STRUCTURAL ANALYSIS OF RNA AND DNA BY EPR SPECTROSCOPY

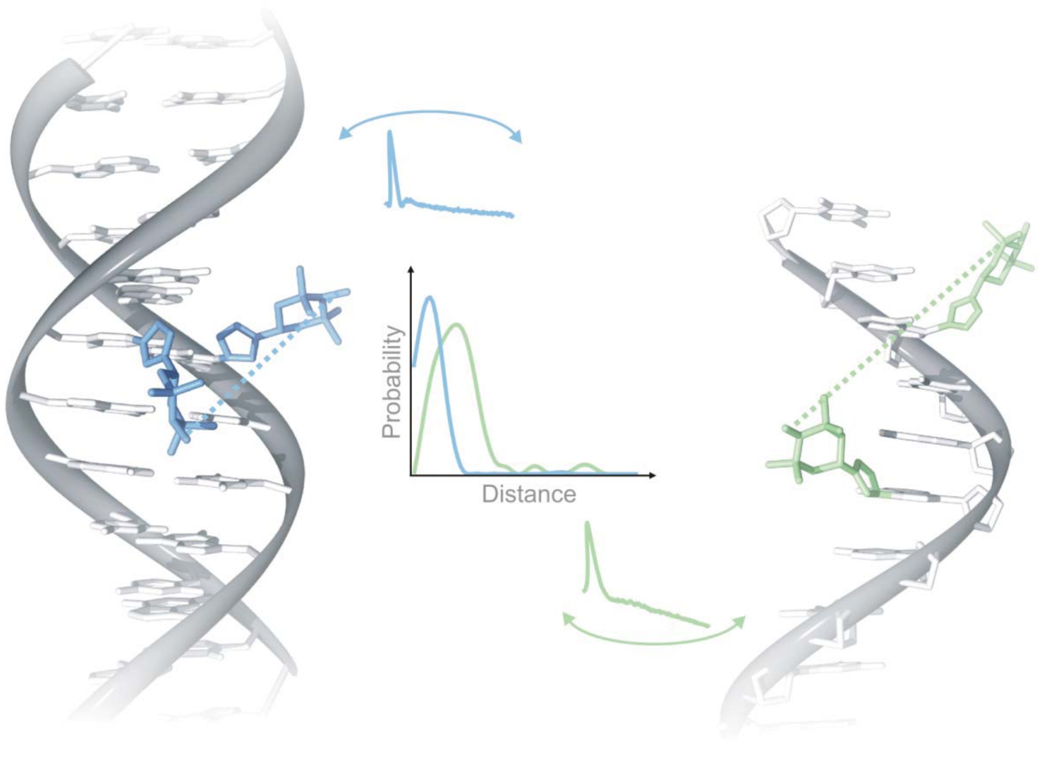

STRUCTURAL ANALYSIS OF RNA AND DNA BY EPR SPECTROSCOPY

DISSERTATION

submitted for the degree of

Dr. rer. nat. (Doctor rerum naturalium)

in the Department of Physics

University of Osnabrueck, Germany

by

Dorith Wunnicke

Osnabrück, 2011

Meinen Eltern.

List of publications

Publications corresponding to this thesis

- Chapter 4
  Wunnicke D, Strohbach D, Weigand JE, Appel B, Feresin E, Suess B, Müller S, Steinhoff HJ (2011) Ligand induced conformational capture of a synthetic tetracycline riboswitch revealed by pulse EPR. *RNA* **17**:172-188.

- Chapter 6
  Ding P, Wunnicke D, Steinhoff HJ, Seela F (2010) Site-directed Spin Labeling of DNA by the Azide-Alkyne 'Click' Reaction: Nanometer Distance Measurements on 7-Deaza-2'-deoxyadenosine and 2'-Deoxyuridine Nitroxide Conjugates Spatially Separated or Linked to a 'dA-dT' Base Pair. *Chemistry - A European Journal* **16**:14385-14396.

Further publications

- Hänelt I*, Wunnicke D*, Müller-Trimbusch M, Vor der Brüggen M, Kraus I, Bakker EP, Steinhoff HJ (2010) Membrane RegionM_{2C2} in Subunit KtrB of the K^+ Uptake System KtrAB from Vibrio alginolyticus Forms a Flexible Gate Controlling K^+ Flux. *Journal of Biological Chemistry* **285**:28210–28219.
  * Both authors contributed equally to this work.

- Hänelt I, Tholema N, Kröning N, Vor der Brüggen M, Wunnicke D, Bakker (2011) KtrB, a member of the superfamily of K(+) transporters. European Journal of Cell Biology doi:10.1016/j.ejcb.2011.04.010

Table of Contents

1 Introduction

1.1 Introduction 2
1.2 References 7

2 Basic principles – Electron Paramagnetic Resonance (EPR) spectroscopy and Molecular Dynamic (MD) simulations

2.1 Introduction …………………………………………………………………… 10
2.2 Electron Paramagnetic Resonance (EPR) spectroscopy ……………….. 10
  2.2.1 Nitroxide spin label ……………………………………………... 10
  2.2.2 Spin Hamiltonian ………………………………………………... 12
  2.2.3 Continuous wave (cw) EPR spectroscopy ……………………. 20
  2.2.4 Pulse EPR spectroscopy ………………………………………… 28
2.3 Molecular dynamics (MD) simulation …………………………………... 30
2.4 References ………………………………………………………………... 33

3 The synthetic tetracycline riboswitch: a *cw* EPR spectroscopy study

3.1 Introduction …………………………………………………………………… 36
3.2 Results and Discussion ……………………………………………………. 38
3.3 Conclusion and Outlook …………………………………………………... 43
3.4 Materials and Methods …………………………………………………… 44
3.5 References ………………………………………………………………... 45

4 Ligand induced conformational capture of a synthetic tetracycline riboswitch revealed by pulse EPR

4.1 Abstract ……………………………………………………………………….. 50
4.2 Introduction …………………………………………………………………… 50
4.3 Results ……………………………………………………………………….. 52
4.4 Discussion ………………………………………………………………... 57
4.5 Materials and Methods …………………………………………………… 59
4.6 References ………………………………………………………………... 62

5 Molecular dynamics (MD) study of a synthetic tetracycline aptamer

5.1 Introduction …………………………………………………………………… 66
5.2 Materials and Methods ……………………………………………………. 66
5.3 Results and Discussion …………………………………………………… 69
5.4 References ………………………………………………………………... 73

6 Site-directed spin labeling of DNA by the azide-alkyne ‘click’ reaction: nanometer distance measurements on 7-deaza-2′-deoxyadenosine and 2′-deoxyuridine nitroxide conjugates spatially separated or linked to a ‘dA-dT’ base pair

6.1 Abstract ……………………………………………………………….... 76
6.2 Introduction ………………………………………………………………. 76
6.3 Results and Discussion ………………………………………………. 78
6.4 Conclusion …………………………………………………………….. 90
6.5 Experimental Section …………………………………………………. 91
6.6 References ……………………………………………………………... 98

7 Site-directed spin labeling by ‘click reaction’ reveals DNA conformational changes induced by mismatch

7.1 Abstract ……………………………………………………………… 102
7.2 Introduction ……………………………………………………….. 102
7.3 Materials and methods ……………………………………………... 104
7.4 Results and Discussion ……………………………………………... 105
7.5 Conclusion ………………………………………………………….. 111
7.6 References …………………………………………………………. 112

8 Summary and Outlook **115**

9 Appendix **119**

1

Introduction

1.1 Introduction

In all life forms genetic information are stored in deoxyribonucleic acids (DNA) and implemented into amino acid sequences of polypeptides by ribonucleic acids (RNA) through gene expression. This makes nucleic acids to one of the most important foundations for living organisms. The two different nucleic acids differ in their sugar structure and nitrogenous bases. DNA contains 2-deoxyribose as sugar and the bases adenine (A), cytosine (C), guanine (G) and thymine (T) while RNA contains ribose and uracil (U) instead of thymine as depicted in Fig. 1.1.

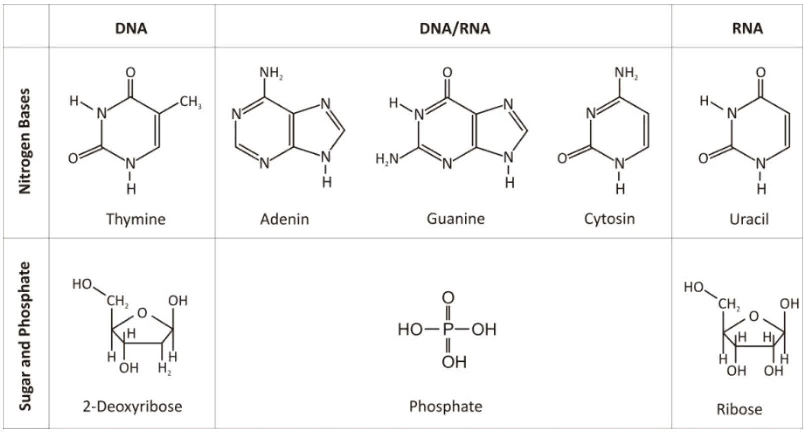

Figure 1.1 Comparison of DNA and RNA nitrogen bases and sugar structures.

The double stranded DNA folds into a double helix comprising two helical strands coiled round the same axis. The backbone of each strand contains the sugar and phosphate residues; whereas the bases point inward and are accessible through the major and minor grooves. Whereas the commonly single stranded RNA is able to adopt complex three-dimensional structures in order to perform a variety of functions.

In particular, gene expression is performed in two subsequent steps in prokaryotes (transcription and translation; cf. Fig. 1.2, A) and three steps in eukaryotes (transcription, pre-mRNA modification and translation). In both cases, the first step includes the transcription of the DNA template strand into the messenger RNA (mRNA) by the so called RNA polymerase. During this process thymine is replaced with uracil. In prokaryotes a single type of RNA polymerase in combination with the Pribnow box and the sigma factor (σ factor) is responsible for transcription. In eukaryotes three RNA polymerases (I-III) are necessary. Each of these polymerases requires specific promoters and transcription factors, DNA binding proteins, to initiate transcription. The mRNA is the carrier of the genetic information from the DNA to the ribosomes. In prokaryotes the mRNA is directly translated in an amino acid sequence, whereas in eukaryotes the pre-mRNA has to be modified before it is transported from the nucleus to the cytoplasm where translation takes place. The constituents of the mRNA in eukaryotes such as the 5' cap, the coding regions, the untranslated regions (UTRs) and the 3' poly(A) tail fulfill a variety of tasks. The 5' cap is a modified guanine nucleotide added to the 5' end of the mRNA. This modification is essential for the recognition and the attachment of the mRNA to the ribosome. The coding regions, providing the genetic information, are composed of nucleotide triplets combined in the so-called codons. These regions begin with the start codon (AUG) and end with a stop codon (UAA, UAG, or UGA). Each of the particular codons encodes for a specific amino acid and is decoded by the ribosome. The amino acid sequence of a protein is predictable alone from the nucleic acid sequence of the DNA. Furthermore, the untranslated regions (UTRs) are located before the start codon (5' UTR) and after the stop codon (3' UTR) and are not translated. These regions are critical for the mRNA stability, mRNA localization, and translational efficiency due to a varying affinity for RNA degrading enzymes called ribonucleases. The 3' poly(A) tail is a long sequence of adenine nucleotides and is added to the 3' end of the mRNA. This tail is used for the export from the nucleus into the cytoplasm and protects the mRNA from degradation. During translation, the second step in prokaryotes and third step in eukaryotes, respectively, the mRNA is decoded by the ribosome to produce a specific amino acid sequence. This process requires two additional types of RNA, the transfer RNA (tRNA) and the ribosomal RNA (rRNA). The transfer RNA (tRNA) mediates the recognition of the codons and exhibits the corresponding amino acid. The rRNA is the RNA constituent of the ribosome and interacts with the tRNAs during translation by providing peptidyl transferase activity. The ribosome itself is divided into the small and large subunits. The small subunit binds to the mRNA and the large subunit to the tRNA. Concluding, the released amino acid sequence folds in its functional three-dimensional structure from random coil.

Mutations in the DNA structure, for instance double-strand breaks, mispairings and nucleobase changes are related to inheritable diseases, cancer and aging[1-3] and have severe effects on the cellular machinery. *In vivo*, misincorporation of nucleotides during replication[4], mutagenic compounds[5, 6] or ionizing radiation[7] are usually responsible for DNA mismatches. The insertion or deletion of a number of nucleotides which are not divisible by three from a DNA sequence results in a change in the reading frame of the codons during translation and ultimately in a frameshift mutation. The translation of the mutated DNA sequence leads to an altered amino acid sequence and therefore in a protein with an impaired functionality. At the same time the incorporation of these mismatches can consequence conformational changes of the DNA structure itself resulting in a hindered transcription process (cf Fig. 1.2, B). The structure-function relationships can be studied in-depth by tracing the mismatch-induced conformational changes.

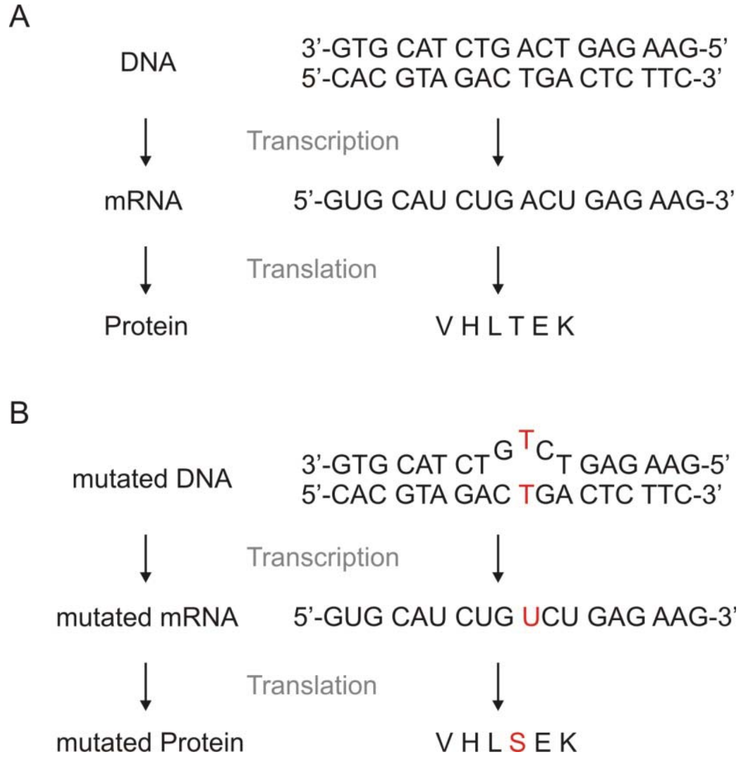

Figure 1.2 Overview of the gene expression of DNA (A) and mutated DNA (B). The genetic information is transcribed into the mRNA and translated in an amino acid sequence. The mutation of the DNA (marked red) caused by the misincorporation of a nucleotide results in an altered amino acid sequence.

As demonstrated in the 1980s RNA can catalyze chemical reactions such as the RNA-catalyzed replication of RNA[8]. The discovery of ribozymes culminates in the hypothesis of the "RNA world"[9]. This hypothesis proposes that in the early state of life RNA overtook most of the biochemical functions of both, DNA and proteins in the cell such as storing of the genetic information and acting as an enzyme. In 2002 Breaker and coworkers discovered natural occurring riboswitches, a new class of RNA molecules which control the implementation of genetic information through the regulation of gene expression[10]. Aptamers, *in vitro* selected riboswitches, bind to various but specific molecular targets such as cofactors, amino acids, drugs or antibiotics[11,12]. They are potential agents for biotechnological and therapeutic applications[13,14] with molecular recognition properties comparable to commonly used antibodies. The aptamer-ligand-complex, inserted into the non-coding region of the mRNA regulates gene expression by means of inhibiting ribosome binding or the movement along the non-coding region (Fig. 1.3). For a more detailed understanding of the functional mechanism of these molecular switches detailed information about the structure and the dynamics of natural and synthetic riboswitches are essential.

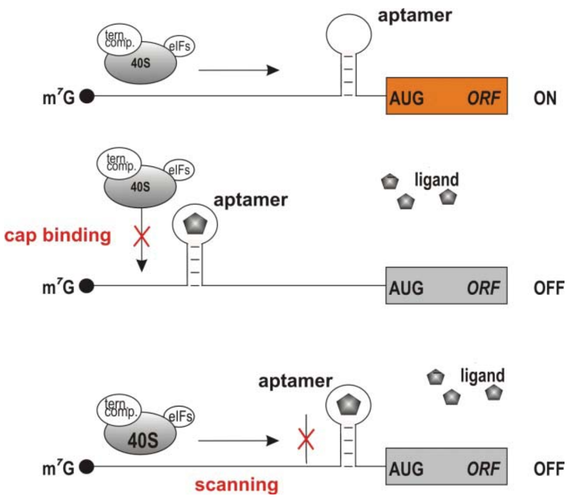

Figure 1.3 Aptamer-ligand mediated translational regulation. Regulation is not affected by the insertion of the aptamer into the non-coding region of the mRNA (top). After ligand addition the aptamer-ligand-complex becomes an obstacle for the ribosome binding (centre) or the movement along the non-coding region (below).

Several methods for structure determination such as NMR (Nuclear Magnetic Resonance) spectroscopy, FRET (Förster resonance energy transfer), and X-ray crystallography have been commonly used in the past. However, all of these approaches exhibit methods-dependent limitations in the application to biomolecules, particularly to nucleic acids. NMR spectroscopy permits to investigate biomacromolecules under conditions close to the physiological state in aqueous solution while it is restricted with respect to the size of the biomacromolecules. The vast majority of natural occurring and synthetic riboswitches are below the limiting molecular weight of about 30 *kDa*. Though, the required concentration of around 1 *mM* represents a major challenge particularly with regard to solid-phase synthesis of oligonucleotides. The second method in aqueous solution, FRET, is based on the energy transfer between two chromophores by means of non-radiative, dipole-dipole coupling in the distance range of 1-10 *nm*. However, the precision of this method is impaired by the uncertainty of the orientation factor and by the size of the chromophores. The orientation factor takes the relative orientation of the chromophores into account and ranges from 0 to 4 for perpendicular and parallel aligned dipoles, respectively. The approximation of the orientation factor results in an uncertain distance determination. Due to the dimensions of the chromophores small structural rearrangements in the investigated biomolecules may remain undiscovered. Furthermore, X-ray crystallography allows the determination of the three-dimensional electron density distribution in crystals with sub-atomic resolutions for rigid structure domains. For dynamic regions the electron densities are not constant in time and hence, structural information about these regions exhibits minor resolution. While there is no limit in the size of the biomacromolecules, artifacts may occur from intermolecular crystal contacts altering the investigated structure. Consequently, all of the above mentioned methods provide individually insufficient information about the structure and the dynamics of biomolecules. In the last years, site-directed spin labeling (SDSL) in combination with electron paramagnetic resonance (EPR) spectroscopy has evolved as a valuable tool to elucidate the structure and dynamics of biological systems such as proteins, protein complexes and nucleic acids under conditions close to the physiological state[15-17]. For this method, a spin labeling technique is essential where the spin label is introduced with high efficiency without affecting the investigated structure. Continuous wave (*cw*) and pulse EPR spectroscopy reveal information about the mobility of the spin label side chains[18], the polarity of their micro-environment[19] and about interspin distances between two spin label side chains in the distance range of 1-8 *nm*[20,21].

The aim of this thesis is to study conformational changes on both, RNA and DNA in more detail applying EPR spectroscopy. This work is divided into three major sections associated with the investigated system:

- *Structural analysis of the synthetic tetracycline (Tc) riboswitch*
  In the first part of this thesis *cw* and pulse EPR experiments in combination with site-directed spin labeling are carried out on a synthetic tetracycline riboswitch to investigate the dynamics and conformational changes of the Tc aptamer upon ligand binding (chapter 3 and 4). Experimental information are utilized as instructions for molecular modeling of the riboswitch in the absence and presence of Tc. In addition, MD simulations of all aptamer models are applied to compare experimentally interspin

distances with simulated ones (chapter 5) and to acquire evidence for the validity of the aptamer models.
RNA sample preparation is accomplished in collaboration with the working groups of Prof. B. Suess (University of Frankfurt) and Prof. S. Müller (University of Greifswald).

- *The copper(I)-catalyzed Huisgen-Sharpless-Meldal alkyne-azide cycloaddition (CuAAC) reaction*
  The copper(I)-catalyzed Huisgen-Sharpless-Meldal alkyne-azide cycloaddition (CuAAC) 'click reaction' is introduced as an alternative spin label strategy in the second part of this work (chapter 6). C*w* and pulse EPR spectroscopy are performed on spin labeled DNA to rate the efficiency of the spin labeling protocol and to examine interspin distance distributions. For that reason, two spin labels are incorporated in the DNA duplex at spatially separated positions or in a 'dA-dT' base pair, respectively. Completive, MD simulations are performed on molecular models of the spin labeled DNA systems to monitor sterical perturbation of the structures and to compare experimentally interspin distances with simulated ones.
  Within the DNA projects samples are prepared in the working group of Prof. F. Seela (University of Osnabrück).

- *Structural analysis of mismatch-induced DNA conformational changes*
  In the last section of this thesis spin labeled DNA with incorporated mismatches such as dT·dT or dA·dA mispairs in between the two spin labels are investigated (chapter 7). For this purpose *cw* and orientation selective pulse EPR measurements in combination with the 'click' reaction are carried out for the matched and mismatched DNA. Dynamics and conformational changes upon incorporation of these mispairs are studied related to the type and nearest neighbor environment of the mismatch.

1.2 References

[1] Q. M. Kong, C. L. G. Lin. *Cellular and Molecular Life Sciences* **2010**, *67*(11), 1817-1829.

[2] A. I. Cederbaum, Y. K. Lu, D. F. Wu. *Archives of Toxicology* **2009**, *83*(6), 519-548.

[3] J. Cadet, T. Douki, D. Gasparutto, J. L. Ravanat. *Mutation Research-Fundamental and Molecular Mechanisms of Mutagenesis* **2003**, *531*(1-2), 5-23.

[4] E. C. Friedberg. *Nature* **2003**, *421*(6921), 436-440.

[5] J. Cadet, S. Bellon, Z. Douki, S. Frelon, D. Gasparutto, E. Muller, J. P. Pouget, J. L. Ravanat, A. Romieu, S. Sauvaigo. *Journal of Environmental Pathology Toxicology and Oncology* **2004**, *23*(1), 33-43.

[6] O. D. Schärer. *Angewandte Chemie International Edition* **2003**, *42*(26), 2946-2974.

[7] S. Bjelland, E. Seeberg. *Mutation Research/Fundamental and Molecular Mechanisms of Mutagenesis* **2003**, *531*(1-2), 37-80.

[8] T. R. Cech. *Proceedings of the National Academy of Sciences of the United States of America* **1986**, *83*(12), 4360-4363.

[9] W. Gilbert. *Nature* **1986**, *319*(6055), 618.

[10] A. Roth, R. R. Breaker. *Annu. Rev. Biochem.* **2009**, *78*, 305-334.

[11] M. Famulok. *Curr. Opin. Struc. Biol.* **1999**, *9*(3), 324-329.

[12] D. J. Patel, A. K. Suri. *J Biotechnol* **2000**, *74*(1).

[13] J. E. Weigand, B. Suess. *Applied Microbiology and Biotechnology* **2009**, *85*(2), 229-236.

[14] M. Famulok, J. S. Hartig, G. Mayer. *Chem. Rev.* **2007**, *107*, 3715-3743.

[15] W. L. Hubbell, D. S. Cafiso, C. Altenbach. *Nat. Struct. Biol.* **2000**, *7*(9), 735-739.

[16] Q. Cai, A. K. Kusnetzow, W. L. Hubbell, I. S. Haworth, G. P. Gacho, N. Van Eps, K. Hideg, E. J. Chambers, P. Z. Qin. *Nucl. Acids. Res.* **2006**, *34*(17), 4722-4730.

[17] E. Bordignon, H.-J. Steinhoff. Membrane protein structure and dynamics studied by site-directed spin labeling ESR, In: (Eds.: M. A. Hemminga and L. J. Berliner), *Biological Magnetic Resonance 27 - ESR Spectroscopy in Membrane Biophysics,* New York, Springer Science and Business Media, **2007**, pp. 129-164.

[18] L. J. Berliner, J. Reuben. *Biological Magnetic Resonance - Vol. 8: Spin Labeling Theory and Applications,* (Eds.: L. J. Berliner and J. Reuben), New York, Plenum Press, **1989**.

[19] H.-J. Steinhoff, A. Savitsky, C. Wegener, M. Pfeiffer, M. Plato, K. Möbius. *Biochim. Biophys. Acta* **2000**, *1457*, 253-262.

[20] C. Altenbach, K. J. Oh, R. J. Trabanino, K. Hideg, W. L. Hubbell. *Biochemistry* **2001**, *40*(51), 15471-15482.

[21] O. Schiemann, T. F. Prisner. *Quarterly Reviews of Biophysics* **2007**, *40*, 1-53.

2

Basic principles - Electron Paramagnetic Resonance (EPR) Spectroscopy and Molecular Dynamics (MD) Simulations

2.1 Introduction

In this chapter the basic principles of electron paramagnetic resonance (EPR) spectroscopy and molecular dynamics (MD) simulation are introduced. EPR spectroscopy exploits the interaction of the magnetic moment of an unpaired electron with an external magnetic field and its environment in a biological system under investigation. The study of the resonant absorption of microwave radiation provides information about the spin label side chain dynamics, the polarity of its environment and inter- and intramolecular distances between spins. In particular, the first paragraphs focus on the fundamental spin Hamiltonian and on two applications namely *cw* and pulse EPR.

Complementary, MD simulation provides insight in the dynamic of the system under investigation based on three-dimensional structural information obtained by molecular modeling or experimental techniques. For this purpose, Newton's classical equation of motion is solved taking preliminarily derived force fields into account as described in the last paragraph. Furthermore, MD simulations enhance the interpretation of experimental data with regard to the perturbation of the system due to the incorporation of the spin label.

2.2 Electron Paramagnetic Resonance (EPR) spectroscopy

2.2.1 Nitroxide spin label

Most biological systems such as proteins, membrane proteins, lipids or nucleotides do not feature an unpaired electron naturally; therefore unpaired electron spins have to be introduced. For this purpose several stable paramagnetic species can be selected, e.g. nitroxide spin labels which are chemically stable and geometrically fairly rigid. In the present work, the (1-oxyl-2,2,5,5-tetramethylpyrroline-3-methyl) methanethiosulfonate (MTS) spin label and the 4-azido-2,2,6,6-tetramethyl-piperidine-1-oxyl (TEMPO) spin label are used. For post-synthetically spin labeling of RNA modified nucleotide 4-thiouridine is incorporated at pre-selected positions and subsequently labeled with the MTS spin label (Fig. 2.1, A). Another approach for spin labeling of RNA is the incorporation of 2'-aminouridine and adjacent selective reaction with the TEMPO spin label (Fig. 2.1, B). 7-deaza-7-ethynyl-2'-deoxyadenosine is chosen for incorporation of terminal triple bonds into DNA and subsequently labeled with the TEMPO spin label (Fig. 2.1, C). Even though the MTS spin label exhibits a 5-membered pyrroline ring in contrast to a 6-membered piperidyl ring of the TEMPO spin label, for both spin label the unpaired electron is located between the N- and O-atoms resulting from the partially overlap of their

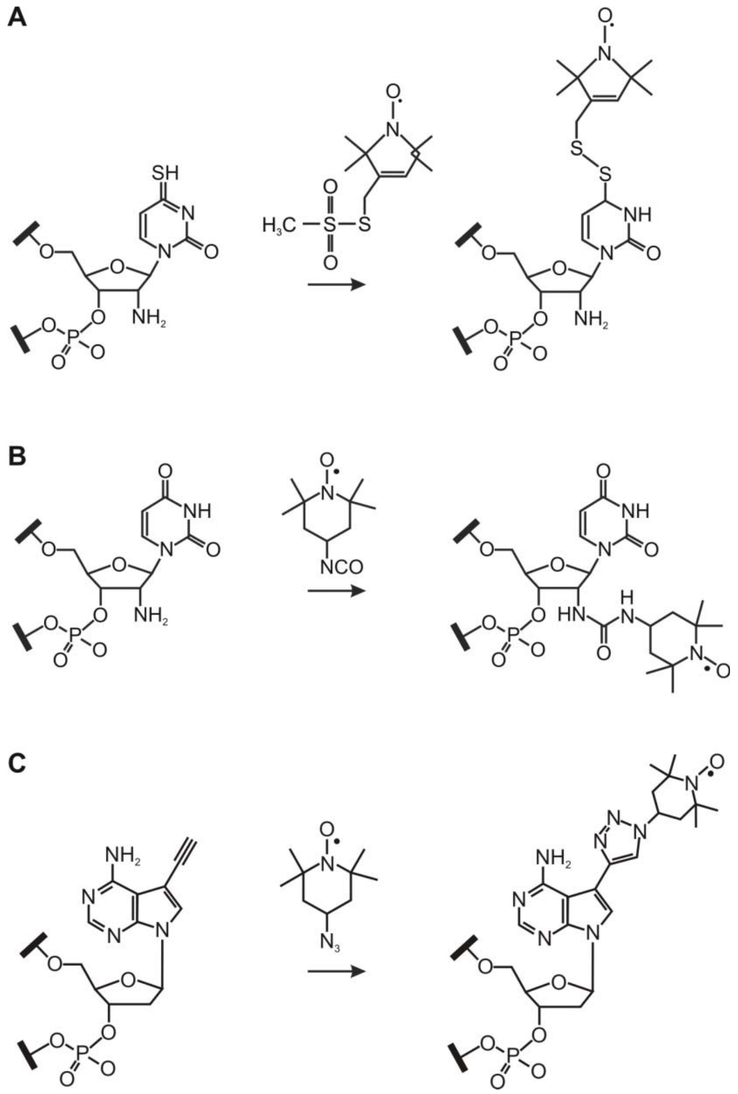

Figure 2.1 Strategy for the post-synthetically introduction of the MTS spin label using the selective reaction with 4-thiouridine (A), of the 4-isocyanato-TEMPO using the selective reaction with 2'-aminouridine (B) and of the 4-azido TEMPO applying copper assisted azide-alkyne ‘click’ reaction with 7-deazadenine (C).

$2p_z$-orbitals. Methyl groups stabilize the spin labels by sterical shielding of the unpaired electrons from their environment. The architecture of the spin label enables several rotations around chemical bonds defining the intrinsic dynamics of the spin label (cf. Fig. 2.1, right site). Based on this, the MTS spin label exhibit higher intrinsic dynamics compared to the TEMPO spin label due to the longer linker.

2.2.2 Spin Hamiltonian

Free electron

Electrons exhibit besides their charge e and mass m_e an intrinsic angular momentum, the so-called electron spin. Associated with the electron spin $\boldsymbol{S}$ is the magnetic moment $\boldsymbol{\mu_s}$

$$\begin{aligned}\boldsymbol{\mu_s} &= -g_e \frac{e\hbar}{2m_e}\boldsymbol{S} \\ &= -g_e \mu_B \boldsymbol{S}\end{aligned} \qquad 2.1$$

where g_e is the g-factor of the free electron, $\hbar$ the Planck constant $h/2\pi$ and μ_B the Bohr magneton. Utilizing the correspondence principle, the energy eigenvalues and eigenvectors of a free electron with spin $\boldsymbol{S} = \frac{1}{2}$ in a homogenous magnetic field $\boldsymbol{B} = (0,0,B_0)$ are the results of solving the eigenvalue equation of the Hamiltonian

$$\mathcal{H}\left|\psi_{\alpha/\beta}\right\rangle = E_{\alpha/\beta}\left|\psi_{\alpha/\beta}\right\rangle. \qquad 2.2$$

The eigenvalues $E_{\alpha/\beta}$ correspond to the α (spin up,↑) and β (spin down,↓) energy states and $\left|\psi_{\alpha/\beta}\right\rangle$ to the eigenvector and electron wave function, respectively. The energy difference ΔE between the energy states

$$\begin{aligned}E_{\alpha,\uparrow} &= +\frac{1}{2} g_e \mu_B \boldsymbol{B} \\ E_{\beta,\downarrow} &= -\frac{1}{2} g_e \mu_B \boldsymbol{B}\end{aligned} \qquad 2.3$$

is

$$\begin{aligned}\Delta E &= E_{\alpha,\uparrow} - E_{\beta,\downarrow} \\ &= g_e \mu_B B_0 \\ &= h\omega_L\end{aligned} \qquad 2.4$$

The energy states are populated according to the Boltzmann distribution. Consequently, in thermal equilibrium the spin down state features a higher population compared to the spin up state. To initiate transitions between both energy levels the fundamental EPR resonance condition (equation 2.4) has to be fulfilled. For this purpose, either the strength of the magnetic field $\boldsymbol{B}$ or the frequency are varied, resulting in one EPR resonance line at

$$B_0 = \frac{\Delta E}{g_e \mu_B}. \qquad 2.5$$

The frequency which fulfills equation 2.4 is the so-called Larmor frequency ω_L . In EPR studies applied here the magnetic field $\boldsymbol{B}$ is in the range of 0.1 to 1 *T*, whereas the frequency ω_L is in the microwave range (≈ 9.4 *GHz*) applied by electromagnetic radiation.

In case of nitroxide spin labels carrying the unpaired electron further interactions between the electron spin and its environment within the molecule have to be taken into account. The energy eigenvalues and eigenvectors of the unpaired electron are defined by the eigenvalue equation of the following spin Hamiltonian

$$\mathcal{H} = \mathcal{H}_{EZ} + \mathcal{H}_{HF} + \mathcal{H}_{Exch} + \mathcal{H}_{DD} + \mathcal{H}_{NZ} \qquad 2.6$$

including the interactions between the electron spin and the magnetic field (electron Zeeman interaction $\mathcal{H}_{EZ}$), nuclear spins (hyperfine interaction $\mathcal{H}_{HF}$) and additional electron spins (Heisenberg exchange coupling and dipole-dipole coupling $\mathcal{H}_{Exch}, \mathcal{H}_{DD}$), furthermore the interaction of nuclear spins with the external magnetic field (nuclear Zeeman interaction $\mathcal{H}_{NZ}$). The next sections provide an overview of the respective contributions to the spin Hamiltonian. Detailed theoretical introductions can be found in the literature[1-5].

Electron Zeeman interaction and g-anisotropy

In addition to the above mentioned interaction between the electron spin $\boldsymbol{S}$ and the external magnetic field, the interaction between the orbital momentum $\boldsymbol{L}$ and **B** has is taken into account. In this case, the magnetic moment of

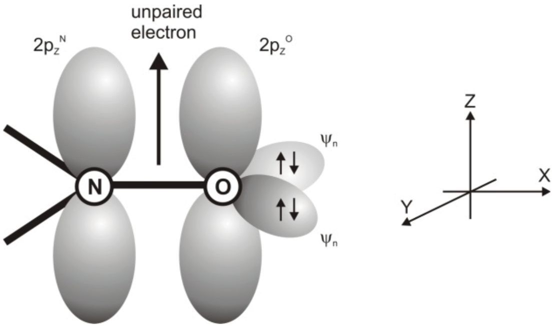

Figure 2.2 Schematic representation of the spin label N-O bond. The oxygen 2s, $2p_x$ and $2p_y$-orbitals superimpose to the non-bonding lone pair orbitals $\psi_{nx,y}$. The spin label frame is represented on the right side. (Figure based on [6])

the electron depends on its orientation with respect to the molecule or on the orientation of the molecule with respect to the magnetic field direction, respectively. Due to this anisotropy the g-factor has to be extended to a g-tensor

$$\boldsymbol{g} = \begin{pmatrix} g_{xx} & g_{yx} & g_{zx} \\ g_{xy} & g_{yy} & g_{zy} \\ g_{xz} & g_{yz} & g_{zz} \end{pmatrix} \qquad 2.7$$

and the electron Zeeman term of the spin Hamiltonian to

$$\mathcal{H}_{EZ} = \mu_B \boldsymbol{BgS}. \qquad 2.8$$

Due to the fact that the eigensystem of the g-tensor is fixed within the spin label molecule, it is convenient to define a spin label coordinate system, which coincides with the eigenframe of the g-tensor and all magnetic tensors discussed later.

In this frame, the z-axis is oriented parallel to the $2p_z$-orbital, the x-axis is aligned along the N-O bond and the y-axis perpendicular to both axes as illustrated in Fig. 2.2. Thus, the g-tensor can be written as a diagonal tensor

$$\boldsymbol{g} = \begin{pmatrix} g_{xx} & 0 & 0 \\ 0 & g_{yy} & 0 \\ 0 & 0 & g_{zz} \end{pmatrix} \qquad 2.9$$

with the elements

$$\begin{aligned} g_{xx} &\approx g_e + 2\lambda(O)\frac{\rho_\pi^O c_{nx}^2}{E_\pi - E_n} \\ g_{yy} &\approx g_e + 2\lambda(O)\frac{\rho_\pi^O c_{ny}^2}{E_\pi - E_n} \\ g_{zz} &\approx g_e \end{aligned} \qquad 2.10$$

including the spin-orbit coupling constant $\lambda(O) = 151\ cm^{-1}$[6]. The π spin density of the oxygen $2p_z$ atomic orbital is ρ_π^O and $\Delta E_{n\rightarrow\pi}$ is the excitation energy for a transition between an orbital of the non-bonding oxygen electron pairs and the N-O bond π-orbital. Furthermore, the molecular orbital coefficients $c_{nx,y}$ of the $2p_x$ and $2p_y$-orbitals contribute to the oxygen lone pair orbital $\psi_{nx,y}$, respectively. Typical values for the g-tensor elements are

$$\begin{aligned} g_{xx} &\approx 2.0089 \\ g_{yy} &\approx 2.0067 \\ g_{zz} &\approx 2.0023. \end{aligned} \qquad 2.11$$

In EPR experiments with a magnetic field strength of 0.3 T the g-tensor anisotropy is not resolved. For this purpose the magnetic field strength has to be in the range of 3 T or higher. For an unbound nitroxide spin label molecule in aqueous solutions the g-anisotropy is averaged out due to the fast molecular motions, and the g-tensor can be simplified to an isotropic value

$$g_{iso} \approx g_{xx} \approx g_{yy} \approx g_{zz} = \tfrac{1}{3}(g_{xx} + g_{yy} + g_{zz}) \qquad 2.12$$

and consequently the electron Zeeman term to

$$\mathcal{H}_{EZ} = \mu_B \boldsymbol{B} g_{iso} \boldsymbol{S}. \qquad 2.13$$

Hyperfine interaction and A-anisotropy

The hyperfine interaction between an electron spin $\boldsymbol{S}$ and a nuclear spin $\boldsymbol{I}$ represents one of the most important sources of information in EPR spectroscopy of nitroxides. It leads to a splitting of the EPR resonance line according to the magnetic quantum number m_I of the nucleus (Fig. 2.3). Both, in MTS and in TEMPO spin label the nitrogen exhibits a nuclear spin of $\boldsymbol{I} = 1$ and a magnetic quantum number of $m_I = \pm 1$ resulting in three EPR resonance lines in the experimental spectra due to the quantum mechanical selection rules $(\Delta m_S = \pm 1, \Delta m_I = 0)$. The hyperfine interaction is described by the Hamiltonian

$$\mathcal{H}_{HF} = -\boldsymbol{SAI} \qquad 2.14$$

where **A** is the hyperfine splitting tensor. The hyperfine splitting tensor can be written as the sum of an isotropic part, the so-called Fermi contact interaction and an anisotropic part, the so-called electron-nuclear dipole-dipole coupling

$$\mathcal{H}_{HF} = \mathcal{H}_{HF,aniso} + \mathcal{H}_{HF,iso}. \qquad 2.15$$

The electron-nuclear dipole-dipole coupling results from the interaction between the nuclear spin $\boldsymbol{I}$ and the electron spin $\boldsymbol{S}$ magnetic moments. Applying the point dipole approximation the anisotropic contribution of the hyperfine interaction is defined by

$$\begin{aligned} \mathcal{H}_{HF,aniso} &= -\boldsymbol{S}\boldsymbol{A}_{aniso}\boldsymbol{I} \\ &= \frac{\mu_0}{4\pi}\mu_B g_e \mu_n g_n \left(\frac{\boldsymbol{SI}}{r_{SI}^3} - \frac{3(\boldsymbol{S}\boldsymbol{r}_{SI})(\boldsymbol{I}\boldsymbol{r}_{SI})}{r_{SI}^5}\right) \end{aligned} \qquad 2.16$$

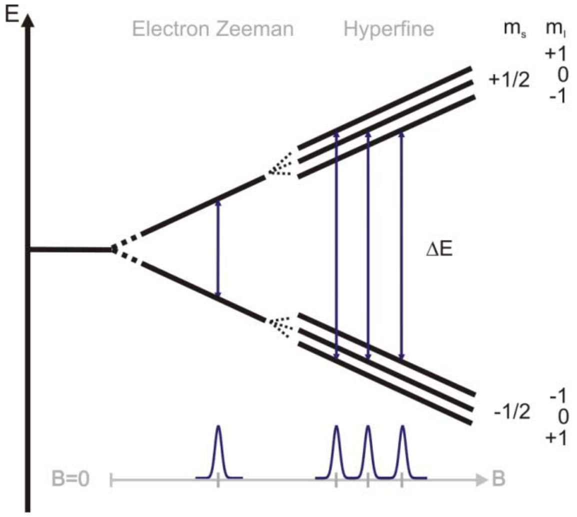

Figure 2.3 Schematic representation of the electron Zeeman and hyperfine interaction. For a system with $\boldsymbol{S} = \frac{1}{2}$ and $\boldsymbol{I} = 1$ the hyperfine interaction results in a splitting of the EPR resonance line into three EPR resonance lines according to the quantum mechanical selection rules ($\Delta m_S = \pm 1, \Delta m_I = 0$).

with the vacuum permeability μ_0, the vector r_{SI} connecting the nuclear spin $\boldsymbol{I}$ and the electron spin $\boldsymbol{S}$, the nuclear magneton μ_n and the nuclear g-factor g_n. In the presence of a strong external magnetic field all contributions perpendicular to the magnetic field direction can be neglected (high field approximation). For a magnetic field aligned along the z-axis the anisotropic hyperfine interaction simplifies to

$$\mathcal{H}_{HF,aniso} = \frac{\mu_0}{4\pi}\mu_B g_e \mu_n g_n \left(\frac{1-3cos^2\theta}{r_{SI}^3}\right)\boldsymbol{S}_z\boldsymbol{I}_z. \qquad 2.17$$

It depends on the angle θ between the vector $\boldsymbol{r_{SI}}$ and the magnetic field direction. Assuming that the z-axis of the spin label eigensystem coincides with the vector $\boldsymbol{r_{SI}}$, θ describes the angle between the spin label z-axis and the magnetic field direction. Thus, in the spin label frame the A-tensor is diagonal and can be written as

$$\boldsymbol{A}_{aniso} = \frac{\mu_0}{4\pi}\frac{g_e\mu_B g_n\mu_n}{{r_{SI}}^3}\begin{pmatrix} -1 & 0 & 0 \\ 0 & -1 & 0 \\ 0 & 0 & 2 \end{pmatrix} \qquad 2.18$$

In contrast, the isotropic contribution to the hyperfine interaction

$$\mathcal{H}_{HF,iso} = \boldsymbol{a}_{iso}\boldsymbol{SI} \qquad 2.19$$

originates from the finite probability of the electron to appear at the nucleus. The isotropic character of this contribution arises from the fact that only electrons in s-orbitals exhibit the non-vanishing probability, resulting in an orientation independent hyperfine splitting

$$\boldsymbol{a}_{iso} = \frac{2\mu_0}{3\hbar} g_e \mu_B g_n \mu_n |\psi_{r=0}|^2 \qquad 2.20$$

where $|\psi_{r=0}|^2$ is the electron spin density at the nucleus. In conclusion, the A-tensor can be summarized as

$$\begin{aligned} \mathbf{A} &= \boldsymbol{A}_{aniso} + \mathbf{1}a_{iso} \\ &= \begin{pmatrix} A_{xx} & 0 & 0 \\ 0 & A_{yy} & 0 \\ 0 & 0 & A_{zz} \end{pmatrix} \end{aligned} \qquad 2.21$$

with following typical values for the respective tensor elements of nitroxides

$$\begin{aligned} A_{xx} &\approx 0.5\ mT \\ A_{yy} &\approx 0.5\ mT \\ A_{zz} &\approx 3.5\ mT. \end{aligned} \qquad 2.22$$

In analogous to the g-tensor, for free spin labels in aqueous solution the ***A***-tensor has the form

$$A_{iso} \approx A_{xx} \approx A_{yy} \approx A_{zz} = \tfrac{1}{3}(A_{xx} + A_{yy} + A_{zz}). \qquad 2.23$$

Electron-electron interaction

The effect of the interaction between two electron spins depends beside others on their interspin distance. In case of interspin distances larger than approximately 1 nm the electron spins are considered to be two magnetic point dipoles μ_1 and μ_2. The energy between two magnetic point dipoles is described by

$$E = -\mu_1 B_2(r_{12}) = -\mu_2 B_1(r_{21}) \qquad 2.24$$

with the magnetic field B_2 of the dipole 2 at the dipole 1. Utilizing the correspondence principle in combination with the equation describing the spatial field distribution of a magnetic dipole, the Hamiltonian for the dipole-dipole interaction is

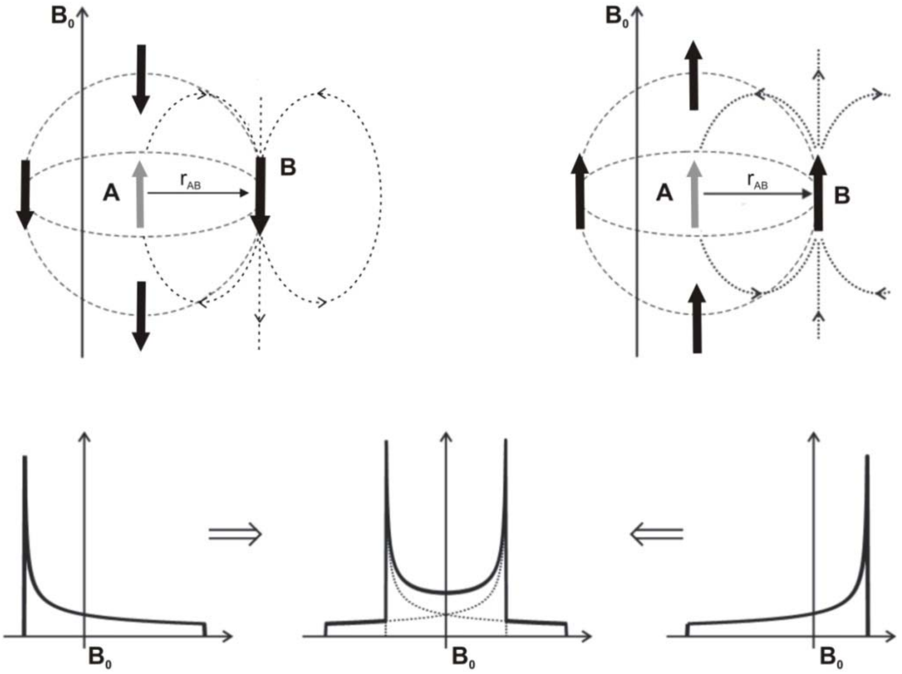

Figure 2.4 Top: Alignment of a dipolar coupled spin pair A (grey arrows) and B (black arrows) in an external magnetic field. Spin B is aligned parallel to spin A. In a powder sample spin B is statistically distributed over the unit sphere (dashed lines) centered on spin A. Bottom: Shifts of the resonance line positions caused by dipolar coupling. The Pake pattern (center) is the superposition of all orientations taking the weighting factor $sin\Theta_{\mathrm{DD}}$ into account where Θ_{DD} represents the angle between the magnetic field direction and the dipolar vector r_{AB}. The highest contribution results from the perpendicular case ($\Theta_{\mathrm{DD}} = 90°$) when spin B is located on the equator. The largest splitting arises from the parallel case ($\Theta_{\mathrm{DD}} = 0°$) when spin B is positioned at the poles. The inversion of the spin B orientation results in the inversion of the transition distribution (Figure adopted from [7]).

$$\mathcal{H}_{DD} = \frac{\mu_0}{4\pi}\left(\frac{\boldsymbol{\mu_1\mu_2}}{r_{12}^3} - \frac{3(\boldsymbol{\mu_1 r_{12}})(\boldsymbol{\mu_2 r_{21}})}{r_{12}^5}\right) \qquad 2.25$$

where r_{12} is the distance between the dipoles. Equation 2.25 can be modified for a spin pair $\mathbf{S_A}$ and $\mathbf{S_B}$, with r_{AB} the distance between the spins and the dipole-dipole coupling tensor **D** to

$$\mathcal{H}_{DD} = \frac{\mu_0}{4\pi\hbar}\frac{g_A\mu_B g_B\mu_B}{{r_{AB}}^3}\left(\boldsymbol{S_A S_B} - \frac{(\boldsymbol{S_A r_{AB}})(\boldsymbol{S_B r_{AB}})}{r_{AB}^2}\right)$$

$$\mathcal{H}_{DD} = \boldsymbol{S_A D S_B}. \qquad 2.26$$

This interaction is field-independent and is therefore called zero-field splitting. Assuming a negligible g-anisotropy ($g_A \approx g_B \approx g_e$) and considering the high-field approximation, the dipole-dipole interaction can be written as

$$\mathcal{H}_{DD} = \omega_{\mathrm{DD}}\hbar \mathrm{S}_{\mathrm{A,z}}\mathrm{S}_{\mathrm{B,z}} \tag*{2.27}$$

with the dipolar frequency

$$\omega_{DD} = \frac{\mu_0 g_e{}^2 \mu_B{}^2}{4\pi\hbar}\left(\frac{1-3cos\Theta_{\mathrm{DD}}}{r_{AB}{}^3}\right) \tag*{2.28}$$

where Θ_{DD} represents the angle between the magnetic field direction and the dipolar vector r_{AB}. In disordered samples the spin label orientations and therefore the dipolar vectors are statistical distributed over the unit sphere with respect to the external magnetic field direction. Hence, equation 2.27 and 2.28 have to be averaged over all angles Θ_{DD} applying the weighting factor $sin\Theta_{\mathrm{DD}}$. This leads to the so-called Pake pattern (Fig. 2.4). Due to the weighting factor $sin\Theta_{\mathrm{DD}}$ the highest contribution to the Pake pattern arises for $\Theta_{\mathrm{DD}} = 90°$ (perpendicular component). In this case spin B is located on the equator of the unit sphere centered on spin A (cf. Fig. 2.4). Whereas the largest splitting of the Pake pattern results from $\Theta_{\mathrm{DD}} = 0°$ (parallel component). In this case spin B is positioned at the poles of the unit sphere. As a result, the dipolar frequency and the shape of the Pake pattern depend on the interspin distance between spin pair A and B.

For electrons spins in close proximity, distances less than approximately 1 *nm*[8], the finite overlap of their orbitals results in an exchange of their spin functions, the so-called Heisenberg exchange coupling. If the spins align anti-parallel, both spins can form an electron pair or a covalent bond resulting in a vanishing EPR signal. In contrast, if the spins align parallel due to Coulomb interaction the Heisenberg exchange interaction is defined as

$$\mathcal{H}_{Exch} = \mathrm{J}\mathbf{S_1}\mathbf{S_2} \tag*{2.29}$$

where J is the isotropic exchange coupling constant

$$\mathrm{J} = -2\left\langle \psi_{\mathrm{a}}(1)\psi_{\mathrm{b}}(2) \middle| \frac{\mathrm{e}^2}{4\pi\epsilon_0 \mathrm{r}} \middle| \psi_{\mathrm{a}}(2)\psi_{\mathrm{b}}(1) \right\rangle \tag*{2.30}$$

which considers the strength of the orbital overlap with $\psi_{\mathrm{a,b}}$ as the different spatial orbital wave functions. The distance-dependence of the exchange coupling allows interspin distance determination in a distance range below 1 *nm*. Furthermore, the study of the exchange coupling constant permit the determination of spin label accessibilities towards rapidly relaxing paramagnetic species which is not part of this work.

Nuclear Zeeman interaction

The coupling of a nuclear spin $\boldsymbol{I}$ with the external magnetic field $\mathbf{B}$ can be defined analogous to the electron Zeeman interaction as

$$\mathcal{H}_{NZ} = \mu_n g_n \mathbf{B}\boldsymbol{I}. \qquad 2.31$$

While the nuclear spin $\boldsymbol{I}$ and the nuclear g-factor are inherent properties of the nucleus, its contribution is not significant and has marginal influence on the EPR spectra.

The total Spin Hamiltonian

The total Spin Hamiltonian is composed of the above presented contributions and has the form

$$\begin{aligned}\mathcal{H} &= \mathcal{H}_{EZ} + \mathcal{H}_{HF} + \mathcal{H}_{NZ} + \mathcal{H}_{Exch} + \mathcal{H}_{DD} \\ &= \sum_{\mathrm{i}} \mu_{\mathrm{B}} \mathbf{g}_{\mathrm{e}} \mathbf{B}\mathbf{S_i} - \sum_{\mathrm{k}} \mu_n \mathbf{g}_{\mathrm{n}} \mathbf{B}\mathbf{I_k} + \sum_{\mathrm{i,k}} \mathbf{S_i}\mathbf{A}\mathbf{I_k} + \mathrm{J}\mathbf{S_1}\mathbf{S_2} + \mathbf{S_1}\mathbf{D}\mathbf{S_2}.\end{aligned} \qquad 2.32$$

In most EPR experiments the electron Zeeman interaction is the dominant interaction. At this, both the nuclear quadrupol interaction and the nuclear spin-spin interaction are neglected. The nuclear quadropul interaction takes effect when the nuclear spin I exhibits a quadrupol moment, i.e. the nuclear spin is $\boldsymbol{I} > 1$, unlike the spin labels presented in this work which possess a nuclear spin of $\boldsymbol{I} = 1$. The nuclear spin-spin interaction is only of influence in high resolution hyperfine spectra using pulse EPR techniques which is not relevant in this work.

2.2.3 Continuous wave (*cw*) EPR spectroscopy

For *cw* EPR studies the samples are positioned in a homogeneous magnetic field B_0. The EPR absorption spectra are detected under a constant and continuous microwave radiation, while the magnetic field B_0 is varied. To enhance the sensitivity an oscillating magnetic field B_{mod} is applied parallel to B_0. Due to the phase sensitive lock-in detection the first derivative is detected. An EPR spectrum provides a wide variety of informations such as spin label side chain dynamics, the polarity of the spin label environment, accessibilities to paramagnetic quencher and distances between spin labels in the 1-2 *nm* range. These spectra are obtained either at room temperature (298 *K*) or at low temperature (160 *K*). This knowledge may aid not only to trace conformational changes but also to enhance the comprehension of structure-function relationship of biomolecules.

The *cw* EPR spectrum

The transitions of the EPR spectrum can be calculated by solving the eigenvalue equation of the spin Hamiltonian. To determine the eigenvalues it is convenient to transform the terms of the spin Hamiltonian from the spin label frame into the laboratory frame. The z^L-axis of the laboratory frame coincides with the external magnetic field direction $\boldsymbol{B}_0 = (0,0,B_0)$. The necessary transformation (cf. Fig. 2.5) is accomplished by the implementation of the rotation matrix **R**

$$\boldsymbol{R} = \begin{pmatrix} cos\vartheta cos\varphi & cos\vartheta sin\varphi & -sin\vartheta \\ -sin\varphi & cos\varphi & 0 \\ sin\vartheta cos\varphi & sin\vartheta sin\varphi & cos\vartheta \end{pmatrix} \qquad 2.33$$

and results in

$$\begin{gathered} \boldsymbol{g}^L = \boldsymbol{RgR}^{-1} \\ \boldsymbol{A}^L = \boldsymbol{RAR}^{-1} \end{gathered} \qquad 2.34$$

The spin Hamiltonian for a spin label possessing an unpaired electron with the spin quantum number $\boldsymbol{S} = \frac{1}{2}$ and hyperfine interaction of the unpaired electron with the nitrogen atom ($\boldsymbol{I} = 1$) is described by

$$\mathcal{H} = \mathcal{H}_{EZ} + \mathcal{H}_{HF} = \mathrm{\mu_B}\mathbf{gBS} + \mathbf{SAI}. \qquad 2.35$$

The eigenvalues of the transformed spin Hamiltonian[9] are

$$E_{m_S,m_I} = m_s \mu_B g(\vartheta,\varphi) B_0 + m_s m_I A(\vartheta,\varphi) \qquad 2.36$$

where

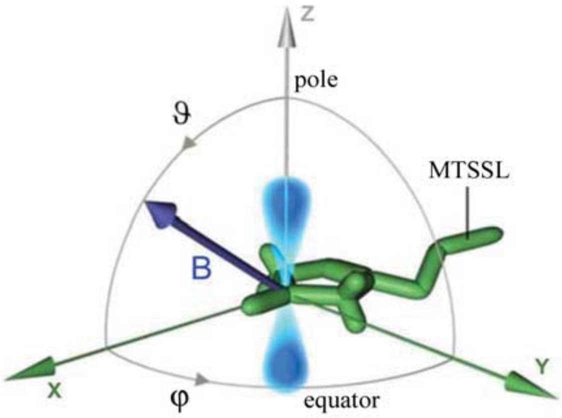

Figure 2.5 Transformation from the spin label frame (x, y, z) to the laboratory frame (z^L-axis corresponding to the B-field direction (dark blue)) by means of a rotation by angle φ about the z-axis and an adjacent rotation by angle ϑ about the new y-axis. (Figure adopted from [10]).

$$\begin{aligned} g(\vartheta,\varphi) = g^L &= g_{xx} sin^2\vartheta cos^2\varphi + g_{yy} sin^2\vartheta sin^2\varphi + g_{zz} cos^2\vartheta \\ A(\vartheta,\varphi) = A^L &= \sqrt{{A_{xx}}^2 sin^2\vartheta cos^2\varphi + {A_{yy}}^2 sin^2\vartheta sin^2\varphi + {A_{zz}}^2 cos^2\vartheta} \end{aligned} \quad 2.37$$

are the g-factor and hyperfine coupling constant. The two depend on the orientation of the magnetic field with respect to the spin label (ϑ,φ). Taking into account the quantum mechanical selection rules $(\Delta m_s = \pm 1, \Delta m_I = 0)$, EPR transition lines arise at the resonance magnetic field positions

$$\begin{aligned} B_0(m_I = +1) &= \frac{\Delta E}{\mu_B g(\vartheta,\varphi)} - A(\vartheta,\varphi) \\ B_0(m_I = 0) &= \frac{\Delta E}{\mu_B g(\vartheta,\varphi)} \\ B_0(m_I = -1) &= \frac{\Delta E}{\mu_B g(\vartheta,\varphi)} + A(\vartheta,\varphi) \end{aligned} \quad 2.38$$

Hence, the EPR spectrum exhibit three absorption lines where the low and the high field peak are separated by $A(\vartheta,\varphi)$ from the center line at $g(\vartheta,\varphi)$, respectively, as depicted in Fig. 2.6.

At this point, EPR transitions would occur until the populations of the energy states are equilibrated. Relaxation processes counteract the saturation of the system and return the system to its equilibrium state. These processes may proceed either with the transfer of energy (longitudinal relaxation T_1) or without (transversal relaxation T_2). The longitudinal or spin-lattice relaxation T_1 includes the energy transfer between electron spins and their environment. This effect causes the relaxation to thermal equilibrium and consequently to the Boltzman distributed population of the energy states. In liquid solutions the energy transfer is provided by means of molecular motion, intermolecular dynamics and collisions, whereas in solids interaction with the lattice vibration is responsible for energy transfer. The transverse or spin-spin relaxation time T_2 is a spin flip-flop process of two spins where the energy is preserved, while the phase relation between these spins is extinguished.

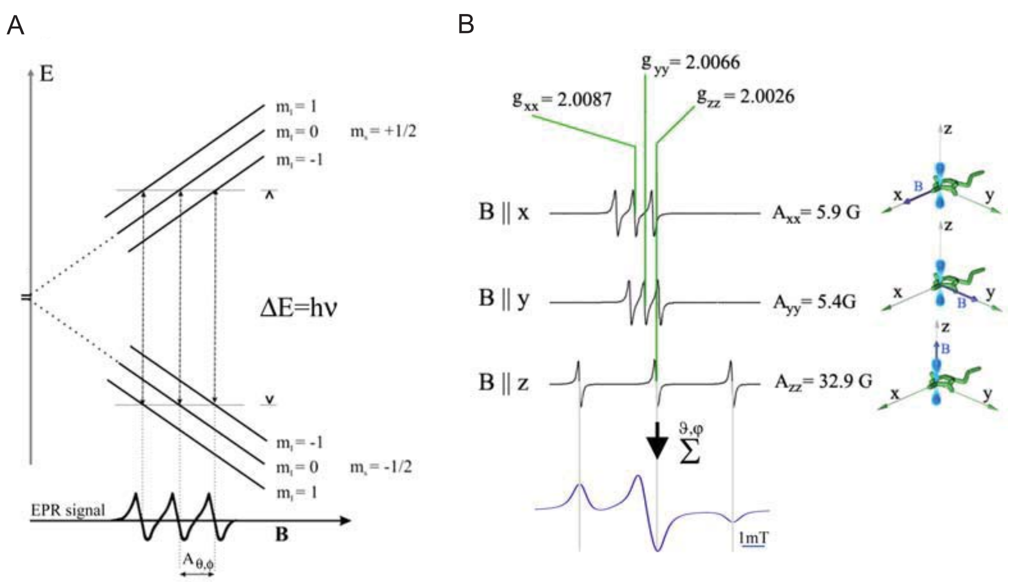

Figure 2.6 A: The hyperfine coupling of an unpaired electron ($\boldsymbol{S} = \frac{1}{2}$) with a nucleus ($\boldsymbol{I} = 1$) results in three EPR transition lines according to the quantum mechanical selection rules. Due to the Lock-in technique, the first derivative of the absorption lines is detected. The low and the high field peak are separated by $A(\vartheta, \varphi)$ from the center line at $g(\vartheta, \varphi)$, respectively. B: EPR spectra corresponding to different orientations of the spin label with respect to the external magnetic field (black spectra). In the extreme cases the spin label x-, y- and z-axis are aligned parallel to the magnetic field direction, respectively. All homogeneous distributed orientations in between the extreme cases superimpose to the powder spectrum (blue spectrum). (Figure adopted from [7] and [10])

Spin label side chain dynamics

Studies of the spin label side chain dynamics in liquid solutions are performed at room temperature. Here, the effective g- and A-tensors and thus the spin Hamiltonian become time-dependent. As a consequence of molecular motion on the nanosecond time scale, the anisotropic components of the tensors in the spin

Hamiltonian particular average out. The dynamics of the spin label and the extent of averaging of the spectral anisotropy are characterized by the rotational correlation time τ_c. For $t < \tau_c$ the stochastical orientations of the spin label are correlated, while the correlation is extinguished after several τ_c. Furthermore, the inverse rotational correlation time ${\tau_c}^{-1}$ is proportional to the transverse relaxation time ${\tau_c}^{-1} \propto T_2$[3].
Depending on the spectral anisotropy $\Delta\omega$, τ_c is assigned to four different dynamic regimes (cf. Fig. 2.7): the isotropic limit ($\Delta\omega \ll {\tau_c}^{-1}$), the fast motion regime ($\Delta\omega < {\tau_c}^{-1}$), the slow motion regime ($\Delta\omega > {\tau_c}^{-1}$) and the rigid limit ($\Delta\omega \gg {\tau_c}^{-1}$)[1]. The spectral anisotropy $\Delta\omega$ is the maximal possible resonance frequency shift caused by the anisotropy of the tensors.

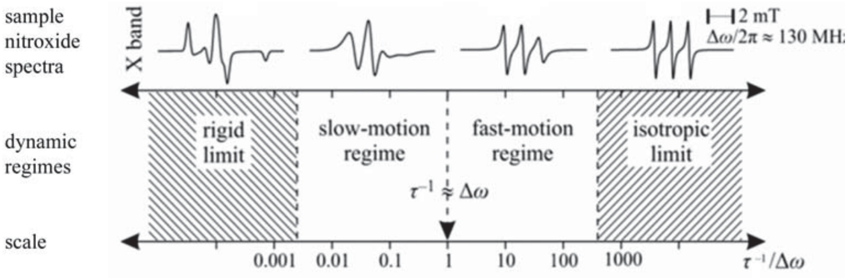

Figure 2.7 Overview of the dynamic regimes in cw EPR spectra at X-band classified by the rotational correlation time ${\tau_c}^{-1}$ with representative spectra shown above. (Figure modified from [1])

In the fastest regime, the isotropic limit, the anisotropies are completely averaged out. The EPR spectrum exhibits three lines with narrow line widths and small hyperfine splitting. In order to gain a simulated EPR spectrum initially the resonance line positions are calculated utilizing isotropic g- and A-values. The superposition of the resonance positions add up to the so-called stick spectrum. This stick spectrum is then convoluted with a Lorentzian line function with a FWHM (full width at half maximum) proportional to $\frac{1}{T_2}$ with the calculated stick spectrum.
The Redfield theory, based on perturbation theory, is the basic principle for spectra simulation in the fast motion regime[11]. In this regime slight spectral anisotropies arise, though the isotropic g- and A-values are sufficient to describe the spectral line positions and the consecutive stick spectrum. Convolution of the stick spectrum with the above mentioned Lorentzian line exhibiting a FWHM$\propto T_2$ is inadequate for calculation of the line widths and the intensities of the respective spectral line. Taking the broadening of the spectral lines into account, the transverse relaxation time has the form

$$\frac{1}{T_2} = A_0 + A + Bm_I + Cm_I^2 \tag{2.39}$$

where A_0 represents the natural line width and A, B, C the broadening due to spectral anisotropies. The line broadening is affected by the nuclear magnetic quantum number m_I and differs among the spectral line positions. At the same time the integral of the absorption lines is proportional to the number of spins. Thus, the broadening of a spectral line results in decreased spectral line intensity. In the EPR spectrum the broader high field peak exhibit a lower intensity compared to the low field peak.

If ${\tau_c}^{-1}$ becomes smaller than the spectral anisotropy, the superposition of Lorentzian lines are insufficient to simulate the EPR spectrum. For the slow motion regime it is necessary to determine the expected value $\bar{\rho}$ of the time-dependent density matrix which describes statistically the energy state populations and their coherence [12]. The stochastic Liouville equation

$$\frac{\partial}{\partial t}\bar{\rho}(\Omega,t) = -i\left[\hat{\mathcal{H}}(\Omega(\mathrm{t})), \rho(\Omega,t)\right] - \Gamma_\Omega[\rho(\Omega,t) - \rho_0(\Omega)] \qquad 2.40$$

yields the time evolution of $\bar{\rho}$. Ω describes the three Euler angles specifying the transformation between spin label and laboratory frame, $\hat{\mathcal{H}}$ the time-dependent spin Hamiltonian, ρ_0 the equilibrium population of the density matrix and Γ_Ω (Markov operator) the rotational diffusion such as Brownian or jump diffusion. To solve the equation 2.40 it is convenient to divide $\hat{\mathcal{H}}$ into three parts

$$\hat{\mathcal{H}}(\Omega(\mathrm{t})) = \hat{\mathcal{H}}_0 + \hat{\mathcal{H}}_1(\Omega(\mathrm{t})) + \varepsilon(t) \qquad 2.41$$

and to introduce Wigner rotation functions as eigenfunctions of the spin Hamiltonian. The first term represents the isotropic contributions including the electron Zeeman, the nuclear Zeeman and the hyperfine interaction under the assumption of the high-field approximation. The anisotropic contributions are summarized in the second term which depends on the three Euler angles. The last term describes the effect of the applied microwave field B_1. Simulation of the EPR spectra in this dynamic range can be performed by the program SRLS (slowly relaxing local structure)[13].

In the rigid limit the biomolecules and the attached spin labels are completely immobilized. The orientations of the spin labels are homogeneously distributed over the unit sphere. The resonance line positions are calculated for all orientations utilizing the orientation dependent g- and A-tensors according to equations 2.37. To sufficiently simulate the respective line widths the stick spectrum is convoluted with a pseudo-Voigt function. EPR spectra of powder samples or of frozen solutions are constituents of the rigid limit as presented in the following paragraph.

Furthermore, the term mobility was introduced in addition to the rotational correlation time τ_c[14]. It accounts for all effects which influence τ_c such as the spin label architecture, secondary and tertiary structure interaction and the dynamics of the backbone. In this regard weak interactions of the spin label with the biomolecules as in loop regions correspond to fast rotational correlation times and to the perception of high spin label side chain mobility. Whereas a restricted motional freedom of the spin label results in a strong interaction of spin label with the molecule, long correlation times and low spin label side chain mobility.

Polarity and distance measurements

In frozen solutions at low temperature (T = 160 *K*) *cw* EPR experiments the biomolecules and attached spin labels under investigation are completely immobilized. The spin label orientations are homogeneously distributed with respect to the external magnetic field direction. The spectra corresponding to each particular orientation superimpose to the EPR powder spectrum (see Fig. 2.6, B), while the g- and A-values are calculated according to equations 2.37. The spectral line shape of these spectra is influenced by both, the hyperfine coupling and the dipolar interaction between spins in close proximity (r < 2 *nm*)[15].

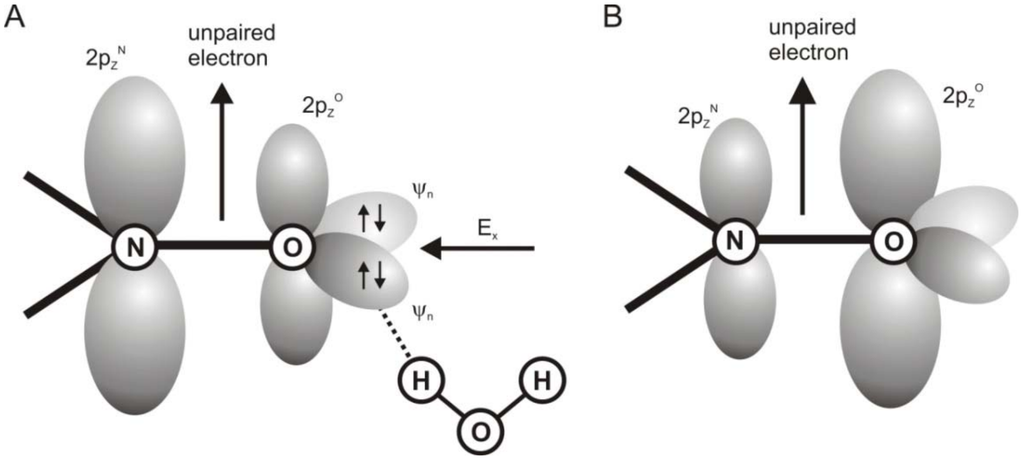

Figure 2.8 Schematic representation of the spin label N-O bond in polar (A) and non-polar environment (B). The oxygen 2s, $2p_x$ and $2p_y$ orbitals superimpose to the non-bonding lone pair orbitals ψ_n. (A): The external electric field component E_x is caused by the polar micro-environment which shift the π-electron density along the N-O bond towards the N-atom represented by increased orbitals. (B): The π-electron density is shifted towards the O-atom. (Figure based on [6]).

In particular, the hyperfine splitting A_{zz} reflects the strength of the hyperfine coupling. Depending on the spin label micro-environment a local electric field component E_x along the N-O bond is established as illustrated in Fig. 2.8. A high polarity in the micro-environment causes a shift of the π-electron density along the N-O bond towards the N-atom and consequently to a stronger hyperfine interaction between the electron and the N-atom ($I = 1$). In contrast, a low polarity results in a shift of the π-electron density towards the O-atom and therefore a weaker hyperfine coupling with the N-atom. Thus, a high A_{zz} value is evident for a strong hyperfine coupling and can be associated with a high accessibility to water molecules. A low A_{zz} value is evident for a weak hyperfine coupling and a low accessibility to water molecules.

Furthermore, the dipolar interaction for spins in a 1-2 *nm* distance range leads to a line broadening of the spectral lines. Decreasing interspin distances results in a stronger dipolar coupling ($\omega_{DD} \propto r^{-3}$) and a significantly line broadening as depicted in Fig. 2.9. Distance distributions as well as the values for the hyperfine splitting A_{zz} are obtained by fitting a simulated spectrum to the experimental one. The fitting is performed according to the simulation of EPR spectra in the slow motion regime utilizing the program DipFit[15]. The line broadening and hence the dipolar interaction is obtained by a convolution with a Pake pattern according to the respective interspin distance.

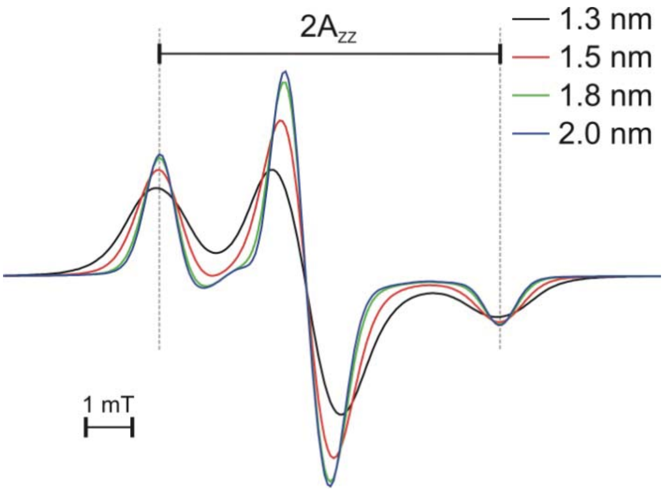

Figure 2.9 Simulated low temperature (T = 160 *K*) *cw* EPR powder spectra corresponding to interspin distances of 1.3 *nm* (black line), 1.5 *nm* (red line), 1.8 *nm* (green line) and 2.0 *nm* (blue line), respectively. Spectra are obtained by using DipFit with equal g- and A-tensor elements and variable interspin distances. All plots are normalized by spin number.

2.2.4 Pulse EPR spectroscopy

In contrast to the previously described *cw* EPR spectroscopy, in pulse EPR experiments microwave pulses are applied on the nanosecond time scale under the condition of a constant external magnetic field B_0. In this work, double electron electron resonance (DEER) experiments have been performed to determine interspin distances in the 2-8 *nm* range. These measurements are based on the selective excitation of two interacting spin fractions A and B using two different frequencies, the observer frequency ν_{obs} and the pump frequency ν_{pump},.

4-pulse double electron electron resonance (DEER)

In DEER experiments the spin fractions A and B are excited selectively with either the observer frequency ν_{obs} or the pump frequency ν_{pump}. Thereby, the pump frequency ν_{pump} is positioned at the maximum of the echo-detected nitroxide EPR absorption spectrum and the observer frequency ν_{obs} at the low field local maximum which result in a 65 MHz frequency offset as depicted in Fig. 2.10. The excitation of the pump spins B results in a resonance frequency shift of the dipolar coupled spins A. Observing the effect on the A spins enables the calculation of interspin distances.

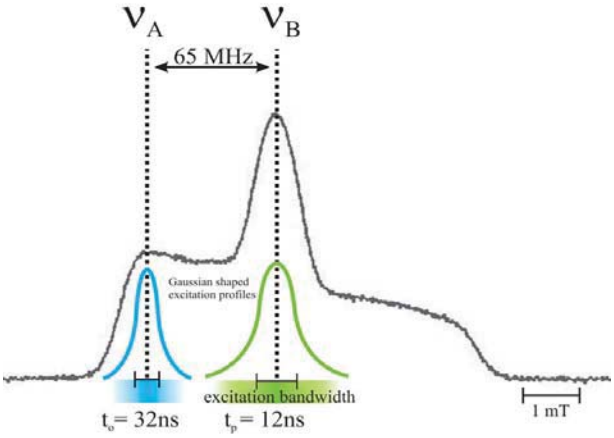

Figure 2.10 In a 4-pulse DEER experiment applied microwave pulses plotted in the echo-detected nitroxide EPR absorption spectrum. The observer frequency is separated by 65 MHz from the pump frequency.

Starting from a system with its equilibrium magnetization M_0 aligned along the z-axis a series of four microwave pulses[16] (cf. Fig. 2.11) are applied successively according to

$$\frac{\pi}{2}(\nu_{obs}) - \tau_1 - \pi(\nu_{obs}) - t - \pi(\nu_{pump}) - (\tau_1 + \tau_2 - t) - \pi(\nu_{obs}) - \tau_2 - echo. \quad 2.42$$

The Hahn-echo sequence, consisting of the first two pulses with the time delay of τ_1 at the observer frequency ν_{obs}, creates the spin echo which is also called Hahn-echo after another time delay τ_1 (Fig. 2.11). The π-pulse after time $2\tau_1+\tau_2$ leads to the refocused and monitored echo signal at $2\tau_1+2\tau_2$. Applying a π-pulse at the pump frequency ν_{pump} selectively excites the spin fraction B which cause a resonance frequency shift of the dipolar coupled spin fraction A. For the experimental DEER signal $V(t)$ the echo amplitude is determined in dependence of time t, corresponding to the pump pulse position[17]. Different t values result in a modulation of the detected echo signal with the dipolar frequency $\omega_{DD} \propto r^{-3}$.

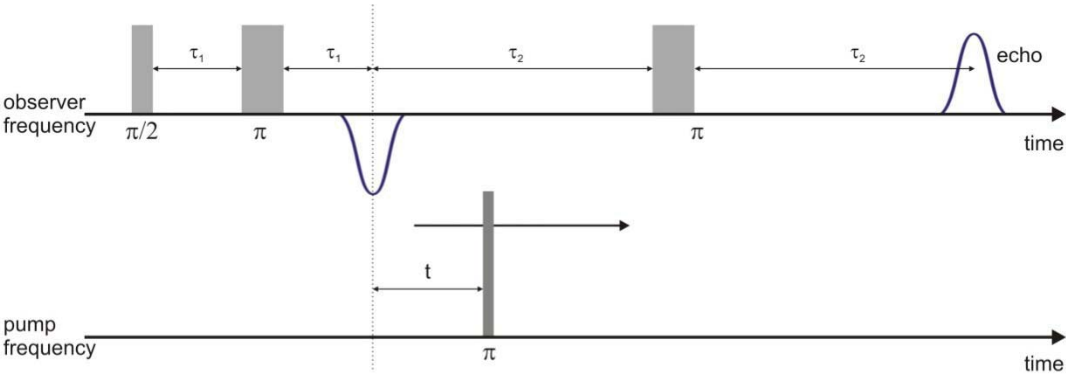

Figure 2.11 Schematic overview of the 4-pulse DEER sequence. See text for further details.

Pulse EPR spectra analysis

Information about the interspin distances are derived by analyzing the dipolar interaction between spin species A and B. The experimental DEER signal

$$V(t) = F(t)B(t) \quad 2.43$$

is composed of an intramolecular contribution $F(t)$, modulated with ω_{DD}, and an unmodulated background contribution $B(t)$[3, 18]. The background contribution $B(t)$ takes into account the homogeneous distributed molecules within the sample and therefore the homogeneous distributed interspin distances between the spins. The superposition of all different ω_{DD} modulated signals related to the variety of interspin distances results in an exponential decay of

$$B(t) = e^{-kt^{D/3}} \tag{2.44}$$

with

$$k = \frac{8\pi^2 \mu_B^2 g_A g_B}{9\sqrt{3}\hbar} C\lambda \tag{2.45}$$

considering the background dimensionality D, the $g_{A/B}$-factor of spin species A and B, respectively, the spin concentration C and the fraction of spins λ excited by the pump pulse[19]. For oligonucleotides the background dimensionality is regarded as D=3[20]. The modulated contribution $F(t)$ has to be separated from the unmodulated one by division of $V(t)$ by $B(t)$ for further analysis. In this process, a distance distribution $P(r)$ has to be fitted to $F(t)$. One possibility to deal with this ill-posed problem is the so-called Tikhonov regularization[21, 22] as utilized in the program DeerAnalysis[23]. For this purpose the function

$$G_\alpha(P) = \|S(t) - F(t)\|^2 + \alpha \left\| \frac{d^2}{dr^2} P(r) \right\|^2 \tag{2.46}$$

has to be minimized, including the root mean square deviation (RMSD) between a simulated spectrum $S(t)$ and the experimental background corrected spectrum $F(t)$ and the square norm of the second derivative of $P(r)$ as a measure for the smoothness of the distance distribution. The second term is weighted by the so-called regularization parameter α which regulates the smoothness. To define the best value for the regularization parameter, $\log(\|S(t) - F(t)\|^2)$, is plotted versus $\log(\|d^2/dr^2\, P(r)\|^2)$ resulting in a L-shaped curve. The best compromise between resolution of $P(r)$ and smoothness corresponds to the kink of the L-curve.

2.3 Molecular dynamics (MD) simulation

EPR spectroscopy as an experimental technique is limited to local information about the dynamic of the spin label side chains, their immediate environment and intramolecular distances. A complementary method such as molecular dynamics (MD) simulations allows a detailed interpretation of experimental results, to make predictions in experimentally hardly accessible regions and deliver insight into the dynamics of all atoms of the molecule under investigation. For instance, the effects induced by spin labeling on the labeled structure can be studied and experimental distance measurements can be compared to simulated ones.

For this purpose, Newton's classical equation of motion

$$F_n = -\left(\frac{\partial}{\partial r_n} E(r_n)\right) = m_n \frac{d^2}{dt^2} r_n(t) \qquad 2.47$$

has to be solved iteratively using a proper integrating algorithm, where m is the mass of the atom n and $\frac{d^2}{dt^2} r_n(t)$ the acceleration due to the Force F_n. The potential energy $E(r_n)$, the derivative of the force F_n with respect to the coordinates of the atom n, is defined by the so-called MD force fields. These force fields comprise pre-calculated parameters such as force constants (k), equilibrium bond lengths (r_0), angles (θ_0, γ_0) and charges (q) for the interactions between the atoms of the molecule. Different force fields are optimized for specific conditions and classes of molecules. In general, the interactions are divided into effects between covalently bonded atoms and atoms which are non-bonded or separated by three or more covalent bonds[24]

$$E = E_{bonded} + E_{non-bonded}. \qquad 2.48$$

The bonded interactions comprehend stretching, bending and rotations around chemical bonds (cf. Fig. 2.12). Van der Waals interaction and Coulomb interactions are summarized in the non-bonded contributions. As a result the potential can be written as

$$E = E_{bonds} + E_{angles} + E_{torsion} + E_{van\ der\ Waals} + E_{Coulomb} \qquad 2.49$$

In the Amber99force field[25-27], which is optimized for application on nucleic acids and used in this work, the bonded interactions represents the energy between covalently bonded atoms, the energy due to the geometry of electron orbitals involved in covalent bonding and the energy for twisting a bond due to bond order and neighboring bonds or lone pairs of electrons. These interactions are adequately represented by harmonic potentials. While the respective harmonic potential is

$$E = \sum_{bonds} \frac{1}{2} k_a \, (r - r_0)^2 \qquad 2.50$$

for bond stretching,

$$E = \sum_{angles} \frac{1}{2} k_b \, (\theta - \theta_0)^2 \qquad 2.51$$

for angle bending and

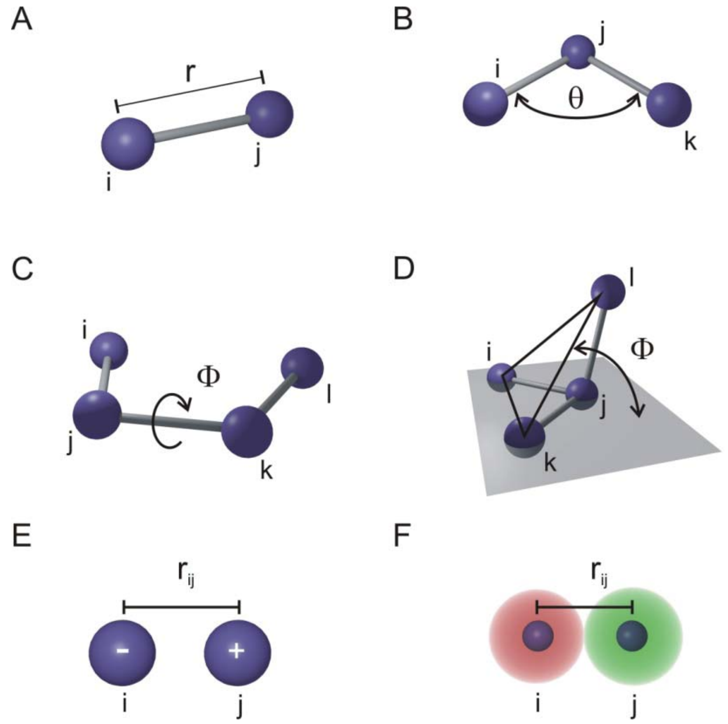

Figure 2.12 Overview of the force field contributions for bonded and non-bonded interactions. (A) bond potential, (B) angle potential, (C) dihedral potential, (D) improper dihedrals, (E) Coulomb potential and (F) van der Waals potential.

$$E = \sum_{torsions} \frac{1}{2} k_c \left[1 + \cos\left(n\Phi + \gamma_0\right)\right] \qquad 2.52$$

for the dihedral torsions of four successive bonded atoms with the multiplicity n, the angle Φ between the planes formed by the first three and the last there atoms and the phase angle γ_0. The index 0 of the harmonic potentials indicates the equilibrium value of the respective interaction. Furthermore, the torsion interaction in the Amber99 force field consists of three components: the general, the specific and the improper dihedrals. The first contribution considers the proper dihedral torsion between the four successive atoms. Its energy solely depends on the two middle atoms. All atoms are accounted for in the specific proper dihedrals. The last improper dihedral term regards four atoms which are not successive bonded and quantifies the planarity of the atoms (cf. Fig. 2.12, D).

The non-bonded interactions, the last two summands of equation 2.49, comprise the van der Waals and the Coulomb interactions between all atom pairs i and j. In particular, the Lennard Jones function of the van der Waals interaction

$$E = \sum_{vdW} \frac{A_{ij}}{{r_{ij}}^{12}} - 2\frac{B_{ij}}{{r_{ij}}^{6}} \qquad 2.53$$

with

$$A_{ij} = \varepsilon {r_{0ij}}^{12}$$
$$B_{ij} = \varepsilon {r_{0ij}}^{6} \qquad 2.54$$

includes repulsive and attractive forces between atoms pairs i and j where r_{ij} is the distance between atoms i and j, r_{0ij} the equilibrium distance and ε the potential well depth. The factor of 2 in equation 2.53 ensures an equilibrium distance of r_{0ij}. For the term of the Coulomb interaction

$$E = \sum\nolimits_{Coulomb} \frac{q_i q_j}{4\pi\varepsilon_0 r_{ij}} \qquad 2.55$$

the charges are represented by single point charges q_i. Consequently, the Amber99 force field has the functional form

$$\begin{aligned} E = \sum_{bonds} \frac{1}{2} k_a\,(r - r_0)^2 + \sum_{angles} \frac{1}{2} k_b\,(\theta - \theta_0)^2 + \sum_{torsions} \frac{1}{2} k_c\,[1 + \cos\,(nw + \gamma_0)] \\ + \sum_{j=1}^{N-1} \sum_{i=j+1}^{N} \left\{ \left[\left(\frac{A_{ij}}{r_{ij}} \right)^{12} - 2 \left(\frac{B_{ij}}{r_{ij}} \right)^{6} \right] + \frac{q_i q_j}{4\pi\varepsilon_0 r_{ij}} \right\} \end{aligned}$$

2.56

Time evolution and therefore the dynamics of the system under investigation in MD simulations is implemented by the successive calculation of the velocities $\frac{d}{dt} r(t)$ at time step $n - 1$ and coordinates $r(t)$ at time step n. The integration for all atoms provides the dynamics of the whole molecule as a function of time, the so-called trajectory. For this purpose, the time steps of the integration have to be small enough to cover the fastest oscillation in the system. For most MD simulations the time steps are in the 1-2 *fs* time range.

2.4 References

[1] M. A. Hemminga, G. Jeschke, J. Strancar, P. G. Fajer, L. Brown, L. Song, E. Bordignon, H.-J. Steinhoff, T. I. Smirnova, A. I. Smirnov, M. I. Fajer, K. L. Sale, M. J. Nilges, K. Mattson, R. L. Belford, J. H. Freed, S. Stoll, A. Schweiger. *Biological Magnetic Resonance - Vol. 27: ESR Spectroscopy in Membrane Biophysics,* (Eds.: M. A. Hemminga and L. J. Berliner), Springer, **2007**, p. -379.

[2] Jeschke, Gunnar and Spiess, Hans Wolfgang. Einführung in die ESR-Spektroskopie. **1998**, 1-243.

[3] A. Schweiger, G. Jeschke. *Principles of Pulse Electron Paramagnetic Resonance,* (Ed.: Oxford University Press), **2001**.

[4] G. R. Luckhurst. Biradicals as Spin Probes, In: (Ed.: L. J. Berliner), New York, Academic Press, **1976**.

[5] L. J. Berliner. *Spin Labeling II: Theory and Applications,* New York, Academic Press, **1979**, p. 1.

[6] M. Plato, H.-J. Steinhoff, C. Wegener, J. T. Törring, A. Savitsky, K. Möbius. *Mol. Phys.* **2002**, *100*(23), 3711-3721.

[7] S. Böhme, Dissertation, Fachbereich Biologie, Universität Osnabrück . **2010**.

[8] M. D. Rabenstein, Y.-K. Shin. *Proc. Natl. Acad. Sci. USA* **1995**, *92*(18), 8239-8243.

[9] L. J. Libertini, O. H. Griffith. *J. Chem. Phys.* **1970**, *53*(4), 1359-1367.

[10] C. Abé, Dissertation, Fachbereich Physik, Universität Osnabrück **2010**.

[11] C. P. Slichter. *Principles of Magnetic Resonance,* (Ed.: Springer), New York, **1996**.

[12] J. H. Freed, G. V. Bruno, C. F. Polnaszek. *The Journal of Physical Chemistry* **1971**, *75*(22), 3385-3399.

[13] J. H. Freed. Theory of Slow Tumbling ESR Spectra for Nitroxides, In: (Ed.: L. J. Berliner), *Spin Labeling: Theory and Applications,* New York, Academic Press, **1976**, pp. 53-132.

[14] H. S. Mchaourab, M. A. Lietzow, K. Hideg, W. L. Hubbell. *Biochemistry* **1996**, *35*(24), 7692-7704.

[15] H.-J. Steinhoff, N. Radzwill, W. Thevis, V. Lenz, D. Brandenburg, A. Antson, G. G. Dodson, A. Wollmer. *Biophys. J.* **1997**, *73*(6), 3287-3298.

[16] M. Pannier, S. Veit, A. Godt, G. Jeschke, H. W. Spiess. *J. Magn. Res.* **2000**, *142*(2), 331-340.

[17] G. Jeschke, Y. Polyhach. *Physical Chemistry Chemical Physics* **2007**, *9*(16), 1895-1910.

[18] B. E. Bode,Johann Wolfgang Goethe-Universität in Frankfurt am Main . **2008**.

[19] A. D. Milov, Y. D. Tsvetkov. *Appl. Magn. Reson.* **1997**, *12*(4), 495-504.

[20] Y. Polyhach, A. Godt, C. Bauer, G. Jeschke. *J. Magn. Res.* **2007**, *185*(1), 118-129.

[21] G. Jeschke, G. Panek, A. Godt, A. Bender, H. Paulsen. *Appl. Magn. Reson.* **2004**, *26*(1-2), 223-244.

[22] Y. W. Chiang, P. P. Borbat, J. H. Freed. *J. Magn. Res.* **2005**, *172*(2), 279-295.

[23] Jeschke, Gunnar. DeerAnalysis 2008. **2008**, -36. 24-7-2008.

[24] A. R. Leach. *Molecular Modelling: Principles and Applications,* (Ed.: Prentice Hall), **2001**.

[25] E. J. Sorin, V. S. Pande. *Biophys. J.* **2005**, *88*(4), 2472-2493.

[26] S. J. Weiner, P. A. Kollman, D. A. Case, U. C. Singh, C. Ghio, G. Alagona, S. Profeta, P. Weiner. *J. Am. Chem. Soc.* **1984**, *106*(3), 765-784.

[27] W. D. Cornell, P. Cieplak, C. I. Bayly, I. R. Gould, K. M. Merz, D. M. Ferguson, D. C. Spellmeyer, T. Fox, J. W. Caldwell, P. A. Kollman. *J. Am. Chem. Soc.* **1995**, *117*(19), 5179-5197.

3

The synthetic tetracycline riboswitch: a *cw* EPR spectroscopy study

3.1 Introduction

The fundamental function of RNA as the so-called messenger RNA (mRNA) is to mediate the translation of the genetic information from DNA into proteins. In 2002 Breaker and coworkers discovered that RNA is also able to control the implementation of the genetic information by regulating gene expression by the formation of RNA-based switches[1]. These RNA-based switches or riboswitches are primarily located in the 5' untranslated region (UTR) of prokaryotic mRNAs and form three-dimensional binding pockets for their specific ligands. Ligand binding leads to conformational changes which interfere with gene expression either by premature termination of transcription or inhibition of translation initiation[2] as depicted in Fig. 3.1.

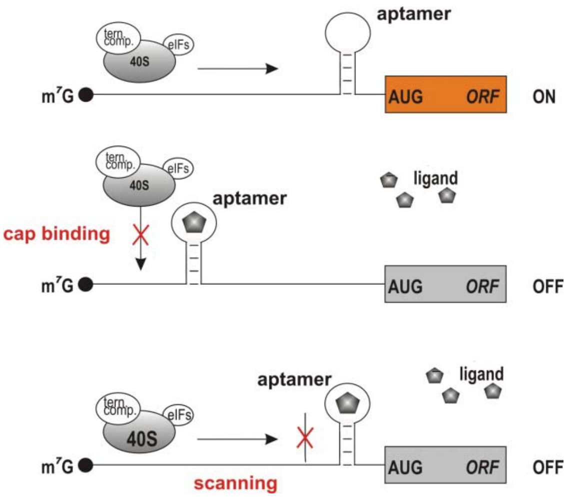

Figure 3.1 Aptamer-ligand mediated translational regulation. Regulation is not affected by the insertion of the aptamer into the non-coding region of the mRNA (top). After ligand addition the aptamer-ligand-complex becomes an obstacle for the ribosome binding (centre) or the movement along the non-coding region (below).

The discovery of these RNA switches established a wide range of applications in diagnostics, medicine and research[3]. RNA switches are ideal suited as highly sensitive biosensors[4]; they specifically recognize and bind a wide range of target molecules, like magnesium ions, cofactors, amino acids or nucleobases. Synthetic riboswitches, so-called aptamers, are isolated by SELEX (Systematic Evolution of Ligands by EXponential enrichment) from a random pool of RNA molecules. Only these which specifically bind to previously defined ligands with high affinity and selectivity are enriched[5, 6]. Like natural riboswitches they are able to adopt complex three-dimensional conformations to provide preformed binding pockets and clefts for the specific recognition and binding of their ligands [7, 8]. Ligand binding is often accompanied by a structural rearrangement of the RNA aptamer[9]. The tetracycline (Tc) binding aptamer investigated in this work has been used as a synthetic riboswitch for conditional gene expression in yeast. It inhibits either translation initiation[10, 11] or pre-mRNA splicing[10]. Its ligand Tc inhibits prokaryotic translation[12, 13] and is used as a therapeutic agent of low toxicity[14]. The aptamer binds Tc with a dissociation constant of ~0.8 *nM* and has a stoichiometry of 1:1 (Tc:pre-structured RNA aptamer)[15]. The aptamer is composed of three helices (stems P1, P2 and P3), two single stranded joining regions (J1-2 and J2-3) and the loop L3 as depicted in Fig. 3.2[16, 17]. It has been shown that the stems set up the scaffold of the aptamer already in the absence of Tc and does not possess direct contact to the ligand. The regions J1-2 and J2-3 form an irregular helix, which enables tertiary contacts to nucleotides from L3 in a pseudoknot like manner. The overall structure resembles that of an inverted "h" with Tc bound at the junction (cf. Fig. 3.2).

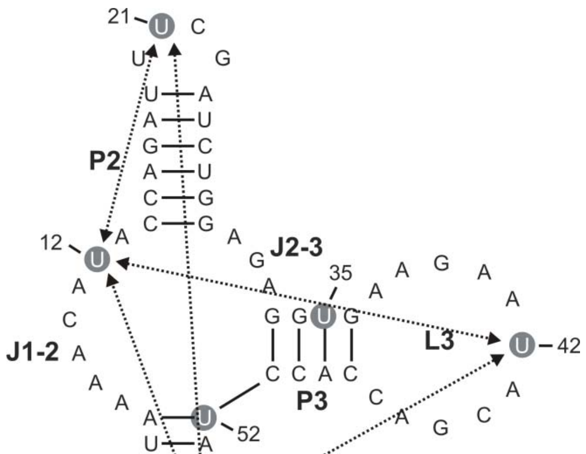

Figure 3.2 Secondary structure predicted for the Tc aptamer (adapted and modified from[16]). Thiouridines (s4U) spin labeled with MTS are marked by full grey circles. By *cw* EPR spectroscopy at 160 *K* investigated doubly labeled mutants are connected by black arrows.

However, the nature of the putative Tc induced conformational transition is still unknown. Up to now, several techniques have been used for high-resolution analysis of various RNA structures such as solid state NMR spectroscopy, X-ray crystallography, and fluorescence spectroscopy. In the last years, electron paramagnetic resonance (EPR) spectroscopy in combination with site-directed spin

labeling (SDSL) has emerged as a powerful tool to investigate RNA/DNA under conditions close to the physiological state. Continuous wave (*cw*) EPR spectroscopy reveals information about the mobility of the spin label side chains[18-20], the polarity of their micro-environment[21, 22], and about intramolecular distances between two spin label side chains in the distance range of 1-2 *nm*[23-26].
The aim of this study was to probe the dynamics and conformational changes of the spin labeled aptamer and polarity changes in the micro-environment of the spin label side chains upon ligand binding. Furthermore, EPR spectroscopy has been applied to distinguish between ion and ligand induced effects.

3.2 Results and Discussion

Introduction of nitroxide spin labels into the Tc aptamer

The (1-oxyl-2,2,5,5-tetramethylpyrroline-3-methyl)methanethiosulfonate (MTS) spin label was introduced post-synthetically by reaction of the 4-thiouridine modified RNA (s4U) as depicted in Fig. 3.3.

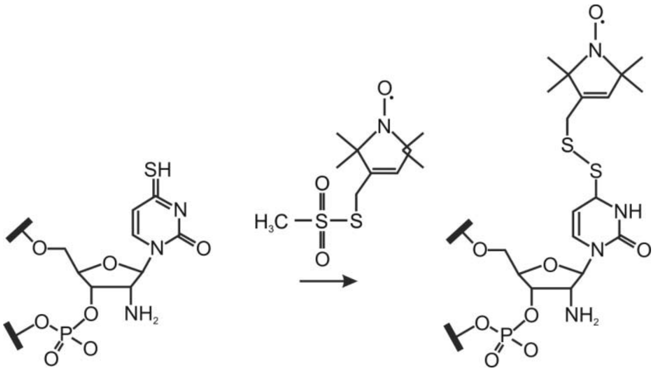

Figure 3.3 Strategy for the post-synthetically introduction of the MTS spin label using the selective reaction with 4-thiouridine.

Different sites (cf. Fig. 3.2) in all elements of the RNA aptamer were selected for introducing the nitroxide spin label, resulting in six single and five double labeled RNA mutants. Within stem P1 sites s4U52 and s4U56 were chosen, s4U12 inside of single stranded joining region J1-2, s4U21, and s4U35 within stems P2 and P3, respectively, and s4U42 in loop L3. The abbreviation s4U represents the modified nucleoside followed by its position within the sequence. Single and double labeled RNA mutants were investigated by *cw* EPR spectroscopy at room temperature (RT, 298K) and at low temperature (LT, 160 *K*), respectively. Changes of the overall spin label mobility and polarity in the micro-environment of the spin label side chains are first indications of structural rearrangements of the aptamer. Furthermore, possible conformational changes of the stem regions P1 and P2 with respect to the joint J1-2 indicated by small interspin distance changes can be traced with the double mutants s4U12/s4U21 and s4U12/s4U56. The relative orientation of stems P1 and P2 can be followed with the double mutant s4U21/s4U56. Pair s4U42/s4U56 was chosen to study the movement of the opposing loop region L3 with respect to the stem region P1. Finally, the interspin distance of s4U12/s4U42 should be sensitive to a possible rearrangement of loop L3 with respect to the single stranded region J1-2.

Cw EPR at room temperature reveals ion-induced changes in spin label mobility

In order to probe the local structure of the RNA aptamer, *cw* EPR experiments at RT were performed. To discriminate between ion and ligand induced effects all experiments were carried out in three consecutive stages. First, the aptamers were measured in water, then in Mg^{2+}-containing buffer in the absence and in the presence of Tc. All spectra exhibit sharp lines which indicate a high nitroxide mobility (Fig. 3.4), also reflected by the values of the simulated reorientational correlation time of the nitroxide spin label given in Table 3.1 (see “materials and methods” for details).

	τ (H_2O)/ns	τ (Mg^{2+})/ns	τ (Mg^{2+} + Tc)/ns
s4U12	0.23 ± 0.05	0.23 ± 0.05	0.24 ± 0.05
s4U21	0.23 ± 0.02	0.35 ± 0.02	0.39 ± 0.02
s4U35	0.35 ± 0.04	0.27 ± 0.04	0.26 ± 0.04
s4U42	0.17 ± 0.03	0.17 ± 0.03	0.15 ± 0.03
s4U52	0.21 ± 0.02	0.15 ± 0.02	0.18 ± 0.02
s4U56	0.25 ± 0.04	0.25 ± 0.04	0.21 ± 0.04

Table 3.1 Simulated reorientational correlation time τ obtained from room temperature spectra (T=293 *K*) in water and in a Mg^{2+}-containing buffer in the absence and in the presence of Tc, respectively.

Hence, the motional freedom of the nitroxide spin labels is hardly restricted by interaction with the local structure of the RNA aptamer. The values for the single

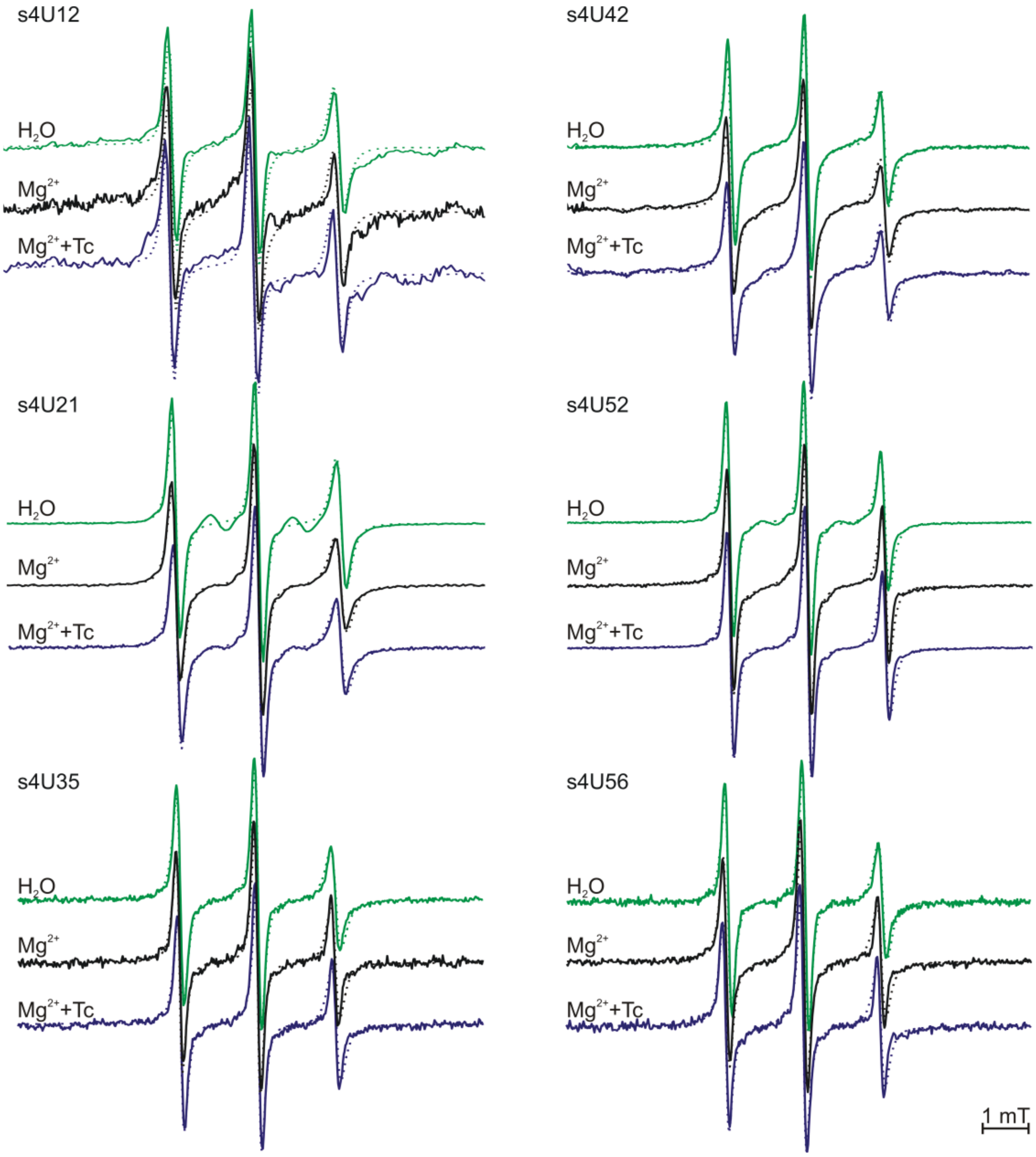

Figure 3.4 Comparison of experimental determined *cw* EPR spectra at 298 *K* (solid lines) and simulated EPR spectra (dotted lines) in water (green lines) and in a Mg^{2+}-containing buffer in the absence (black lines) and in the presence of Tc (blue lines), respectively. All plots are normalized by amplitude.

labeled mutants s4U12, s4U42 and s4U56 of 0.23 ns, 0.17 *ns* and 0.25 *ns*, respectively, do not change in their limits of error upon the addition of Mg^{2+} and of Tc. In contrast, a Mg^{2+}-induced increase of the reorientational correlation time from 0.23 *ns* to 0.35 *ns* is visible for s4U21, but upon addition of Tc no further changes take place. Furthermore, for s4U35 and s4U52 a decrease of the spin label reorientational correlation time from 0.35 *ns* to 0.27 *ns* and from 0.21 *ns* to 0.15 *ns* upon Mg^{2+} addition, respectively, is observed. Again, no further changes occur in the presence of Tc. Our results clearly indicate ion-induced changes of the spin label mobility most likely caused by conformational changes in the aptamer structure. No additional changes of the nitroxide dynamics and therefore the RNA structure upon Tc-binding are detectable, leading to the conclusion that the aptamer adapts a conformation in the Mg^{2+}-containing buffer which is very similar to that one in the presence of Tc. Thus, the Tc-dependent aptamer can be classified as type I [27]. These types of riboswitches exhibit a well defined and localized binding pocket. The global conformation is already pre-structured and ligand binding induces only conformational changes to a small region. It was shown for a type I riboswitch that ligand binding leads only to conformational changes of a limited set of nucleotides within the binding pocket of a purine riboswitch [28]. Apart from that, conformational changes upon Tc-binding cannot be precluded at this point. A very weak interaction of the nitroxide ring with the aptamer structure and/or the high spin label mobility could prevent the detection of small conformational changes taking place upon binding of Tc. Furthermore, it is possible that the spin label affects the ligand binding itself and prevents small conformational changes within the binding pocket as indicated by the decreased Tc-binding constants for the double mutants s4U12/s4U21, s4U12/s4U56 compared to the unmodified RNA (cf. Table 4.1).

Ion-induced polarity changes in the environment of the spin label

Low temperature (LT) *cw* EPR experiments of five double labeled RNA mutants in water and in the absence or in the presence of Tc in a Mg^{2+}-containing buffer, respectively, have been performed to reveal information about the polarity in the micro-environment of the spin label side chains. Changes in the polarity are reflected by changes of the hyperfine splitting values A_{ZZ} as given in Table 3.2. For the different double labeled RNA mutants the values vary from 3.6 *mT* to 3.8 *mT*. Thereby, the A_{ZZ} values for the double mutants are the average for the A_{ZZ} values of the single mutants. However, the A_{ZZ} for the double mutants provide the necessary information about global structural changes. The spectra detected for the spin labeled RNA mutants are shown in Fig. 3.5. All values of the hyperfine splitting A_{ZZ} exhibit a high polarity, the nitroxide spin labels are highly accessible towards water molecules. An increase of the hyperfine splitting A_{ZZ} is evident for s4U12/s4U21, s4U12/s4U56, s4U21/s4U56 and s4U42/s4U56 upon Mg^{2+} addition, indicating an increase of the polarity in the environment. Moreover, in the presence of the ligand the values of the hyperfine splitting A_{ZZ} and therefore the polarity of the environment are retained. In the case of double mutant s4U12/s4U42 the hyperfine splitting A_{ZZ} value is almost identical at all consecutive stages. Again, these results give strong evidence for Mg^{2+}-induced conformational changes of the aptamer. A rearrangement of the aptamer conformation upon Tc-binding could not be resolved. This is in line with previous studies of the *glmS* ribozyme where the formation of a highly conserved ribozyme core was shown, and the ligand bound to a prefolded, solvent-accessible pocket. The ribozyme structures in the absence and in the presence of the ligand superimpose closely [29, 30].

	A_{ZZ} (H_2O)/mT	A_{ZZ} (Mg^{2+})/mT	A_{ZZ} (Mg^{2+} + Tc)/mT
s4U12/s4U21	3.62 ± 0.05	3.77 ± 0.05	3.78 ± 0.05
s4U12/s4U42	3.75 ± 0.05	3.77 ± 0.05	3.76 ± 0.05
s4U12/s4U56	3.63 ± 0.05	3.80 ± 0.05	3.80 ± 0.05
s4U21/s4U56	3.74 ± 0.05	3.81 ± 0.05	3.82 ± 0.05
s4U42/s4U56	3.68± 0.05	3.80 ± 0.05	3.81 ± 0.05

Table 3.2 Simulated hyperfine splitting A_{ZZ} obtained from low temperature spectra (T=160 *K*) of double labeled RNA mutants in water and in a Mg^{2+}-containing buffer in the absence and in the presence of Tc, respectively.

In addition to polarity determination, *cw* EPR experiments at LT provide information about possible changes of interspin distances in the range of 1-2 *nm*. For RNA double mutant s4U12/s4U42 fitting of the simulated dipolar broadened EPR spectra (cf. Fig. 3.5) to the experimental one utilizing the program DipFit yields a distance distribution centered at 1.4 nm (± 0.2 nm) at all consecutive stages and a fraction of the single spin labeled component of 30-40%. However, the interspin distances within all other RNA mutants exceed the value of 2 *nm* in the absence and in the presence of Tc. Hence, pulse EPR spectroscopy is the improved method for interspin distance determination up to 8 *nm* and will be applied in the following chapter.

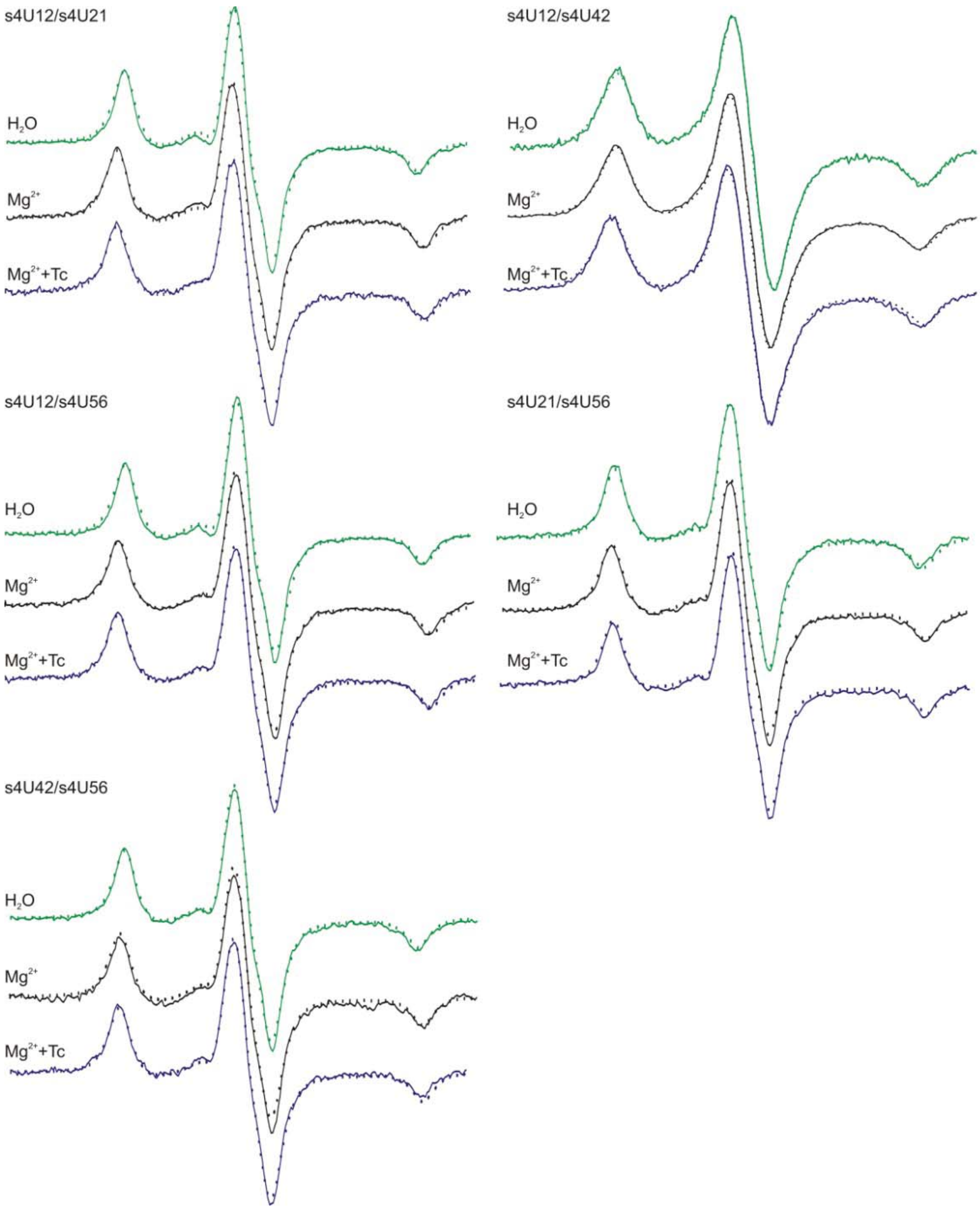

Figure 3.5 Comparison of experimental determined *cw* EPR spectra at 160K (solid lines) and simulated EPR spectra (dotted lines) in water (green lines) and in a Mg^{2+}-containing buffer in the absence (black lines) and in the presence of Tc (blue lines), respectively. All plots are normalized by amplitude.

3.3 Conclusion and Outlook

Here, *cw* EPR spectroscopy in combination with site-directed spin labeling have revealed ion-induced changes of the spin label mobility and polarity due to conformational changes in the aptamer structure. Further changes in the presence of the ligand Tc could not be resolved, indicating that the aptamer conformation in the presence of Tc resembles that in the absence of the ligand. Furthermore, for RNA double mutant s4U12/s4U42 the interspin distance of 1.4 nm remains stable upon ligand addition. Nevertheless, small local conformational rearrangements upon Tc-binding cannot be excluded at this point. To determine interspin distances in the absence and in the presence of Tc, pulse EPR spectroscopy will be applied to a set of RNA double mutants. This method extends the measurable distance range up to 8 *nm*[31]. Furthermore, applying a spin label strategy seems to be necessary with a proposed smaller disturbance of the bound spin label to the ligand binding. Within a new spin label strategy the spin label should reduce motion that conceals local rearrangements without sterical perturbation of the RNA structure. The post-synthetic introduction of a spin label by reaction with 2'-aminouridine modified RNA is a suitable modification of the existent strategy due to sterical reasons which is reflected in the Tc-binding constant for the RNA double mutant C’14/A’41 of 4.2 *nM* resembling the Tc-binding constant of 0.77 *nM* for the unmodified RNA (cf. Table 4.1).

3.4 Materials and Methods

Sample preparation

The RNA was dissolved in 20 *mM* potassium phosphate buffer, 100 *mM* NaCl, 5 *mM* $MgCl_2$ (pH 7.5) yielding a 30-70 *μM* final concentration for single mutants and 110 -150 *μM* for double mutants. The RNA mutants were incubated at 65 °C for 5 *min* followed by slow-cooling to RT in order to allow homogeneous tertiary structure formation. Complex formation with a 2-fold excess of Tc was assured by an additional incubation for 5 *min* at 37 °C and slow-cooling to RT. Sample volumes of 10 *μl* and 40 *μl* were loaded into EPR quartz capillaries for *cw* EPR measurements at RT and LT, respectively. For *cw* EPR experiments at LT samples were frozen in liquid nitrogen before insertion into the resonator.

EPR measurements

Cw EPR spectra at RT were recorded using a Magnettech Miniscope MS200 X-band spectrometer equipped with a rectangular TE102 resonator. The microwave power was set to 10 *mW* and the B-field modulation amplitude adjusted to 0.15 *mT*. *Cw* EPR spectra for the determination of interspin distances in the range of 1-2 *nm* and the hyperfine splitting A_{ZZ} were recorded at 160 *K* using a homemade X-band EPR spectrometer equipped with a Super High Sensitivity Probehead (Bruker). A continuous flow helium cryostat (ESR 900, Oxford Instruments) in combination with a temperature controller (ITC 503S, Oxford Instruments) allowed temperature stabilization, while the magnetic field was measured by a B-NM 12 B-field meter (Bruker). The microwave power was adjusted to 0.2 *mW* and the B-field modulation amplitude to 0.25 *mT*.

Analysis of *cw* EPR at low temperature

Fitting of the simulated dipolar broadened EPR spectra to the experimental low temperature *cw* EPR spectrum using the program DipFit[26] reveal the average interspin distance in the range of 1-2 *nm* as described before. DipFit determines best-fit parameters for the interspin distance and distance distribution considering a Gaussian distribution of interspin distances and the hyperfine splitting A_{ZZ}. During the fitting procedure, the *g*-tensor values, the A_{XX} and A_{YY} values of the hyperfine tensor and the Lorentzian and Gaussian line width parameters are fixed to the values found for the reference spectrum s4U52. In detail, A_{XX} and A_{YY} were fixed to 0.52 and 0.35 *mT*, respectively, whereas A_{ZZ} is variable in order to determine the polarity of the immediate spin label environment. The g-tensor values are set to g_{XX} = 2.0083, g_{YY} = 2.0071, g_{ZZ} = 2.0023. The EPR spectra are convoluted with a field-independent line shape function composed of a superposition of 28 % Lorentzian and 72 % Gaussian of 0.33 and 0.31 *mT* widths, respectively. The fraction of single spin-labeled component is variable.

Analysis of *cw* EPR at room temperature

Fitting of simulated EPR spectra to the experimental ones detected at 298 *K* was performed according to a Brownian model of isotropic reorientational diffusion of the nitroxide[18] with two distinct spectral components. Due to the fact that the experimental spectra reflect an almost isotropic reorientational motion of the nitroxide, the fraction of the component characterized by longer correlation times was in the range of 5-10%. For the fitting procedure the *g* and *A*-tensor values were fixed to values determined by analysis of the low temperature spectra, whereas rotational diffusion constants and the ratio of the two spectral components were allowed to vary. The reorientational correlation time τ_c was calculated from the obtained rotational diffusion constant *R* according to $\tau_c=(6 \times R)^{-1}$.

3.5 References

[1] W. Winkler, A. Nahvi, R. R. Breaker. *Nature* **2002**, *419*(6910), 952-956.
[2] A. Roth, R. R. Breaker. *Annu. Rev. Biochem.* **2009**, *78*, 305-334.

[3] J. E. Weigand, B. Suess. *Applied Microbiology and Biotechnology* **2009**, *85*(2), 229-236.

[4] S. Blouin, J. Mulhbacher, J. C. Penedo, D. A. Lafontaine. *ChemBioChem* **2009**, *10*(3), 400-416.

[5] A. D. Ellington, J. W. Szostak. *Nature* **1990**, *346*(6287), 818-822.

[6] C. Tuerk, L. Gold. *Science* **1990**, *249*(4968), 505-510.

[7] M. Famulok. *Curr. Opin. Struc. Biol.* **1999**, *9*(3), 324-329.

[8] D. J. Patel, A. K. Suri. *J Biotechnol* **2000**, *74*(1).

[9] T. Hermann, D. J. Patel. *Science* **2000**, *287*(5454), 820-825.

[10] B. Suess, S. Hanson, C. Berens, B. Fink, R. Schroeder, W. Hillen. *Nucl. Acids. Res.* **2003**, *31*(7), 1853-1858.

[11] P. Koetter, J. E. Weigand, B. Meyer, K.-D. e. e. d. Entian, B. s. s. d. Suess. *Nucl. Acids. Res.* **2009**, *37*(18).

[12] B. Epe, P. Woolley, H. Hornig. *FEBS Letters* **1987**, *213*(2), 443-447.

[13] C. M. T. Spahn, C. D. Prescott. *Journal of Molecular Medicine-Jmm* **1996**, *74*(8), 423-439.

[14] C. Berens, W. Hillen. *Eur J Biochem* **2003**, *270*(15), 3109-3121.

[15] M. Mueller, J. E. Weigand, O. Weichenrieder, B. b. b. d. Suess. *Nucl. Acids. Res.* **2006**, *34*(9), 2607-2617.

[16] S. Hanson, G. Bauer, B. Fink, B. Suess. *Rna-A Publication of the Rna Society* **2005**, *11*(4), 503-511.

[17] H. Xiao, T. E. Edwards, A. R. Ferre-D'Amare. *Chem. & Biol.* **2008**, *15*(10), 1125-1137.

[18] J. H. Freed. Theory of Slow Tumbling ESR Spectra for Nitroxides, In: (Ed.: L. J. Berliner), *Spin Labeling: Theory and Applications,* New York, Academic Press, **1976**, pp. 53-132.

[19] L. J. Berliner. *Spin Labeling II: Theory and Applications,* New York, Academic Press, **1979**, p. 1.

[20] L. J. Berliner, J. Reuben. *Biological Magnetic Resonance - Vol. 8: Spin Labeling Theory and Applications,* (Eds.: L. J. Berliner and J. Reuben), New York, Plenum Press, **1989**.

[21] M. Huber, J. T. Törring. *Chem. Phys.* **1995**, *194*(2-3), 379-385.

[22] H.-J. Steinhoff, A. Savitsky, C. Wegener, M. Pfeiffer, M. Plato, K. Möbius. *Biochim. Biophys. Acta* **2000**, *1457*, 253-262.

[23] C. Altenbach, K. J. Oh, R. J. Trabanino, K. Hideg, W. L. Hubbell. *Biochemistry* **2001**, *40*(51), 15471-15482.

[24] M. D. Rabenstein, Y.-K. Shin. *Proc. Natl. Acad. Sci. USA* **1995**, *92*(18), 8239-8243.

[25] H.-J. Steinhoff, O. Dombrowsky, C. Karim, C. Schneiderhahn. *Eur. Biophys. J.* **1991**, *20*(5), 293-303.

[26] H.-J. Steinhoff, N. Radzwill, W. Thevis, V. Lenz, D. Brandenburg, A. Antson, G. G. Dodson, A. Wollmer. *Biophys. J.* **1997**, *73*(6), 3287-3298.

[27] R. K. Montange, R. T. Batey. *Annual Review of Biophysics* **2008**, *37*, 117-133.

[28] C. D. Stoddard, S. D. Gilbert, R. T. Batey. *Rna-A Publication of the Rna Society* **2008**, *14*(4), 675-684.

[29] D. J. Klein, A. R. Ferre-D'Amare. *Science* **2006**, *313*(5794), 1752-1756.

[30] K. J. Hampel, M. M. Tinsley. *Biochemistry* **2006**, *45*(25), 7861-7871.
[31] M. Pannier, S. Veit, A. Godt, G. Jeschke, H. W. Spiess. *J. Magn. Res.* **2000**, *142*(2), 331-340.

4

Ligand induced conformational capture of a synthetic tetracycline riboswitch revealed by pulse EPR

Wunnicke D, Strohbach D, Weigand JE, Appel B, Feresin E, Suess B, Müller S, Steinhoff HJ (2011) *RNA* **17**:172-188.

4.1 Abstract

RNA aptamers are *in vitro* selected binding domains which recognize their respective ligand with high affinity and specificity. They are characterized by complex three-dimensional conformations providing preformed binding pockets which undergo conformational changes upon ligand binding. Small molecule binding aptamers have been exploited as synthetic riboswitches for conditional gene expression in various organisms. In the present study, double electron electron resonance (DEER) spectroscopy combined with site directed spin labeling was used to elucidate the conformational transition of a tetracycline aptamer upon ligand binding. Different sites were selected for post-synthetic introduction of either the (1-oxyl-2,2,5,5-tetramethylpyrroline-3-methyl) methanethiosulfonate by reaction with a 4-thiouridine modified RNA or of 4-isocyanato-2,6-tetramethylpiperidyl-N-oxid spin label by reaction with 2'-aminouridine modified RNA. The results of the DEER experiments indicate the presence of a thermodynamic equilibrium between two aptamer conformations in the free state and capture of one conformation upon tetracycline binding.

4.2 Introduction

Riboswitches are regulatory elements, which are primarily located in the 5' untranslated region (UTR) of prokaryotic mRNAs. They are complex folded single stranded RNA structures and can bind specific ligands, like magnesium ions, cofactors, amino acids or nucleobases. Ligand binding causes conformational changes which regulate gene expression, either through premature termination of transcription or inhibition of translation initiation[1]. Furthermore, aptamers exhibit properties comparable to antibodies[2, 3]. They are potential agents for disease diagnosis and treatment[4] and for biotechnological applications like biosensors[5]. Aptamers are also used as riboswitches for conditional gene regulation[6, 7]. Such RNA molecules are isolated by SELEX (Systematic Evolution of Ligands by EXponential Enrichment) from a random pool of RNA molecules[8, 9]. They specifically bind to previously defined ligands with high affinity and selectivity. This class of nucleic acid molecules adopts complex three-dimensional conformations to provide preformed binding pockets and clefts for the specific recognition and binding of their ligands, such as cofactors, amino acids, drugs or antibiotics[10, 11]. Ligand binding is often accompanied by structural rearrangement of the RNA aptamer[12].

The tetracycline (Tc)-binding aptamer investigated in the present work has been used as an RNA switch for conditional gene expression in yeast, either inhibiting translation initiation[13, 14] or pre-mRNA splicing[15]. The ligand Tc inhibits prokaryotic translation[16] and is used as a therapeutic agent of low toxicity[17]. The aptamer is biochemically well characterized; it binds its ligand with a dissociation constant of ~0.8 *nM* and has a stoichiometry of one molecule of Tc and one molecule of the pre-structured RNA aptamer[18]. The RNA aptamer comprises three helices (stems P1, P2 and P3), the single stranded joining regions J1-2 and J2-3 and the loop L3 (Fig. 4.1)[19, 20].

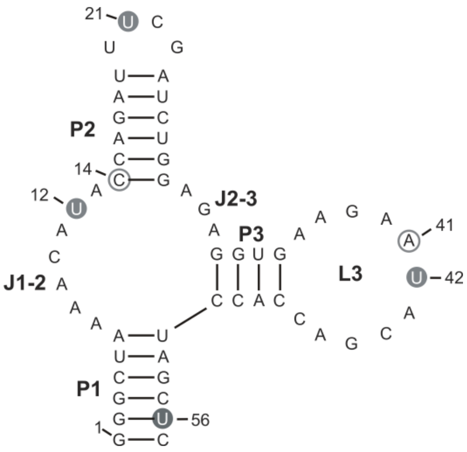

Figure 4.1 Secondary structure predicted for the Tc aptamer. Thiouridines (U) spin labeled with MTS are marked by full grey circles, 2'-aminouridine labeled with 4-isocyanato-TEMPO are depicted by open grey circles (adapted from Hanson *et al.*[19])

All three stem regions are not in direct contact to Tc and form the scaffold already in the absence of the ligand. An irregular helix consisting of the regions J1-2 and J2-3 possesses tertiary contacts to nucleotides from L3 in a pseudoknot like manner. The overall structure resembles that of an inverted “h” with Tc bound at the junction (cf. Fig. 4.1). However, the nature of the putative Tc induced conformational transition is still unknown.

Both, electron paramagnetic resonance (EPR) spectroscopy in combination with site-directed spin labeling (SDSL) and Förster resonance energy transfer (FRET) spectroscopy allow inter- and intramolecular distance measurements on the nanometer scale. FRET is based on the non-radiative energy transfer between two fluorophors which permit distance determination in the range of 1-10 *nm*[21]. Furthermore, single-molecule FRET provides information about the conformational dynamics of single biomolecules over time scales in the range of microseconds to seconds[22, 23]. The precision of this method is impaired by the uncertainty of the orientation factor and by the size of the fluorophors. EPR spectroscopy in combination with SDSL has been shown to be ideally suited to elucidate the conformations and conformational dynamics of biological systems such as proteins, protein complexes, DNA and RNA under physiological conditions[24-26]. By means of spin labeled folded DNA or RNA a nanometer distance ruler was developed[27-29], B/A conformational transitions of DNA[30] and DNA damages[31] were studied by double electron-electron resonance (DEER) spectroscopy[32] showing its high sensitivity towards small structural changes.

In the present study, we apply this technique to examine the dynamics and conformational transition of the spin labeled Tc aptamer upon ligand binding. Our results reveal the presence of a thermodynamic equilibrium between two aptamer conformations in the free state and a shift towards one conformation upon Tc binding.

4.3 Results

The aim of the present study is to probe the conformational changes of the Tc aptamer upon ligand binding. Therefore different sites (cf. Fig. 4.1) were selected for post-synthetic introduction of either the (1-oxyl-2,2,5,5-tetramethylpyrroline-3-methyl) methanethiosulfonate spin label (MTS) by reaction with 4-thiouridine modified RNA (s4U) or of 4-isocyanato-2,6-tetramethylpiperidyl-N-oxid (4-isocyanato-TEMPO) by reaction with 2'-aminouridine modified RNA as shown in Fig. 4.2.

Due to sterical reasons the approach involving the 2'-aminouridine modified RNA leads to a smaller disturbance of the bound spin label to ligand binding which is evident in the binding constant (see Table 4.1). The conformations and conformational changes of the overall aptamer structure were determined from interspin distances and distance changes within four RNA double mutants, s4U12/s4U21, s4U12/s4U56, s4U42/s4U56 and C’14/A’41. Spin labeled RNAs are named according to their spin labeled sites. The labeled nucleotide positions are indicated in the secondary structure shown in Fig. 4.1. The double mutants s4U12/s4U21 and s4U12/s4U56 were chosen to study possible conformational changes of the stem regions P1 and P2 with respect to the joint J1-2. The interspin distance of s4U42/s4U56 is sensitive to conformational rearrangement of the opposing loop region with respect to the stem region P1. Movement of the loop L3 with respect to the single stranded region J1-2 may be followed with the RNA double mutant C’14/A’41 with the spin label bound to the RNA sugar-phosphate backbone.

The Tc binding constants for the double mutants were determined by fluorescence titration spectroscopy to evaluate influences of spin labeling on ligand binding (see Table 4.1). For C′14/A′41 and s4U42/s4U56 the Tc binding constants resemble those of the unmodified RNA. Double mutants s4U12/s4U21 and s4U12/s4U56 show a decrease in the binding affinity. This is attributed to the spin label on position 12, as sites 21 and 56 are not part of the binding pocket. U12 does not directly contact Tc, but is involved in the organization of the overall structure of the aptamer by hydrogen-bonding to G31[20]. This contact might be disturbed in the spin labeled aptamer conformation. However, it has been shown that nucleotide exchanges on position 12 retain the regulatory activity of the aptamer[19] and the Tc binding constants for double mutants involving s4U12 are still in the nanomolar range (cf. Table 4.1).

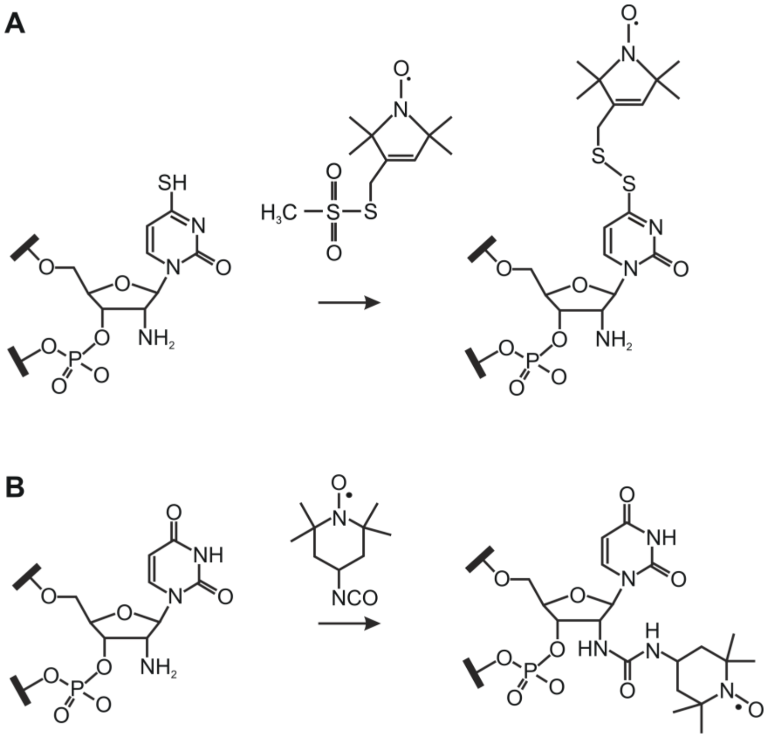

Figure 4.2 Strategy for the post-synthetic introduction of MTS using the selective reaction with 4-thiouridine (A) and of 4-isocyanato-TEMPO using the selective reaction with 2'-aminouridine (B).

The EPR spectra of the single mutants labeled with MTS (Fig. 4.3, A) are characterized by high motional freedom of the spin label side chains and the presence of only a single motional component. A decreased motional freedom of the

TEMPO spin label side chain at A′41 is obvious by the decreased amplitude ratio of the high field to the middle field resonance peaks (Fig. 4.3, B). For all single mutants the spin label mobility does not change upon Tc-binding which indicates that the reorientational motion of the spin labels is not influenced by the ligand. Also for the double mutants (Fig. 4.3, C-D) EPR spectral changes upon ligand binding were not observed.

	K_D / nM	Interspin distance without Tc/nm	Interspin distance with Tc/nm
wild type	0.77 ± 0.11[1]		
s4U12/s4U21	137 ± 10	2.9 ± 0.5 3.8 ± 0.4	(2.3 ± 0.4) 2.8 ± 0.5 (3.8 ± 0.5)
s4U12/s4U56	103 ± 16	3.8 ± 0.4 5.0 ± 0.5	4.9 ± 0.2
s4U42/s4U56	6.2 ± 0.7	4.8 ± 0.2	4.7 ± 0.2
C′14/A′41	4.2 ± 0.2	2.6 ± 0.3 (3.4 ± 0.2)	(2.7 ± 0.4) 3.6 ± 0.3

Table 4.1 Binding constants K_D of double labeled RNA mutants, and interspin distances determined in the absence and in the presence of tetracycline (Tc). Dominating interspin distance peaks are given with their estimated FWHM widths, peaks with decreased probability or shoulders are shown in parenthesis.
[1]published in Müller *et al.*[18]

DEER experiments were performed in the absence and in the presence of Tc, the corresponding results are depicted in Fig. 4.4. In Table 1 the values of the dominating interspin distances and of the estimated distributions widths FWHM are given. For s4U12/s4U21 in the absence of Tc a distance distribution with two shoulders centered at 2.9 *nm* (± 0.5 *nm*) and 3.8 *nm* (± 0.4 *nm*) is obvious. Binding of Tc reduces the population of the larger distance, and the average distance is shifted to a smaller value. The distance distribution for s4U12/s4U56 in the absence of Tc reveals two major peaks centered at 3.8 *nm* (± 0.4 *nm*) and 5.0 *nm* (± 0.5 *nm*), whereas in the presence of Tc a well defined single population with a mean distance of 4.9 *nm* (± 0.2 *nm*) is evident. The experimental result in absence of Tc indicates the presence of a thermodynamic equilibrium either of two conformers of the spin label, or of two aptamer conformations. Sites 12 and 56 are highly exposed and the spin label side chains do not experience any restriction of their reorientational motion due to the interaction with the ligand (cf. Fig. 4.3 and 4.5).

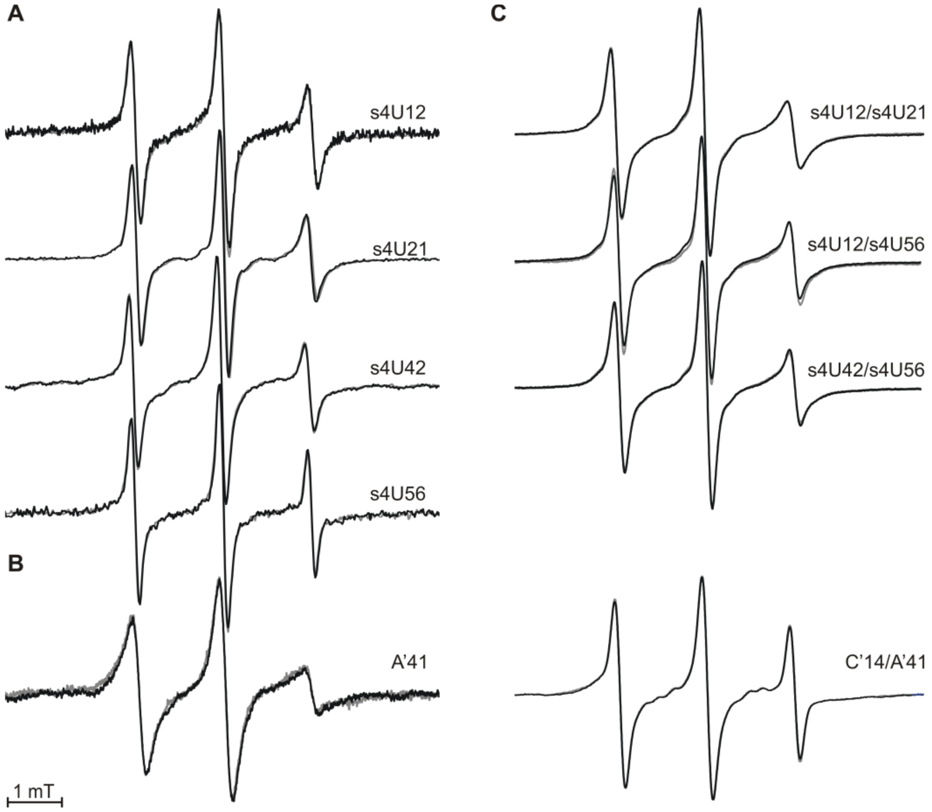

Figure 4.3 Room temperature continuous wave EPR spectra measured at X-band in the absence (black lines) and in the presence of Tc (grey lines). (A, C) Single and double mutants labeled with MTS and (B, D) single and double mutants labeled with the 4-isocyanato-TEMPO. All plots are normalized by amplitude.

Room temperature EPR spectra of s4U12, s4U56, and s4U12/s4U56 reveal only a single spectral component and the spectral shapes are not altered upon ligand binding. Hence, the observed distance distribution is attributed to an equilibrium of two aptamer conformations which characterize the free state of the aptamer. Addition of Tc traps the aptamer conformation corresponding to the larger interspin distance peak. For s4U42/s4U56 the distance distributions are almost identical in presence and absence of Tc with a mean distance of 4.8 *nm* (± 0.2 *nm*). A manual variation of the homogenous background correction shifts the mean distances by

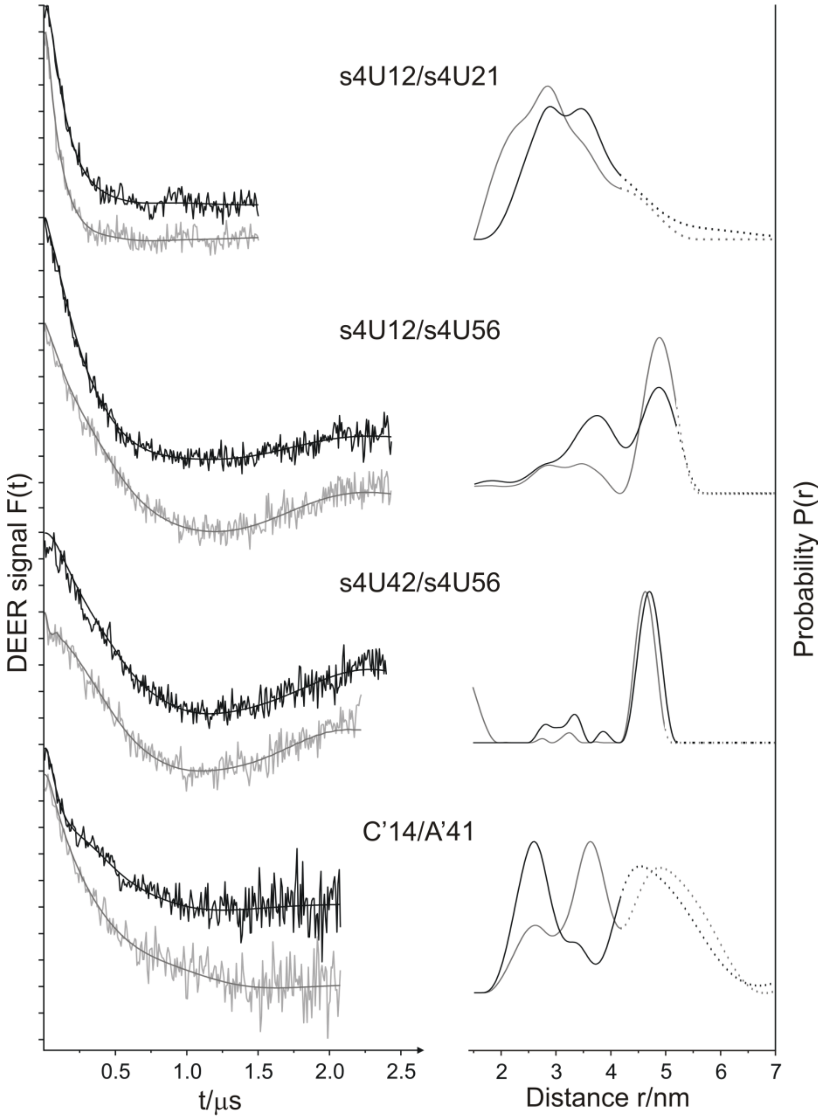

Figure 4.4 DEER analysis of the RNA double mutants s4U12/s4U21, s4U12/s4U56, s4U42/s4U56, and C'14/A'41 in the absence (black) and in the presence of Tc (grey). Left: background corrected dipolar evolution data F(t). Tick marks are separated by 0.02. Right: distance distributions P(r) obtained using DeerAnalysis2006[33]. In the dotted range intermolecular spin-spin interaction may contribute.

less than 0.4 *nm* for these mutants. The data for C'14/A'41 in the absence of Tc exhibits three major peaks centered at 2.6 *nm* (± 0.3 *nm*), 3.4 *nm* (± 0.2 *nm*) and 4.7 *nm* (± 0.7 *nm*). In the presence of Tc the population ratio of the peaks corresponding to 2.6 *nm* and 3.4 *nm* are interconverted. Variation of the homogenous background correction leads to a significant decrease of the population for distances larger than 4.5 *nm*. This is strong evidence that the peaks at 4.8 *nm* do not reflect dipolar interaction within the same RNA molecule but are due to the interaction with background spins or have to be attributed to the presence of a fraction of unfolded aptamers. In addition to the analysis by Tikhonov regularization, all data were fitted with a Monte Carlo/SIMPLEX algorithm assuming a sum of Gaussian-distributed conformers contributing to the dipolar evolution data by use of the software DEFit 3.9[34]. The resulting distance distributions resemble those obtained by Tikhonov regularization.

The location and the microenvironment of the introduced spin labels are schematically represented in the aptamer model depicted in Fig. 4.5. Regions J1-2, J2-3 and L3 of the model were built according to the X-ray structure of the circularly permuted tetracycline-dependent aptamer[20]. The model was complemented with a schematic representation of the stems P1 and P2 based on the chemical and enzymatic probing experiments[19] according to the experimental interspin distances. The experimentally determined interspin distances are indicated by grey dotted arrows in Figure 4.5, A. The two components in the distance distributions of s4U12/s4U21, s4U12/s4U56, and C'14/A'41 represent two locations of the nitroxides at positions 12 and 14 as indicated. The displacement of these nitroxides could not be achieved by reorientation of the nitroxide side chains but required adjusting of region J1-2 as represented in Fig. 4.5, B. Upon ligand binding one conformation (blue) is trapped which resembles that of the X-ray structure (3EGZ).

4.4 Discussion

The aim of this study was to investigate the dynamics and possible conformational changes of the Tc aptamer upon ligand binding. Therefore, different single and double spin labeled aptamer mutants were synthesized and analyzed by EPR spectroscopy. The results for the double mutants s4U12/s4U21, s4U12/s4U56 and C'14/A'41 indicate the presence of a thermodynamic equilibrium of two aptamer conformations characteristic for the free state of the aptamer. Ligand binding shifts this equilibrium towards one of these conformations. The spin label at site 21 is highly exposed without any restriction in its reorientational motion or ligand interaction according to the model illustrated in Fig. 4.5. In addition, the single component room temperature EPR spectra do not reveal any evidence for interaction with the ligand. Site 56 is located in stem P1, which is supposed to form the scaffold of the aptamer without direct ligand interaction. Since site 12 is located in the single stranded region J1-2, the distance changes observed for s4U12/s4U21 and s4U12/s4U56 indicate a displacement of this region upon Tc binding as displayed in Fig. 4.5. The results of s4U42/s4U56 reveal that s4U42 is not involved

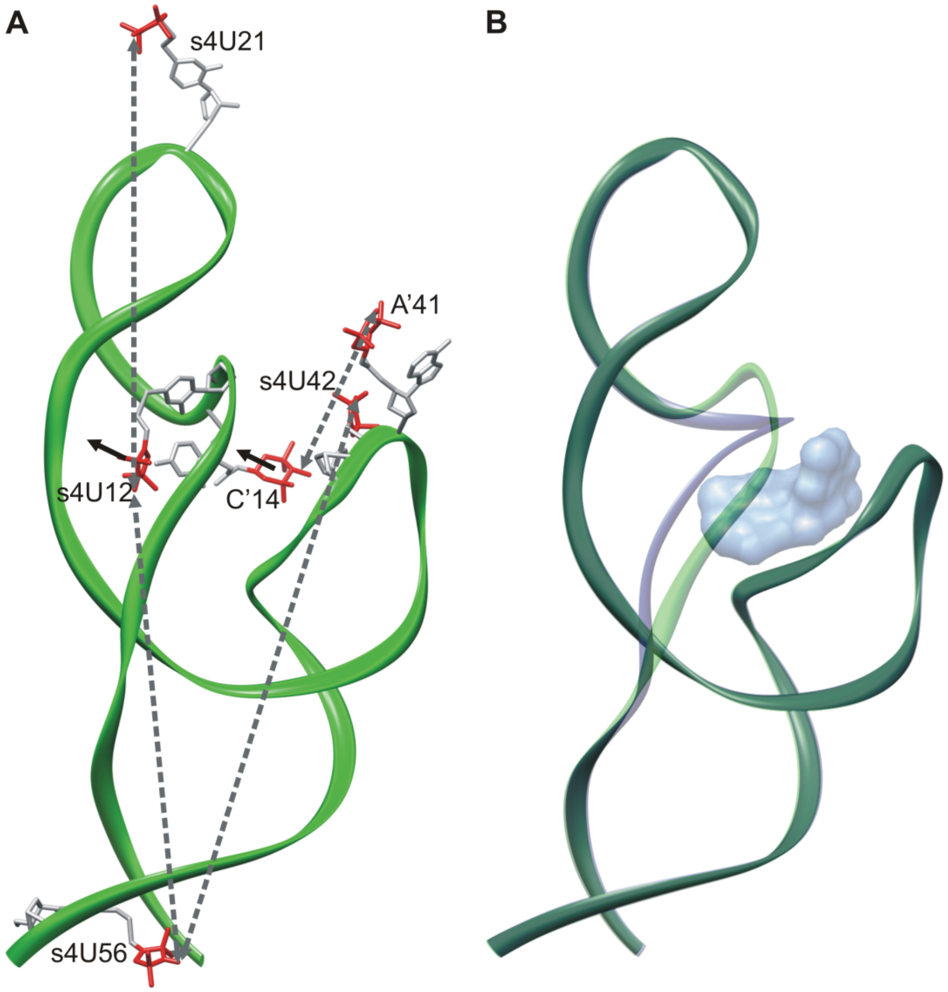

Figure 4.5 Schematic representations of the Tc aptamer conformations. The regions J1-2, J2-3 and L3 of the X-ray structure of the circularly permuted Tc-dependent aptamer[20] was complemented with a schematic representation of the stems P1 and P2 based on the chemical and enzymatic probing experiments[19]. (A) Interspin distances between nitroxides at positions 12, 14, 21, 41, 42, and 56 as indicated by grey dotted arrows were used as constraints during modeling. Black arrows indicate the displacement of the nitroxides at positions 12 and 14 upon addition of Tc. (B) Two aptamer conformations (green, blue) are in equilibrium in the free state. Upon addition of Tc (shown in surface representation) the aptamer conformation depicted in blue is trapped.

in conformational changes upon ligand binding; the distance distributions in presence and absence of Tc are identical. Hence, a ligand induced transformation of the opposing loop region along the stem region P1 is unlikely and a transformation of the stem regions of the aptamer could not be resolved. Therefore, the distance changes detected for C'14/A'41 again reveal the displacement of the single stranded region J1-2. In conclusion, addition of Tc leads to the capture of one aptamer conformation which resembles that of the X-ray structure[20].

Similar conformational changes have been revealed by NMR spectroscopy for a citrulline-binding RNA aptamer and the related arginine-binding aptamer[35]. Both aptamers contain two asymmetrical internal loops that are not well ordered in the free RNA but fold into a compact structure upon ligand binding with one nucleotide capping the binding pocket. Evidence for a dynamic equilibrium of an "inactive" and an "active" state was provided for a theophylline-binding RNA aptamer[36]. Their results indicated that the RNA utilize a conformational selection mechanism for binding theophylline like other RNAs with conformationally heterogeneous free states, such as the aptamer domains in RNA riboswitches binding their ligands. Furthermore, a previous NMR study on the aptamer domain of a guanine riboswitch[37] revealed that the aptamer domain binds the ligand in a disordered and unstructured binding pocket but with a preorganized tertiary interaction between two loops in its free state. The loop–loop interaction organizes the global fold of the RNA prior to ligand binding, only small changes are necessary to accommodate the ligand.

In this work we studied the conformational transition of a spin labeled Tc binding RNA aptamer using DEER spectroscopy in combination with site-directed spin labeling. We have focused on the determination of interspin distances of four double spin labeled aptamer variants which uncovers a thermodynamic equilibrium of two aptamer conformations in absence of Tc and the capture of one conformation in presence of Tc. Existence of a conformational equilibrium in the free state and shift to one conformation upon ligand binding seems to be a capable mechanism for a riboswitch to provide the necessary action to impact on gene expression.

4.5 Materials and Methods

Synthesis and spin labeling of RNA aptamers

The RNA variants were obtained by solid-phase RNA synthesis using standard phosphoramidite chemistry as described[38, 39]. 3'-*O*-phosphoramidites of *N*-acyl-5'-*O*-dimethoxytrityl-2'-*O*-tertbutyldimethylsilyl protected nucleosides were obtained from ChemGenes, Wilmington, MA. A set of different positions in the stems, single stranded region and loop region was selected for post-synthetically spin labeling (Fig. 4.1; highlighted in grey) with either the (1-oxyl-2,2,5,5-tetramethylpyrroline-3-methyl)methanethiosulfonate (MTS) spin label or the 4-isocyanato-2,6-tetramethylpiperidyl-N-oxid (4-isocyanato-TEMPO) spin label (Fig. 4.2).

The modified nucleotide 4-thiouridine was incorporated at pre-selected positions instead of uridine to be used for post-synthetic spin labeling with MTS[40]. RNA samples were incubated for 2 *h* at room temperature (RT) with a 200-fold excess of dithiothreitol (DTT) in 50 *µl* of 100 *mM* sodium phosphate buffer (pH 8.0). The reducing agent was removed by demineralization using centrifugal filters, followed by lyophilization of the RNA. Spin labeling was carried out overnight by incubation of a 100 *µM* solution of the RNA double mutant in 90 *mM* sodium phosphate buffer (90 % v/v) (pH 8.0) and dimethylformamide (DMF) (10 % v/v) with a 10-fold excess of MTS. Unbound MTS was removed by demineralization and lyophilization as described above. Different singly and doubly spin labeled RNAs (named according to the spin labeled sites) were synthesized, namely single mutants s4U12, s4U21, s4U42 and s4U56, and double mutants s4U12/s4U21, s4U12/s4U56 and s4U42/s4U56.

Alternatively, 4-isocyanato-TEMPO was attached to the sugar moiety of the specific nucleotides. Therefore, RNA mutants were synthesized with 2'-aminouridine and subsequently spin labeled[41, 42]. A 100 *µM* solution of the RNA in 100 *mM* sodium borate buffer (pH 8.5) (50 % v/v), DMF (20 % v/v) and formamide (30 % v/v) was cooled down to -8 °C and incubated for 2 *h* with a 15-fold excess of TEMPO. Side products and unbound reagents were extracted with 300 *µl* chloroform at RT followed by precipitation of the labeled RNA from ethanol, resolving the pellet in water, demineralization using centrifugal filters and finally lyophilization of the RNA. Again, labeled RNAs are named according to the spin labeled sites, namely C’14 for the single mutant and C’14/A’41 for the double mutant. For both spin label strategies the spin label efficiency was approximately above 50 %.

Fluorescence titration experiments

Fluorescence titration experiments were carried out at 25 °C on a Fluorolog FL3-22. The excitation wavelength was set to 370 *nm*. Spectra were acquired from 450 to 600 *nm* in 1 *nm* increments with an integration time of 0.3 *sec*. Slits were set to 2 *mm*. Tc was presented in a total volume of 2 ml binding buffer (20 mM potassium phosphate buffer pH 7.5, 100 *mM* NaCl, 1 *mM* $MgCl_2$). The RNA was dissolved in binding buffer and titrated avoiding a total volume increase of more than 5 %. The solution was stirred during each titration step and allowed to equilibrate for 2 *min* before data collection. Fluorescence spectra were measured for each titration point. The peak area of the fluorescence emission signal was averaged, normalized and plotted against the free RNA concentration. The dissociation constant K_D was calculated as described earlier[18].

EPR sample preparation

The RNA was dissolved (50-70 μM final concentration for single mutants or 110 -150 μM for double mutants) in 20 mM potassium phosphate buffer, 100 mM NaCl, 5 mM $MgCl_2$ (pH 7.5). 5-20 % glycerol (v/v) was added as a cryoprotectant and deuterated water was used to increase the transverse relaxation time for pulse EPR experiments. The RNA mutants were incubated at 45 °C for 5 min followed by slow-cooling to RT in order to allow homogeneous tertiary structure formation. Complex formation with a 2-fold excess of Tc was assured by an additional incubation for 5 min at 37 °C and slow-cooling to RT.

For the DEER experiments 30-40 μl of the sample solution was filled into EPR quartz capillaries and frozen in liquid nitrogen before insertion into the resonator. Sample volumes of 10 μl were loaded into EPR quartz capillaries for continuous wave (*cw*) EPR measurements.

EPR setup

Room temperature *cw* EPR spectra at X-band were recorded using a Magnettech Miniscope MS200 X-band spectrometer equipped with a rectangular TE102 resonator. To avoid saturation and to obtain high signal-to-noise ratio the microwave power was set to 10 mW and the B-field modulation amplitude was adjusted to 0.15 mT.

All DEER experiments were performed at 50 K using a Bruker Elexsys 580 spectrometer equipped with a 3-mm split ring resonator (ER 4118X-MS3; Bruker) at X-band frequencies (9.4 GHz). The resonator was overcoupled to Q ~ 100. Temperature stabilization was achieved by a continuous flow helium cryostat (ESR 900; Oxford Instruments) in combination with a temperature controller (ITC 503S; Oxford Instruments). The following four-pulse DEER sequence was used[43]:

$$\frac{\pi}{2}(\nu_{obs}) - \tau_1 - \pi(\nu_{obs}) - t - \pi(\nu_{pump}) - (\tau_1 + \tau_2 - t) - \pi(\nu_{obs}) - \tau_2 - echo. \tag{4.1}$$

For all pulses at the observer frequency the ‹x› channels were applied. A two-step phase cycling (+ ‹x›, - ‹x›) was performed on $\frac{\pi}{2}(\upsilon_{obs})$. The observer pulses had lengths of 16 ns for $\frac{\pi}{2}$ and 32 ns for π pulses and the pump pulse length was set to 12 ns. The pump frequency, υ_{pump}, was positioned at the center of the resonator dip. This frequency corresponded to the maximum of the echo-detected nitroxide EPR absorption spectrum. The observer frequency, υ_{obs} , was set to the low field local maximum of the absorption spectrum which resulted in a 65 MHz frequency offset. Time τ_1 and τ_2 were kept constant, whereas t' was varied. Deuterium modulation was averaged by addition of traces at eight different τ_1 start values, starting at $\tau_{1,0}$ = 400 *ns* and incrementing by $\Delta\tau_1$ = 56 *ns*. The dipolar evolution time was given by $t = t' - \tau_1$ and data with $t > 0$ were analyzed. The experimental echo decay was background-corrected using a homogeneous three-dimensional spin distribution. The experimental DEER spectra yield information about intra- and intermolecular interspin distances. A background correction separates the intermolecular background contribution from the intramolecular contribution. Interspin distance distributions were derived by fitting the dipolar evolution function using Tikhonov regularization, a commonly used method of regularization of ill-posed problems, as implemented in DEERAnalysis2006[33]. In addition, the experimental data were fitted with a Monte Carlo/SIMPLEX algorithm assuming a sum of Gaussian-distributed interspin distances contributing to the dipolar evolution data by use of the software DEFit 3.9[34].

Molecular modeling

The starting structure for molecular modeling was the X-ray structure of the circularly permuted tetracycline aptamer[20] (Protein Data Bank code: 3EGZ). The regions J1-2, J2-3 and loop L3 were extracted and complemented with the stems P1 and P2. Both stems were constructed according to the chemical and enzymatic probing experiments[19]. Spin label were introduced at the positions 12, 14, 21, 41, 42 and 56, the topologies for the spin label side chains were set up with respect to published data[44] and similar configurations in the Gromacs library. The initial molecular model was adapted on the bases of the experimentally determined interspin distances, resulting in two molecular models which correspond to the two aptamer conformations in the free state. For both molecular models energies were minimized by means of steepest descent using the amber99[45] force field implemented in the Gromacs simulation package[46]. Periodic boundary conditions in the presence of TIP3P water molecules were utilized.

4.7 References

[1] A. Roth, R. R. Breaker. *Annu. Rev. Biochem.* **2009**, *78*, 305-334.

[2] L. Gold, B. Polisky, O. Uhlenbeck, M. Yarus. *Annu. Rev. Biochem.* **1995**, *64*, 763-797.

[3] D. S. Wilson, J. W. Szostak. *Annu. Rev. Biochem.* **1999**, *68*, 611-647.

[4] M. Famulok, J. S. Hartig, G. Mayer. *Chem. Rev.* **2007**, *107*, 3715-3743.

[5] J. E. Weigand, B. Suess. *Applied Microbiology and Biotechnology* **2009**, *85*(2), 229-236.

[6] B. Suess, J. E. Weigand. *Rna Biology* **2008**, *5*(1), 24-29.

[7] M. N. Win, J. C. Liang, C. D. Smolke. *Chem. & Biol.* **2009**, *16*(3), 298-310.

[8] A. D. Ellington, J. W. Szostak. *Nature* **1990**, *346*(6287), 818-822.

[9] C. Tuerk, L. Gold. *Science* **1990**, *249*(4968), 505-510.

[10] M. Famulok. *Curr. Opin. Struc. Biol.* **1999**, *9*(3), 324-329.

[11] D. J. Patel, A. K. Suri. *J Biotechnol* **2000**, *74*(1).

[12] T. Hermann, D. J. Patel. *Science* **2000**, *287*(5454), 820-825.

[13] B. Suess, S. Hanson, C. Berens, B. Fink, R. Schroeder, W. Hillen. *Nucl. Acids. Res.* **2003**, *31*(7), 1853-1858.

[14] P. Kotter, J. E. Weigand, B. Meyer, K. D. Entian, B. Suess. *Nucl. Acids. Res.* **2009**, *37*(18).

[15] J. E. Weigand, B. Suess. *Nucl. Acids. Res.* **2007**, *35*(12), 4179-4185.

[16] B. Epe, P. Woolley, H. Hornig. *FEBS Letters* **1987**, *213*(2), 443-447.

[17] C. Berens, W. Hillen. *Eur J Biochem* **2003**, *270*(15), 3109-3121.

[18] M. Mueller, J. E. Weigand, O. Weichenrieder, B. b. b. d. Suess. *Nucl. Acids. Res.* **2006**, *34*(9), 2607-2617.

[19] S. Hanson, G. Bauer, B. Fink, B. Suess. *Rna-A Publication of the Rna Society* **2005**, *11*(4), 503-511.

[20] H. Xiao, T. E. Edwards, A. R. Ferre-D'Amare. *Chem. & Biol.* **2008**, *15*(10), 1125-1137.

[21] M. Lorenz, S. Diekmann. *Methods in Molecular Biology* **2006**, 243-255.

[22] H. D. Kim, G. U. Nienhaus, T. Ha, J. W. Orr, J. R. Williamson, S. Chu. *Proceedings of the National Academy of Sciences of the United States of America* **2002**, *99*(7), 4284-4289.

[23] M. Margittai, J. Widengren, E. Schweinberger, G. F. Schroder, S. Felekyan, E. Haustein, M. Konig, D. Fasshauer, H. Grubmuller, R. Jahn, C. A. M. Seidel. *Proceedings of the National Academy of Sciences of the United States of America* **2003**, *100*(26), 15516-15521.

[24] W. L. Hubbell, D. S. Cafiso, C. Altenbach. *Nat. Struct. Biol.* **2000**, *7*(9), 735-739.

[25] Q. Cai, A. K. Kusnetzow, W. L. Hubbell, I. S. Haworth, G. P. Gacho, N. Van Eps, K. Hideg, E. J. Chambers, P. Z. Qin. *Nucl. Acids. Res.* **2006**, *34*(17), 4722-4730.

[26] E. Bordignon, H.-J. Steinhoff. Membrane protein structure and dynamics studied by site-directed spin labeling ESR, In: (Eds.: M. A. Hemminga and L. J. Berliner), *Biological Magnetic Resonance 27 - ESR Spectroscopy in Membrane Biophysics,* New York, Springer Science and Business Media, **2007**, pp. 129-164.

[27] O. Schiemann, N. Piton, Y. Mu, G. Stock, J. W. Engels, T. F. Prisner. *J. Am. Chem. Soc.* **2004**, *126*(18), 5722-5729.

[28] N. Piton, O. Schiemann, Y. Mu, G. Stock, T. Prisner, J. W. Engels. *Nucleosides, Nucleotides and Nucleic Acids* **2005**, *24*(5), 771-775.

[29] O. Schiemann, A. Weber, T. E. Edwards, T. F. Prisner, S. T. Sigurdsson. *J. Am. Chem. Soc.* **2003**, *125*(12), 3434-3435.

[30] G. Sicoli, G. Mathis, O. Delalande, Y. Boulard, D. Gasparutto, S. Gambarelli. *Angewandte Chemie-International Edition* **2008**, *47*(4), 735-737.

[31] G. Sicoli, G. Mathis, S. Aci-Seche, C. Saint-Pierre, Y. Boulard, D. Gasparutto, S. Gambarelli. *Nucleic Acids Res.* **2009**, *37*(10), 3165-3176.

[32] G. Jeschke, Y. Polyhach. *Physical Chemistry Chemical Physics* **2007**, *9*(16), 1895-1910.

[33] G. Jeschke, V. Chechik, P. Ionita, A. Godt, H. Zimmermann, J. E. Banham, C. R. Timmel, D. Hilger, H. Jung. *Appl. Magn. Reson.* **2006**, *30*(3-4), 473-498.

[34] K. I. Sen, T. M. Logan, P. G. Fajer. *Biochemistry* **2007**, *46*(41), 11639-11649.

[35] Y. S. Yang, M. Kochoyan, P. Burgstaller, E. Westhof, M. Famulok. *Science* **1996**, *272*(5266), 1343-1347.

[36] M. P. Latham, G. R. Zimmermann, A. Pardi. *J. Am. Chem. Soc.* **2009**, *131*(14), 5052-+.

[37] J. Noeske, J. Buck, B. Fürtig, H. R. Nasiri, H. Schwalbe, J. Wähnert. *Nucl. Acids. Res.* **2007**, *35*(2), 572-583.

[38] R. Welz, S. Muller. *Tetrahedron Lett.* **2002**, *43*(5), 795-797.

[39] C. Schmidt, R. Welz, S. Muller. *Nucl. Acids. Res.* **2000**, *28*(4), 886-894.

[40] P. Z. Qin, K. Hideg, J. Feigon, W. L. Hubbell. *Biochemistry* **2003**, *42*(22), 6772-6783.

[41] T. E. Edwards, T. M. Okonogi, B. H. Robinson, S. T. Sigurdsson. *J. Am. Chem. Soc.* **2001**, *123*(7), 1527-1528.

[42] N.-K. Kim, A. Murali, V. J. DeRose. *Chem. & Biol.* **2004**, *11*, 939-948.

[43] M. Pannier, S. Veit, A. Godt, G. Jeschke, H. W. Spiess. *J. Magn. Res.* **2000**, *142*(2), 331-340.

[44] C. Beier, H.-J. Steinhoff. *Biophys. J.* **2006**, *91*(7), 2647-2664.

[45] E. J. Sorin, V. S. Pande. *Biophys. J.* **2005**, *88*(4), 2472-2493.

[46] D. van der Spoel, E. Lindahl, B. Hess, G. Groenhof, A. E. Mark, H. J. C. Berendsen. *Journal of Computational Chemistry* **2005**, *26*(16), 1701-1718.

5

Molecular modeling and molecular dynamics (MD) study of a synthetic tetracycline aptamer

5.1 Introduction

In the last decade molecular dynamics (MD) simulations have become an established and powerful tool in the study of biomolecules. Complementary to experimental techniques like EPR spectroscopy it enhances the understanding of the structure and function of biomolecules and the interpretation of experimental results. While particularly EPR spectroscopy provides local information about the dynamic of the spin label nitroxides, their immediate environment and intramolecular distances between two spin labels, MD simulations give insight into the dynamics of the entire biomolecule and inter-atom distances as a function of time. MD simulations have been successfully applied to systems involving protein-RNA binding[1] and the study of structures and dynamics of small RNA systems[2-4]. A well established and widely used force field for nucleic acids in MD simulations is AMBER[5-7]. In a previous study, *cw* and pulse EPR spectroscopy combined with site directed spin labeling were used to elucidate the dynamics and the conformational transition of a synthetic tetracycline (Tc) riboswitch upon ligand binding[8]. This well characterized aptamer acts as an RNA switch for conditional gene expression in yeast, either inhibiting translation initiation[9] or pre-mRNA splicing[10]. The experimental results indicate the presence of a thermodynamic equilibrium between two aptamer conformations in the free state and the capture of one conformation upon Tc binding[8]. The combination of experimentally determined interspin distances and previously published structural information of the aptamer binding pocket[11] results in molecular models of the Tc aptamer. Two molecular models were built corresponding to the equilibrium aptamer conformations in the free state. In addition, a molecular model was created corresponding to the conformation in the presence of Tc.

In the present chapter, MD simulations performed on these aptamer models in the absence and in the presence of Tc are discussed and compared to experimental results. The simulated interspin distances distributions are found to be in good agreement with the experimental determined interspin distance distributions. Together with the proven stability of all three aptamer structures during the MD simulations, these models are thought to represent reasonable aptamer conformations in thermodynamic equilibrium in the absence of Tc and upon ligand addition.

5.2 Materials and Methods

Molecular Modeling

For molecular modeling of all aptamer models the X-ray structure of the circularly permuted tetracycline-dependent aptamer[11] (Protein Data Bank code: 3EGZ, Fig. 5.1) was used as a starting point.

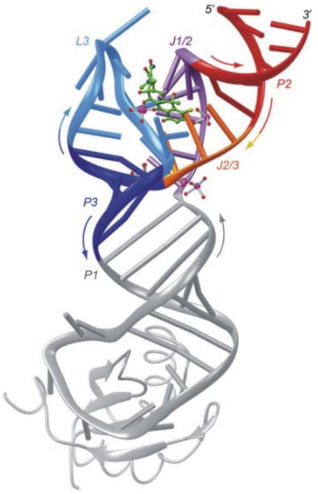

Figure 5.1 Schematic representation of the Tc aptamer in complex with 7-chlorotetracycline (green stick figure) and U1A. Magnesium ions and their solvation waters (magenta and red spheres, respectively) are shown. Colored arrows denote chain direction (Figure adopted from [11]).

The sequence of this permuted Tc aptamer, shown in Fig. 5.2, differs from that of the Tc-dependent aptamer used in this work. The residue numbers of the Tc-dependent aptamer correspond to those of Hanson *et al.*[12] (Fig. 5.2, A) and the residues numbers of the permuted Tc aptamer to those of Xiao *et al.*[11] (Fig. 5.2, B). In the permuted Tc aptamer loop L2 was deleted and a U1A protein binding site (L4) was introduced which caps stem P1. The regions J1-2, J2-3 and L3, involved in ligand binding, are identical in both constructs. Hence, the regions J1-2, J2-3 and L3 of the circularly permuted tetracycline-dependent aptamer were extracted for the adjacent molecular modeling. In addition, stems P1 and P2 are built separately according to the known sequence (Fig. 5.2, A) and the chemical and enzymatic probing experiments[12]. Spin labels were introduced at the positions 12, 14, 21, 41, 42 and 56. The respective components were merged on the bases of experimentally determined interspin distances leading to an initial molecular model of the aptamer. The initial molecular model was energy minimized by means of steepest descent using the amber99[13] force field implemented in the Gromacs simulation package[14]. The topologies for the spin label side chains were set up with respect to published data[15] and similar configurations in the Gromacs library. Periodic boundary conditions in the presence of TIP3P water molecules were utilized. The initial molecular model was further optimized according to the experimentally determined interspin distances for RNA double mutants s4U12/s4U21, s4U12/s4U56, s4U42/s4U56 and C’14/A’41 (see chapter 4), resulting in two molecular models which correspond to the two equilibrium aptamer conformations and in one molecular model related to the aptamer conformation in the presence of Tc. The interspin distance for RNA double mutant s4U12/s4U42 determined by *cw* EPR spectroscopy is disregarded during the process of molecular modeling and serves as a closing verification of the molecular models. Molecular dynamics (MD) simulation were performed on these three aptamer models.

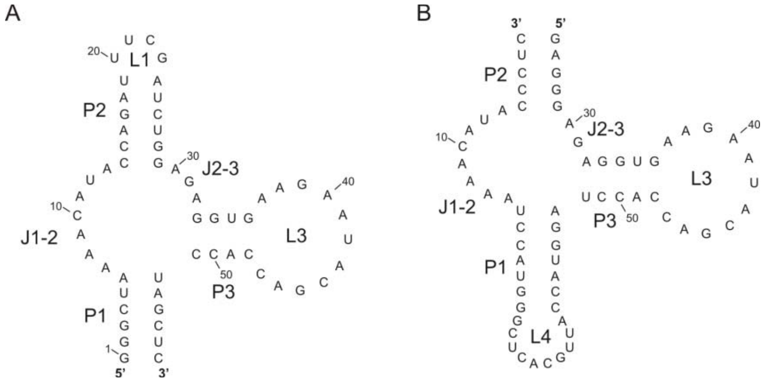

Figure 5.2 Secondary structure of the Tc aptamer (A) and the circularly permuted Tc aptamer[11] (B). Residue numbers correspond to those of Hanson *et al*. [12] (A) and Xiao *et al*.[12] (B).

Molecular Dynamics simulation

Molecular dynamics (MD) simulations were performed using YASARA Dynamics[16] with periodic cell boundaries and the implemented amber99 force field[13]. For all simulations a simulation cell with 15 *Å* space around the respective aptamer model was created. The simulation cells were filled with explicit water molecules and Na^+/Cl^- counter ions at locations of the lowest/highest electrostatic potential during a cell neutralization and pK_a prediction experiment (pH 7.0). To remove bumps and correct the covalent geometry, the structure was energy-minimized, using a 7.8 *Å* force cutoff and the Particle Mesh Ewald (PME) algorithm to treat longrange electrostatic interactions. The topologies for the spin label side chains and for the tetracycline were set up by YASARA Dynamics. After removal of conformational stress by a steepest descent minimization, the procedure continued by simulated annealing (time step 2 *fs*, atom velocities scaled down by 0.9 every 10th step) until convergence was reached and the energy improved by less than 0.05 kJ/mol per atom during 200 steps. Afterwards, the final 10 *ns* MD simulations were done at 298 *K* with 1 *fs* time steps under constant pressure, while intermolecular forces were calculated every 2 *fs* and the first 0.3 *fs* were not considered during analysis. Periodic boundary crossing of solute atoms was prevented by means of the function "solute drift". The interspin distances were extracted using the macro "MD analyzes" provided by YASARA Dynamics.

5.3 Results and Discussion

In order verify the suggested conformation of the three previously discussed aptamer models[8] and to analyze the effects on the overall structure induced by spin labeling MD simulations were performed (for the starting structures see Fig. 4.5). The two equilibrium aptamer models are based on the circularly permuted Tc riboswitch[11] and on experimental determined interspin distances in the absence of Tc. The aptamer model in the presence of the ligand is based on the equilibrium aptamer structure in the absence of Tc.

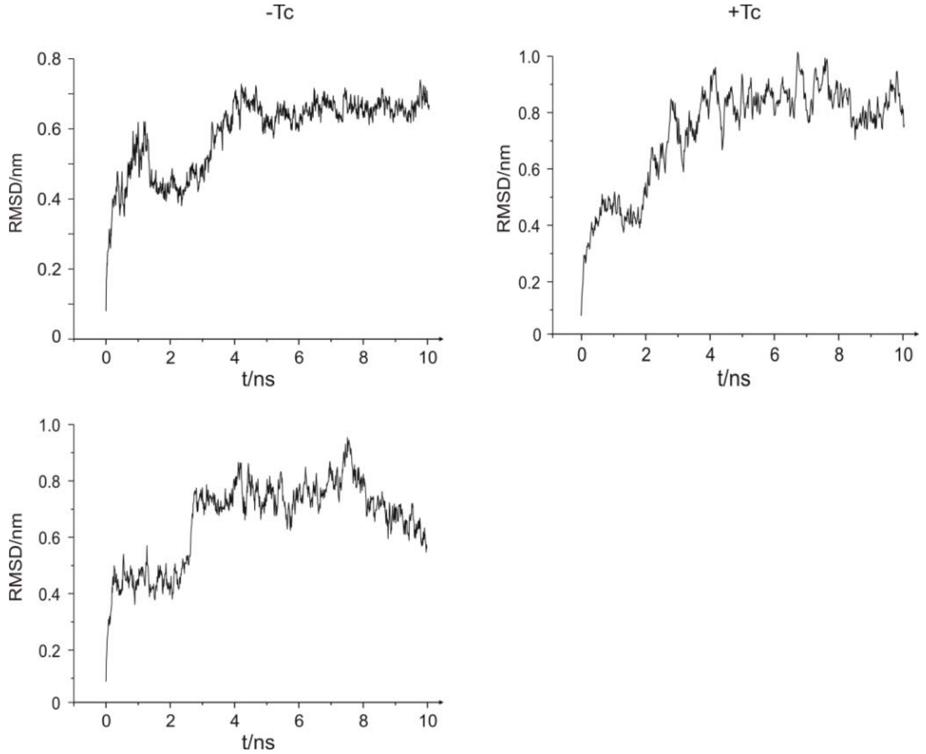

Figure 5.3 Root mean square deviations (RMSD) from the respective initial starting structures for both equilibrium aptamer models in the absence of Tc (left side) and the aptamer model related to the captured conformation in the presence of Tc (right side).

During the 10 *ns* MD simulations the overall structures remain stable, even though all three aptamer models display a high flexibility (cf. Fig. 5.3). In particular, the stem region P1 (cf. Fig. 4.1 and chapter 4.2 for details) exhibits a high flexibility and the possibility to perform movements centered at the pseudoknot of the aptamer structure without altering the overall length of the stem. The steep rise of the respective RMSD (cf. Fig. 5.3) at the beginning of the simulation is caused by the adaption of the models to the force field and has to be accounted for in the adjacent analysis.

	MD		EPR spectroscopy	
	without Tc	with Tc	without Tc	with Tc
s4U12/s4U21	2.6 ± 0.2 3.4 ± 0.7	3.1 ± 0.6	2.9 ± 0.5 3.8 ± 0.4	(2.3 ± 0.4) 2.8 ± 0.5 (3.8 ± 0.5)
s4U12/s4U42	(1.2 ± 0.2) (1.5 ± 0.2) 1.8 ± 0.2 2.0 ± 0.3	1.8 ± 0.4	1.4 ± 0.2	1.4 ± 0.2
s4U12/s4U56	3.7 ± 0.3 4.6 ± 0.4	4.8 ± 0.4	3.8 ± 0.4 5.0 ± 0.5	4.9 ± 0.2
s4U42/s4U56	4.3 ± 1.0 4.8 ± 0.5	4.7 ± 0.5	4.8 ± 0.2	4.7 ± 0.2
C’14/A’41	2.2 ± 0.1 2.8 ± 0.2	3.2 ± 0.1	2.6 ± 0.3 (3.4 ± 0.2)	(2.7 ± 0.4) 3.6 ± 0.3

Table 5.1 Experimental and simulated interspin distances for double labeled RNA mutants. Dominating interspin distance peaks are given with their estimated FWHM widths, peaks with decreased probability or shoulders are shown in parenthesis.

The simulated mean interspin distances and distribution widths are compared to the experimental dominating interspin distance peaks and their estimated distribution widths (see Table 5.1). The simulated interspin distance distributions for the equilibrium aptamer models in the absence of Tc, the simulated interspin distance distributions in the presence of Tc and the respective experimental ones are overlaid in Fig. 5.4. For s4U12/s4U21 in the absence of Tc the simulated mean interspin distances are centered at 2.6 *nm* (± 0.2 *nm*) and 3.4 *nm* (± 0.7 *nm*), and in presence of Tc at 3.1 *nm* (± 0.6 *nm*). Comparison of simulated and experimental distance distributions in absence of Tc reveal a slight shift of the mean interspin distances to shorter and longer distances. The superposition of both simulated interspin distances and their distribution widths coincides with the experimental distance distribution. In addition, the experimental mean interspin distance as well as the distribution width in presence of Tc are satisfactorily reproduced. The missing shoulder towards shorter distances in the presence of the ligand may arise from the existence of the second equilibrium aptamer conformation which does not

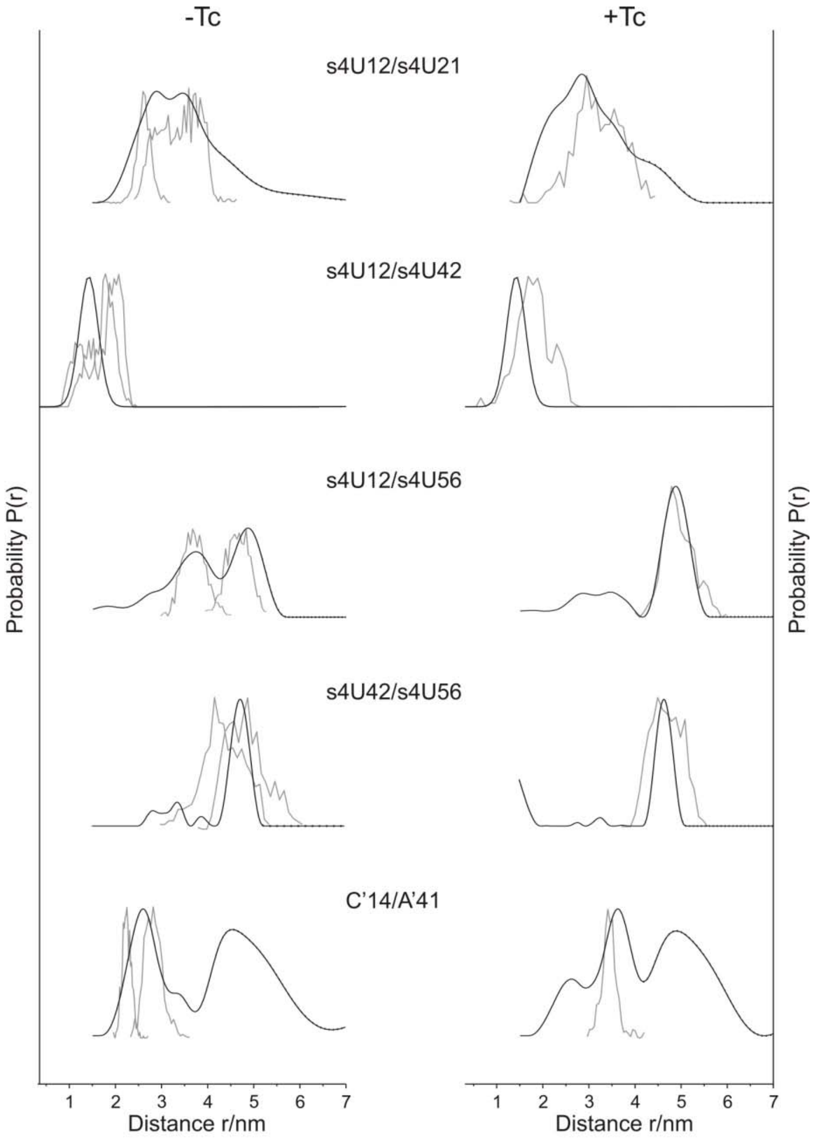

Figure 5.4 Comparison of experimental and simulated interspin distance distributions for RNA double mutants s4U12/s4U21, s4U12/s4U56, s4U42/s4U56, and C'14/A'41. Experimental distance distributions (black) are obtained by pulse EPR spectroscopy in absence (left) or presence of Tc (right), respectively and simulated distance distributions (grey) by MD simulations. In the dotted range intermolecular spin-spin interactions may contribute due to different sample preparation (for details see chapter 4.3).

bind Tc. For s4U12/s4U42 the simulated mean interspin distances are in the range of 1.2-2.0 *nm* in the absence of Tc. In the presence of Tc the mean interspin distance is positioned at 1.8 *nm* (± 0.4 *nm*). Due to the fact that the fitting of the dipolar broadened *cw* EPR spectra only reveal interspin distances below 1.8 *nm*, the simulated interspin distance distributions are in good agreement with the experimental ones, even though the interspin distance for s4U12/s4U42 was not considered during molecular modeling as a restraint. For s4U12/s4U56 the simulated mean interspin distances in the absence of Tc of 3.7 *nm* (± 0.3 *nm*) and 4.6 *nm* (± 0.4 *nm*), and 4.8 *nm* (± 0.4 *nm*) in the presence of Tc are evident. The experimental distance distribution reveals two major peaks in absence of Tc which are adequately reproduced by the simulated distance distribution in terms of the mean interspin distances and the distribution widths. Furthermore, the agreement between the simulated and experimental interspin distance distributions is excellent in presence of Tc for the interspin distance as wells as the width. For s4U42/s4U56 in the absence of Tc, the simulated mean interspin distances are positioned at 4.3 *nm* (± 1.0 *nm*) and 4.8 *nm* (± 0.5 *nm*). In the presence of Tc a major distance peak at 4.7 *nm* (± 0.5 *nm*) is observed. Even though there is a reasonable agreement between the experimental and the simulated mean interspin distances in the absence of Tc for one aptamer model, there is no agreement for the other equilibrium aptamer model. In both cases, it is obvious that the simulated distribution width is broader than the experimentally obtained one. This may be due to possible movements of the stem region P1 centered at the pseudoknot of the aptamer structure during the simulations and furthermore, the freezing process may stabilize the experimental structure. Since site s4U12 is located close to the pseudoknot, the double mutant s4U12/s4U56 is not able to detect a possible movement of stem P1 as long as the overall length and therefore the distance between sites 12 and 56 remains stable. The same characteristics are evident for the comparison of the simulated and the experimental distance distributions in the presence of Tc. Whereas the mean experimental interspin distance is satisfactorily reproduced, a broader simulated distribution width is apparent. For C’14/A’41 the simulated mean interspin distances are centered at 2.7 (± 0.1 *nm*) and 2.8 *nm* (± 0.2 *nm*) in the absence of Tc, and in the presence of Tc at 3.2 *nm* (± 0.1 *nm*). The simulated mean interspin distances are shifted towards shorter and longer distances compared to the experimental one in the absence of Tc. Considering the broader experimental distribution width both simulated distance distributions contribute to the experimental distance distribution. In the presence of Tc the simulated interspin distance is marginal shifted towards shorter distances and exhibits a considerable smaller distribution width than the experimental distribution width. These effects as well as the missing peak around 5 *nm* of the experimental distribution can be understood in terms of a considerable contribution of unfolded aptamers in the DEER experiments as discussed in chapter 4.3, and the minor peak towards shorter distances of the existence of the second equilibrium aptamer conformation which does not bind Tc.

In conclusion, the simulated interspin distance distributions are in good agreement with the experimental ones. Furthermore, the MD simulations exhibit a stable overall structure for all three aptamer models during the MD simulations. Consequently, all three aptamer models are appropriate candidates for the aptamer conformations in thermal equilibrium in the absence and for the captured conformation in the presence of Tc. Furthermore, the investigation of additional double mutants will enhance the accuracy of the aptamer models.

5.4 References

[1] Y. Zhao, B. L. Kormos, D. L. Beveridge, A. M. Baranger. *Biopolymers* **2006**, *81*(4), 256-269.

[2] A. Villa, G. Stock. *Journal of Chemical Theory and Computation* **2006**, *2*(5), 1228-1236.

[3] J. Koplin, Y. G. Mu, C. Richter, H. Schwalbe, G. Stock. *Structure* **2005**, *13*(9), 1255-1267.

[4] Widjajakusuma, Elisabeth C.,Fachbereich Biochemie, Universität Frankfurt a.M. **2007**.

[5] D. A. Case, D. A. Pearlman, J. W. Caldwell, T. E. Cheatham III, W. S. Ross, C. Simmerling, T. Darden, K. M. Merz, R. V. Stanton, A. Cheng, J. J. Vincent, M. Crwoley, V. Tsui, R. Radmer, Y. Duan, J. Pitera, I. Massova, G. L. Seibel, U. C. Singh, P. Weiner, P. A. Kollman. *AMBER - Version 6,* **1999**, p. -422.

[6] W. D. Cornell, P. Cieplak, C. I. Bayly, I. R. Gould, K. M. Merz, D. M. Ferguson, D. C. Spellmeyer, T. Fox, J. W. Caldwell, P. A. Kollman. *J. Am. Chem. Soc.* **1995**, *117*(19), 5179-5197.

[7] S. J. Weiner, P. A. Kollman, D. A. Case, U. C. Singh, C. Ghio, G. Alagona, S. Profeta, P. Weiner. *J. Am. Chem. Soc.* **1984**, *106*(3), 765-784.

[8] D. Wunnicke, D. Strohbach, J. E. Weigand, B. Appel, E. Feresin, B. Suess, S. Müller, H. J. Steinhoff. *RNA* **2011**, *17*(1), 182-188.

[9] B. Suess, S. Hanson, C. Berens, B. Fink, R. Schroeder, W. Hillen. *Nucl. Acids. Res.* **2003**, *31*(7), 1853-1858.

[10] J. E. Weigand, B. Suess. *Nucl. Acids. Res.* **2007**, *35*(12), 4179-4185.

[11] H. Xiao, T. E. Edwards, A. R. Ferre-D'Amare. *Chem. & Biol.* **2008**, *15*(10), 1125-1137.

[12] S. Hanson, G. Bauer, B. Fink, B. Suess. *RNA* **2005**, *11*(4), 503-511.

[13] E. J. Sorin, V. S. Pande. *Biophys. J.* **2005**, *88*(4), 2472-2493.

[14] D. van der Spoel, E. Lindahl, B. Hess, G. Groenhof, A. E. Mark, H. J. C. Berendsen. *Journal of Computational Chemistry* **2005**, *26*(16), 1701-1718.

[15] C. Beier, H.-J. Steinhoff. *Biophys. J.* **2006**, *91*(7), 2647-2664.

[16] E. Krieger, T. Darden, S. B. Nabuurs, A. Finkelstein, G. Vriend. *Proteins-Structure Function and Bioinformatics* **2004**, *57*(4), 678-683.

6

Site-directed Spin Labeling of DNA by the Azide-Alkyne 'Click' Reaction: Nanometer Distance Measurements on 7-Deaza-2′-deoxyadenosine and 2′-Deoxyuridine Nitroxide Conjugates Spatially Separated or Linked to a 'dA-dT' Base Pair

Ding P, Wunnicke D, Steinhoff HJ, Seela F (2010) *Chemistry - A European Journal* **16**:14385-14396.

6.1 Abstract

Nucleobase-directed spin labeling by the azide-alkyne 'click' (CuAAC) reaction was performed for the first time on oligonucleotides. 7-Deaza-7-ethynyl-2'-deoxyadenosine (**1**) and 5-ethynyl-2'-deoxyuridine (**2**) were chosen to incorporate terminal triple bonds into DNA. Oligonucleotides containing **1** or **2** were synthesized on solid-phase, and spin labeling with 4-azido-2,2,6,6-tetramethyl-piperidine-1-oxyl (4-azido TEMPO, **3**) was performed by post-modification in solution. Two spin labels (**3**) were incorporated with high efficacy in the DNA duplex at spatially separated positions or in a 'dA-dT' base pair. Modification at the 5-position of the pyrimidine base or the 7-position of the 7-deazapurine residue give steric freedom to the spin label in the major groove of duplex DNA. By applying *cw* and pulse EPR spectroscopy, very accurate distances within a 1-2 *nm* range were measured. The spin spin distance was 1.8 *nm* (± 0.2 *nm*) for DNA duplex **17(dA$^{*7,\ 10}$)•11** containing two spin labels, which are separated by two nucleotides within one individual strand. A distance of 1.4 *nm* (± 0.2 *nm*) was found for the spin labeled 'dA-dT' base pair **15(dA^{*7})•16(dT^{*6})**. The 'click' approach has the potential to be applied to all four constituents of DNA, indicating the universal applicability of the method. New insights into structural changes of canonical or modified DNA are expected which provide additional information on novel DNA structures, protein interaction, DNA architecture as well as synthetic biology.

6.2 Introduction

DNA is a polymorphic molecule forming a variety of three-dimensional structures such as A-, B- or Z-DNA and other motifs. Different base sequences can influence structural parameters such as groove width, local twist, curvature and mechanical rigidity[1]. These features help proteins to read and recognize one oligonucleotide sequence in preference to another, not only through chemical properties in the positions of nucleotide residues, but also on sequence-dependent structural features[2]. During the last decade, electron paramagnetic resonance (EPR) spectroscopy in combination with site-directed spin labeling (SDSL) has emerged as a powerful tool to investigate RNA/DNA architectures under biological conditions[3]. Recently, pulse EPR spectroscopy has been applied to DNA, focusing on B/A conformational transitions[4], DNA damages[5], and a nanometer distance ruler based on folded DNA/RNA has been developed[6]. To apply EPR spectroscopic protocols to DNA, unpaired electron spins have to be introduced and several paramagnetic species can be chosen for this purpose, e.g. metal ions,

Cu^{2+} or FeS clusters, radical centers and nitroxide spin labels which are chemically stable and geometrically fairly rigid[3]. Incorporation of spin labels into oligonucleotides should occur at defined positions with high efficiency, causing only small structural perturbations of DNA structure. However, the spin label should be rigid enough to reduce motion that obscures physical data.

Continuous wave (*cw*) EPR spectroscopy on spin labeled biomolecules provides information about the nitroxide side chain mobility[3], the polarity of its micro-environment[7], and about intra- or intermolecular distances between two spin labeled side chains in the distance range of 1-2 *nm*[8]. Double electron electron resonance (DEER) spectroscopy extends the measurable interspin distances up to 8 *nm*[9]. Until now, several approaches have been applied for spin labeling of RNA/DNA, as recently reviewed by Klare *et al*.[10] The nitroxide side chains can be introduced on the monomeric level – in phosphoramidites for solid-phase oligonucleotide synthesis[11] or triphosphates for enzymatic polymerization[12] as well as on the polymeric level by post-modification of oligonucleotides, RNA or DNA[6a, 13].

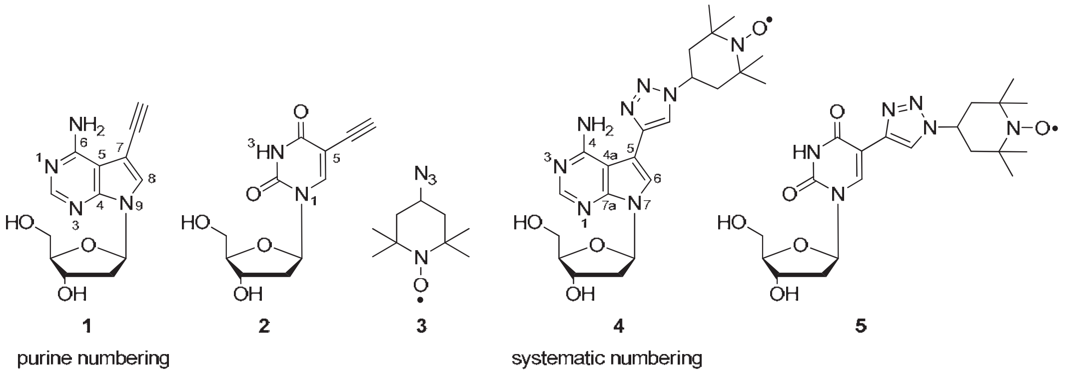

Figure 6.1 Structures of ethynyl-substituted nucleosides and 4-azido TEMPO conjugates.

A promising approach for spin labeling of oligonucleotides is the copper(I)-catalyzed *Huisgen-Sharpless-Meldal* alkyne-azide cycloaddition (CuAAC), so called 'click' reaction[14]. It has been proven to be an ideal bioorthogonal protocol for ligating functional molecules to biological or nonbiological materials in organic and aqueous reaction systems[15]. To avoid perturbation of the DNA structure, the click reaction is performed most efficiently when the ligand is introduced in the major groove of DNA. Consequently, 7-deazapurines have been used for modification at position-7 (purine numbering is used throughout the manuscript). Likewise, the 5-position of the pyrimidine base can be used for the same purpose

(Fig. 6.1)[16]. Our laboratory has many contributions to this matter over the years[17]. Recently, it was shown that reporter groups of moderate size can be introduced into the major groove of B-DNA by the CuAAC reaction[18].

This manuscript reports on the synthesis of oligonucleotides incorporating a derivative of 7-deaza-2′-deoxyadenosine (**1**) or 2′-deoxyuridine (**2**) bearing ethynyl side chains and their post-modification with nitroxide labels (Fig. 6.1)[19]. For this purpose, phosphoramidites of nucleosides **1** and **2** were synthesized and employed in solid-phase synthesis. The post-synthetic functionalization of oligonucleotides *via* 'click' chemistry was performed with 4-azido-2,2,6,6-tetramethyl-piperidine-1-oxyl (**3**; 4-azido TEMPO) (Scheme 7.1). For comparison, the reaction was studied on the nucleoside level yielding conjugates **4** and **5**. Two TEMPO residues were introduced at distant positions of a single stranded oligonucleotide. Further, a TEMPO residue was clicked to each nucleobase of a modified 'dA-dT' base pair within an oligonucleotide duplex incorporating the nucleosides **1** and **2**. For both approaches, distance measurements were performed using *cw* and pulse EPR spectroscopy.

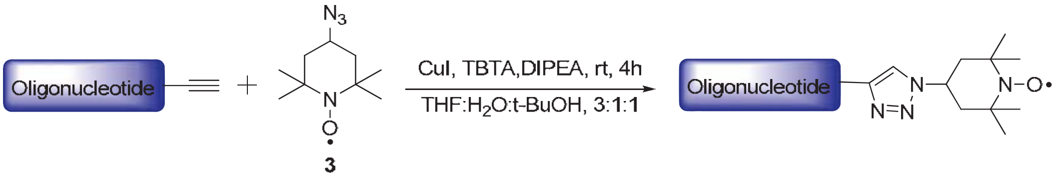

Scheme 6.1 Cu(I)-catalyzed 'click' reaction using the alkyne-azide cycloaddition.

6.3 Results and Discussion

Synthesis and properties of monomers

7-Deaza-7-ethynyl-2′-deoxyadenosine (**1**) was already synthesized earlier[19], but has not been incorporated into oligonucleotides, while the incorporation of nucleoside **2** in oligonucleotides was described[16]. Here, we report on the conversion of nucleoside **1** into the phosphoramidite building block **8**, which was employed in solid-phase oligonucleotide synthesis. For amino group protection of nucleoside **1**, the isobutyric residue was chosen[17a] and the protocol of transient protection was employed (→ **6**, 72% yield) (Scheme 6.2). Compound **6** was converted into the DMT derivative **7** under standard conditions (65 % yield). Phosphitylation with 2-cyanoethyl *N,N*-diisopropylchloro-phosphoramidite furnished the phosphoramidite **8** (83 % yield, Scheme 6.2). The phosphoramidite **9** was prepared according to a published procedure[16].

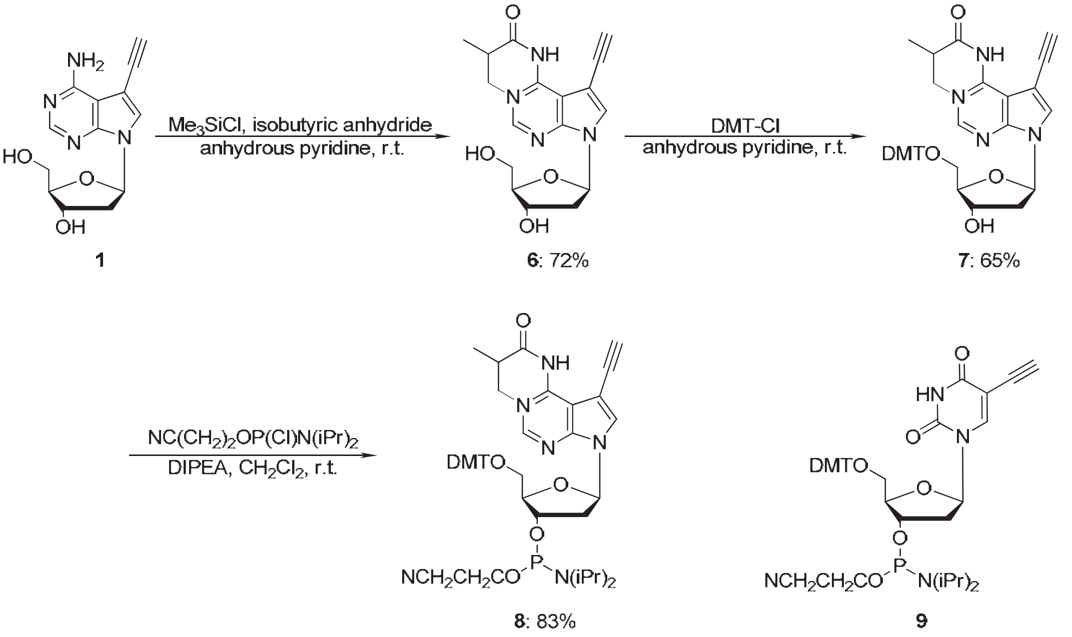

Scheme 6.2 Synthesis of phosphoramidite building block **8**.

Next, the click reaction was performed on nucleosides **1** or **2** with 4-azido-2,2,6,6-tetramethyl-piperidine-1-oxyl (**3**) (4-azido TEMPO). The paramagnetic radical, which contains an unpaired electron and a 'clickable' azido function, was synthesized from 4-hydroxy-2,2,6,6-tetramethyl-piperidine-1-oxyl according to the literature.[20] Then, the 7-ethynyl nucleosides **1** or **2** were functionalized with **3** by the click reaction to give the conjugates **4** or **5** in the presence of CuI in a 3:1:1 mixture of THF/*t*-BuOH/H_2O (Scheme 6.3). Addition of *N,N*-diisopropylethylamine (DIPEA) was essential for the completion of the reaction within 4 h. CuI has been used as copper(I) source instead of the Cu(II)SO_4/ascorbic acid system to avoid reduction of the nitroxide radical by ascorbic acid to the nonparamagnetic hydroxylamine derivative during click reaction[10, 21]. The spin labeled 1,2,3-triazolyl nucleoside conjugate **4** was obtained in 64%, while **5** was formed in 55 %.

All compounds were characterized by UV-spectra, ^{1}H and ^{13}C NMR spectra as well as by elemental analysis or mass spectra (experimental section, Table 6.2 and appendix A). All ^{1}H NMR signals of spin labeled compounds are broadened, and furthermore some atoms of the TEMPO residue are appearing neither in the ^{1}H nor in the ^{13}C NMR spectra. Also, the signal intensity of peaks obtained for the triazole moiety and partially for the nucleobase base is affected[22]. To verify presence of the intact spin label within the monomeric spin labeled conjugates **4** and **5**, they were subjected to EPR measurements, and the nitroxide label was confirmed (data not shown).

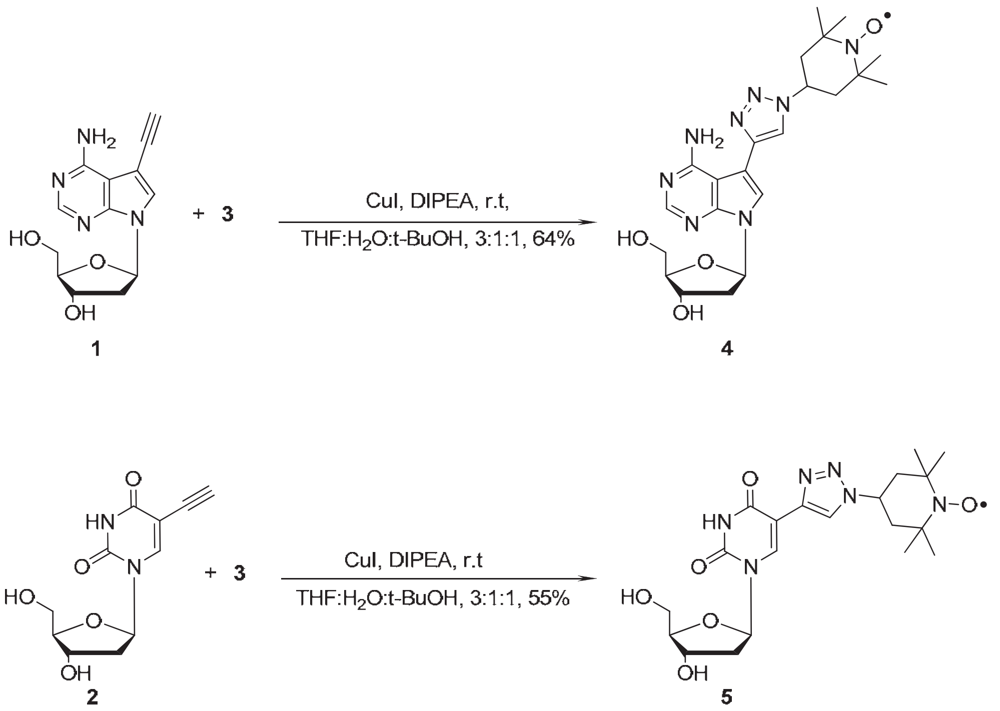

Scheme 6.3 Functionalization of nucleosides **1** and **2** with 4-azido TEMPO (**3**).

Synthesis and characterization of oligonucleotides for spin labeling

A series of oligonucleotides was synthesized (Table 6.1). After cleavage from the solid support, the oligonucleotides were deprotected according to the standard procedure (25 % aq. NH_3, 60 °C, 14-16 *h*). However, in the case of oligonucleotides containing 5-ethynyl-2′-deoxyuridine (**2**) significant amounts of side products were formed during the deprotection protocol with ammonia at elevated temperature (55 °C, 14-16 *h*). As the impurity shows a similar mobility on HPLC as the target molecule, it was necessary to change the deprotection conditions to room temperature (25 % aq. NH_3, 12 *h*). Consequently, tBPA-protected phosphoramidites were used[23]. Oligonucleotides were detritylated and purified by reversed-phase HPLC. The homogeneity of the oligonucleotides was confirmed by reversed-phase HPLC, as well as by MALDI-TOF mass spectrometry (see Appendix A). The base composition of oligonucleotides containing **1** and **2** was determined by enzymatic hydrolysis with snake venom phosphodiesterase followed by alkaline phosphatase and subsequent reversed-phase HPLC chromatography (see Appendix A).

Earlier, it was reported from our laboratory that the various 5-alkynyl pyrimidines and 7-alkynylated 7-deazapurines increase duplex stability by 1–3 °C per modification[18, 24]. Herein, we studied the impact of the ethynyl side chain of nucleosides **1** and **2** on duplex stability (Table 6.1). For this, the oligonucleotide duplex 5′-d(TAGGTCAATACT)-3′ (**10**) • 3′-d(ATCCAGTTATGA)-5′ (**11**) was used as reference. To be consistent with the conditions utilized in low temperature EPR experiments, 10 % glycerol (cryoprotectant) was added to the buffer solution throughout all T_m measurements. From Table 7.1, it can be seen that the replacement of a dA residue by 7-deaza-7-ethynyl-2′-deoxyadenosine (**1**) has a positive effect on duplex stability (T_m = 44 °C for **12•11**). This effect is more pronounced when multiple positions were modified with nucleoside **1** (**14•11**, ΔT_m = 2 °C per modification). According to Table 7.1, the replacement of one dT residue by 5-ethynyl-2′-deoxyuridine (**2**) has marginal influence on the duplex stability (T_m = 43 °C for duplex **10•13**). A similar result was obtained for the duplex **12•13** which contains one modified 'dA-dT' base pair of ethynyl substituted residues.

The thermal stability of duplexes in 0.1 *M* NaCl buffer with or without glycerol (data in parentheses) were compared and revealed a significant destabilization (**10•11**, **12•11**, **10•13**). These results are in agreement with previous work[25], reporting that glycerol reduces the thermal stability of duplexes by decreasing the number of water molecules interacting with the oligonucleotide solvation sites. This alters the electrostatic interactions within the polynucleotide chain and its counter ion surrounding. The influence of the spin label on duplex stability (oligonucleotide duplexes containing **4** or **5**) will be discussed later.

Introduction of nitroxide labels into oligonucleotides

Among the synthetic strategies to introduce spin labels into oligonucleotides, spin labeled phosphoramidites were already employed in solid-phase oligonucleotide synthesis[11]. Other approaches utilize backbone labeling. Either H-phosphonates or phosphorothioates were incorporated into the phosphodiester chain selectively and labeled afterwards with appropriately functionalized spin label derivatives[13b, 26]. As phosphorthioates prepared under standard conditions are diasteromeric, spin labeled conjugates with R_P or S_P configuration located in different environments of the DNA chain are formed. Another possibility is the application of thiooxo nucleosides as spin

Duplex	T_m [°C]	Δ T_m [°C]	$\Delta G°_{310}$ [kcal mol^{-1}][c]
5′- d(TAG GTC AAT ACT) (**10**) 3′- d(ATC CAG TTA TGA) (**11**)	43 (47)	--	- 9.7
5′- d(TAG GTC **1**AT ACT) (**12**) 3′- d(ATC CAG TTA TGA) (**11**)	44 (47)	+1	-9.9
5′- d(TAG GTC AAT ACT) (**10**) 3′- d(ATC CAG **2**TA TGA) (**13**)	43 (46)	0	-9.5
5′- d(TAG GTC **1**AT ACT) (**12**) 3′- d(ATC CAG **2**TA TGA) (**13**)	43	0	-9.2
5′- d(TAG GTC **1**AT **1**CT) (**14**) 3′- d(ATC CAG TTA TGA) (**11**)	47	+4	-10.6
5′- d(TAG GTC **4**AT ACT) (**15**) 3′- d(ATC CAG TTA TGA) (**11**)	40[b]	-3	-8.6
5′- d(TAG GTC AAT ACT) (**10**) 3′- d(ATC CAG **5**TA TGA) (**16**)	42[b]	-1	-9.3
5′- d(TAG GTC **4**AT ACT) (**15**) 3′- d(ATC CAG **5**TA TGA) (**16**)	37	-6	-8.0
5′- d(TAG GTC **4**AT **4**CT) (**17**) 3′- d(ATC CAG TTA TGA) (**11**)	41[b]	-2	-8.7

Table 6.1 T_m values of oligonucleotide duplexes containing ethynylated nucleosides and spin labeled conjugates[a]. [a] Measured at 260 *nm* in 0.1 *M* NaCl, 10 *mM* $MgCl_2$ and 10 % glycerol (pH 7.0) with 5 *μM* single-strand concentration. Data in parentheses were measured in 0.1 *M* NaCl, 10 *mM* $MgCl_2$ buffer (pH 7.0) without glycerol. [b] 10 % excess of the unmodified sequence. [c] The $\Delta G°_{310}$ values were determined from the melting curves using the software MELTWIN, version 3.0. The $\Delta G°_{310}$ values are given with 15 % deviation.

label targets, such as 4-thiouridine or 6-thioguanosine as target sites which were functionalized with methanethiosulfonates spin labels[27]. However, this approach is restricted to nucleobases, in which oxygen can be replaced by sulfur, such as 2′-deoxyuridine or 2′-deoxyguanosine. The resulting S-S bridges were obtained in high yields, but cleavage of the disulfide was observed over longer periods of time[27]. Another common protocol uses the *Sonogashira* cross-coupling reaction performed on a CPG-resin being used for solid-phase oligonucleotide synthesis. Here, fairly rigid spin labels were introduced into oligonucleotides[6a, 13d].

As we want to develop an efficient and universal protocol for spin labeling, this manuscript reports for the first time on the CuAAC click reaction for a direct oligonucleotide spin labeling using nucleobases as target sites. This approach shows the following advantages: (i) the simultaneous incorporation of two spins or even more labels in a highly efficient way, (ii) spin labeling can be accomplished at different nucleobases within one oligonucleotide strand, (iii) the target sites for spin labeling (nucleosides **1** and **2**) within one particular oligonucleotide can also be utilized for the introduction of other reporter groups, e.g. for FRET studies etc and (iv) accumulated information can be collected regarding structural changes by direct comparison of data obtained from the various labels introduced at identical positions by utilizing one particular oligonucleotide for post-modification. The click method, which is presented below can be performed on free oligonucleotides in solution, but is also applicable to solid support bounded oligonucleotides.

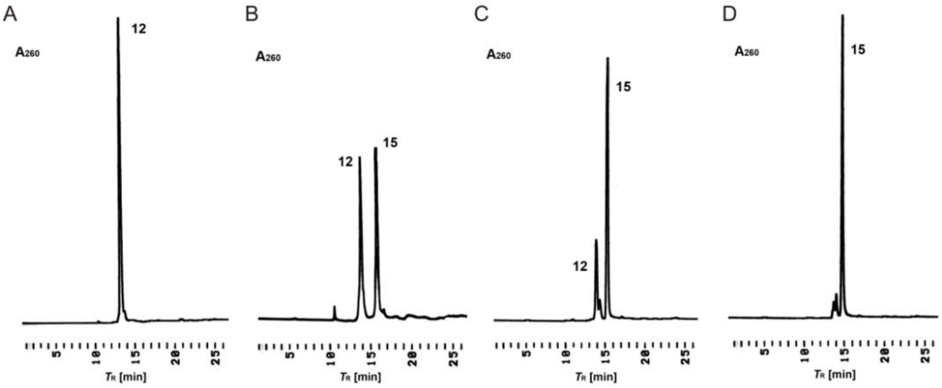

Figure 6.2 HPLC profiles of the Cu (I) catalyzed 'click' reaction of the oligonucleotide 5′-d(TAG GTC 1AT ACT) (12) with 4-azido TEMPO **3**, monitored in intervals by HPLC, 20 μl reaction mixture per injection (A) at 0 *min*; (B) at 60 *min*; (C) at 120 *min*; (D) at 240 *min*. Gradient: 0-30 *min* 0–60 % B in A, 30-40 *min* 60 % B in A, 60-0 % B in A, flow rate 0.7 $ml\ min^{-1}$ (A = 0.1 M $(Et_3NH)OAc$ (pH 7.0)/MeCN 95:5, B = MeCN).

Oligonucleotides with ethynyl substituted nucleosides **1** or **2** were functionalized with 4-azido TEMPO (**3**) in solution to produce paramagnetic oligonucleotides. The reaction was carried out in aqueous THF/H_2O/*t*-BuOH (3:1:1) at room temperature in the presence of the chelate ligand of CuI-TBTA [tris(benzyltriazolylmethyl)amine] and *N,N*–diisopropylethylamine (DIPEA) (Scheme 6.4). Due to the delicate nature of the nitroxide, no reducing reagent has been used during the 'click' reaction forming the oligonucleotide conjugate. Monitoring the click reaction in time intervals by HPLC shows that the starting material was consumed completely after 4 *h* (Fig. 6.2 and Appendix A). Labeled oligonucleotides were further purified by reversed-phase HPLC (RP-18 column).

The formation of click products was confirmed by MALDI-TOF mass spectrometry and enzymatic hydrolysis (see Appendix A). The reaction route is shown in Scheme 6.4.

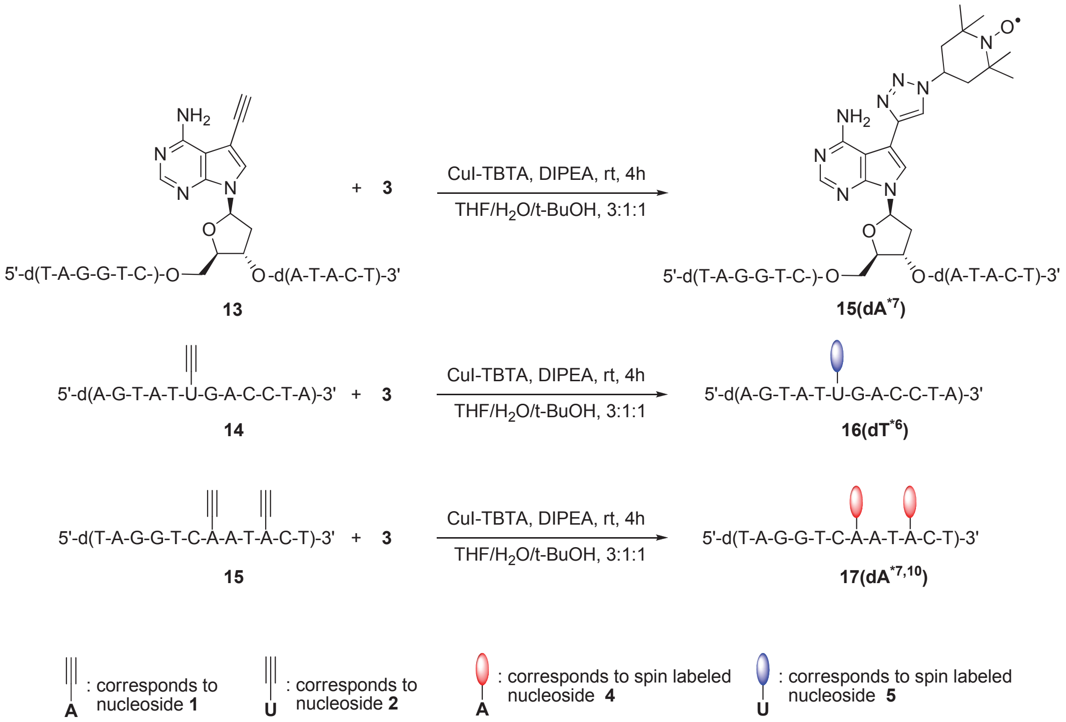

Scheme 6.4 Oligonucleotides labeled with 4-azido TEMPO (**3**) by click reaction. The abbreviations dA^{*7}, dT^{*6}, dA^{*7,10} correspond to the modified nucleoside (**4** or **5**) and its position within the oligonucleotide sequence indicated by the superscript number.

As discussed above, the ethynyl substituents of nucleoside **1** and **2** have a negligible influence on DNA stability. The short alkynyl side chain (2-3 *Å*), which is shorter than the depth of the B-DNA major groove (8.8 *Å*)[2] increases base-pair stability only slightly (Table 6.1). To evaluate the influence of the bulky spin label modification on duplex stability, oligonucleotides incorporating the functionalized residues **4** and **5**, both carrying a spin label, were investigated (Table 6.1). A single incorporation of the 7-deazapurine conjugate **4** at a central position [**15**(**dA**^{*7})•**11**] slightly destabilizes the 'dA-dT' base pair by 3 °C, while two incorporations of **4** [**17**(**dA**$^{*7,\,10}$)•**11**] do not destabilize the duplex further (-1 °C per modification). In the case of the 5-substituted 2´-deoxyuridine conjugate **5**, a similar trend was observed (**10**•**16**(**dT**^{*6}), ΔT_m = - 1 °C). It has to be noted that the T_m value of the duplex **15**(**dA**^{*7})•**16**(**dT**^{*6}) with a spin labeled 'dA-dT' base pair decreases the T_m

value by 6 °C. The above results clearly demonstrate that a single bulky spin label at position-7 of a 7-deazapurine or position-5 of a pyrimidine does not disturb the DNA duplex structure due to the noncritical position (C-7 of 7-deazapurine and C-5 of pyrimidine). However, when two spin labels are introduced at both sides of a 'dA-dT' base pair, the helix structure is slightly perturbed as reflected by the T_m decrease (Table 7.1). A destruction of the base pair is not occurring, as such a phenomenon would decrease the T_m value much stronger (ΔT_m = 10-15 °C).

EPR spectroscopy of spin labeled oligonucleotides

As melting data cannot answer questions regarding nanometer scale changes, EPR distance measurements were performed. In this regard, oligonucleotide duplexes with spatially isolated TEMPO residues or with nitroxides linked to each site of a base pair were investigated. Herein, *cw* and pulse EPR spectroscopy were utilized. A comparison of the room temperature spectra of the single and double labeled oligonucleotides is presented in Fig. 6.3. All spectra indicate a high mobility of the spin labeled side chains and the presence of only one distinct motional component; the spin labeled side chains are not restricted in the reorientational freedom by their immediate micro-environment. Interestingly, for the modified duplex **15**(**dA**^{*7}) •**16**(**dT**^{*6}), the amplitudes decrease from the low-field peak towards the high-field peak. In addition, considerable broadening of the lines compared to the spectra of the single labeled strand is obvious, which is due to spin-spin interaction. While the double labeled duplex **15**(**dA**^{*7})•**16**(**dT**^{*6}) reveals this anisotropic behavior, the single labeled duplex **15**(**dA**^{*7})•**11** and **10**•**16**(**dT**^{*6}) do not display such properties. Given that the anisotropic behavior is not caused by the constraints of neighboring nucleobases, the anisotropy is evidence for sterical interaction of the two spin labeled side chains or for a slightly perturbed 'dA-dT' base pair. The perturbation of the DNA structure is already reflected by the decreased T_m value of ΔT_m = - 6 °C (Table 6.1). On the contrary, the room temperature spectrum for the modified duplex with distant spin labels **17**(**dA**^{*7,10})•**11** does not exhibit any anisotropic behavior. No perturbation of the DNA structure caused by spin labeling and no interaction of both spin labels are observable in the spectrum, which is not unexpected, since both spin labels are at a distant position.

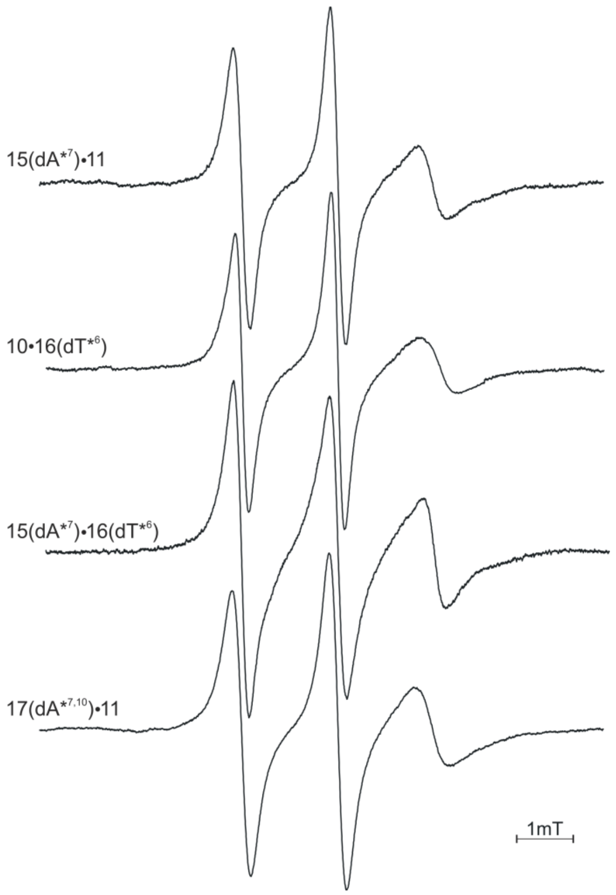

Figure 6.3 Room temperature (*T* = 298 *K*) *cw* EPR spectra at X-band (~ 9.4 *GHz*) measured in 0.1 *M* NaCl, 10 *mM* $MgCl_2$ and 10% glycerol (pH 7.0). All plots are normalized by amplitude.

Results of the *cw* and DEER measurements performed at 160 *K* and at 50 *K*, respectively, are depicted in Fig. 6.4. Tikhonov regularization of the data for the double labeled duplex **17(dA$^{*7, 10}$)•11** reveals a well defined single distance population with an interspin distance of 1.8 *nm* (± 0.2 *nm*) (Fig. 6.4, B). The width of 0.2 *nm* of the distance distribution is narrow, revealing half of the width found for an analogous labeled DNA duplex reported by Flaender *et al.*[28]. In fact, it is similar to a DNA duplex system with 4-amino-TEMPO attached to 2-fluorohypoxanthine bases[5]. Hence, the presented DNA system, spin labeled by the click reaction, is a powerful tool which enables accurate interspin distance measurements and is sensitive even to small structural changes. Furthermore, the rigid spin label will allow orientation selective studies to obtain the relative orientation of both spin labels as demonstrated by Schiemann *et al.*[29]

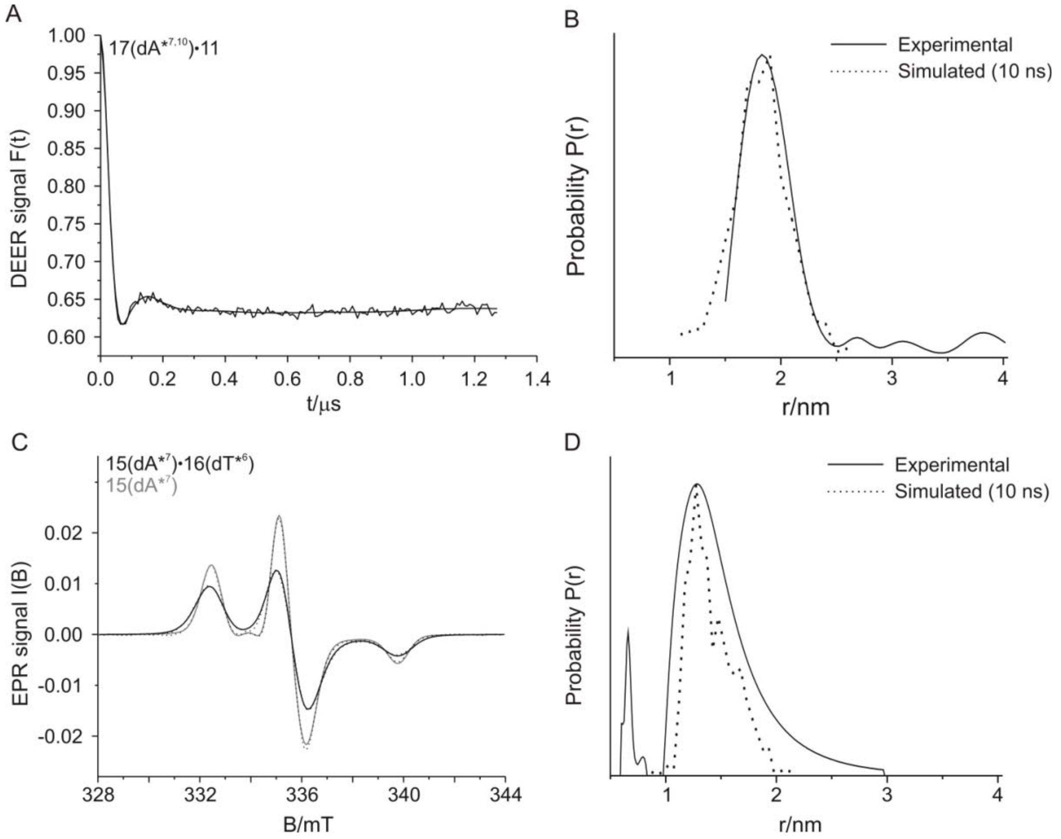

Figure 6.4 Low temperature (*T* = 50 *K*) DEER spectra of spin labeled duplex **17(dA$^{*7,\ 10}$)•11** at X-band (~ 9.4 *GHz*). (A) Background corrected dipolar evolution data *F(t)*. (B) Comparison of distance distributions *P(r)* obtained by Tikhonov regularization[33] of the pulse EPR spectrum (solid line) and simulated interspin distances using Yasara Dynamics (dotted line). (C): Low temperature (*T* = 160 *K*) *cw* EPR powder spectra at X-band. Experimental spectra of double labeled DNA duplex **15(dA^{*7})•16(dT^{*6})** (black solid line) and single labeled oligonucleotide **15(dA^{*7})** (grey solid line), the corresponding simulated EPR spectra are represented by dashed lines. All plots are normalized by spin number. (D) Comparison of distance distributions P(r) obtained by Tikhonov regularization (ShortDistances)[31] of the *cw* EPR spectrum (solid line) and interspin distances using Yasara Dynamics[34] (dotted line). All experiments are performed in 0.1 *M* NaCl, 10 *mM* $MgCl_2$ and 10 % glycerol (pH 7.0). Distance distributions are normalized by amplitude.

The data obtained for the double labeled duplex **15**(**dA**^{*7})**•16**(**dT**^{*6}) reveal an interspin distance below the accessible distance range of DEER spectroscopy (below 1.5 *nm*)[30] (data not shown). Therefore, we utilized *cw* EPR spectroscopy at 160 *K* to determine the interspin distance for **15**(**dA**^{*7})**•16**(**dT**^{*6}). No dipolar broadening appears for the single stranded oligonucleotide **15**(**dA**^{*7}), which is taken as a reference for the simulation of the dipolar broadening. In contrast, the experimental observed spectrum of **15**(**dA**^{*7})•**16**(**dT**^{*6}) exhibits significant dipolar broadening (Fig. 6.4, C). Fitting of simulated dipolar broadened EPR spectra (Fig. 6.4, D, dashed line) to the experimental one, utilizing the Tikhonov regularization approach provided by the program ShortDistances[31], yields a mean interspin distance of 1.4 *nm* (± 0.3 *nm*) and a fraction of the single spin labeled component of 11%. In addition, the data were fitted with the program DipFit[32], assuming a sum of Gaussian distributions of interspin distances. This results in a distance distribution centered at 1.4 nm (± 0.1 *nm*), and an A_{zz} value of 3.7 *mT*. The fraction of the single spin labeled component amounting to 10 %. The high A_{zz} value indicates a high polarity in the immediate micro-environment of the spin labeled side chains. Hence, the spin labeled side chains are accessible towards water molecules, which is in agreement with the DNA model (Fig. 6.5). The high spin labeling efficiency is reflected by the minor single labeled fraction of 10-11%. From the point of the physical measurement, a spin label should be rather rigid not showing significant independent movement with regard to the DNA duplex. Short alkynyl linkers[6a, 11a] or phenoxazine moieties[22b] fulfill these requirements. However, rigid and bulky spin labels affect DNA structure. They can stabilize or destabilize base pairs and provide a 'more or less' altered picture of the 'real' DNA duplex structure. On the other hand, a more flexible spin label is prone to independent movements but has a smaller influence on the duplex structure. Hence, a suitable compromise has to be found between the ease of synthesis, the universal character of the protocol, the rigidity of the label and the steric perturbation of the DNA structure induced by the label. We think that spin labeling using CuAAC affording spin labels linked via a *s*-1,2,3-triazole moiety fulfills most of these requirements. This is supported by the very small line width of the signals obtained from DEER measurements.

Comparison with molecular dynamics simulation

In order to analyze the effects induced by spin labeling on duplex structure and to provide a more comprehensive description, molecular dynamics (MD) simulations were performed on the DNA duplexes **15**(**dA**^{*7})•**16**(**dT**^{*6}) and **17**(**dA**$^{*7,\,10}$)•**11**. As a starting structure, both models were built with spin labels adjusted to their experimental determined distance using YASARA Dynamics (see experimental section for details).[34] For duplex **15**(**dA**^{*7})•**16**(**dT**^{*6}), the spin label leads to a marginal perturbation of the spin labeled 'dA-dT' base pair during the MD simulation. At the same time, the overall structure and in particular the base pair remains stable during the whole MD simulation of 10 *ns* as depicted in Fig. 6.5. The experimental *cw* EPR spectrum of **15**(**dA**^{*7})•**16**(**dT**^{*6}) at room temperature indicated

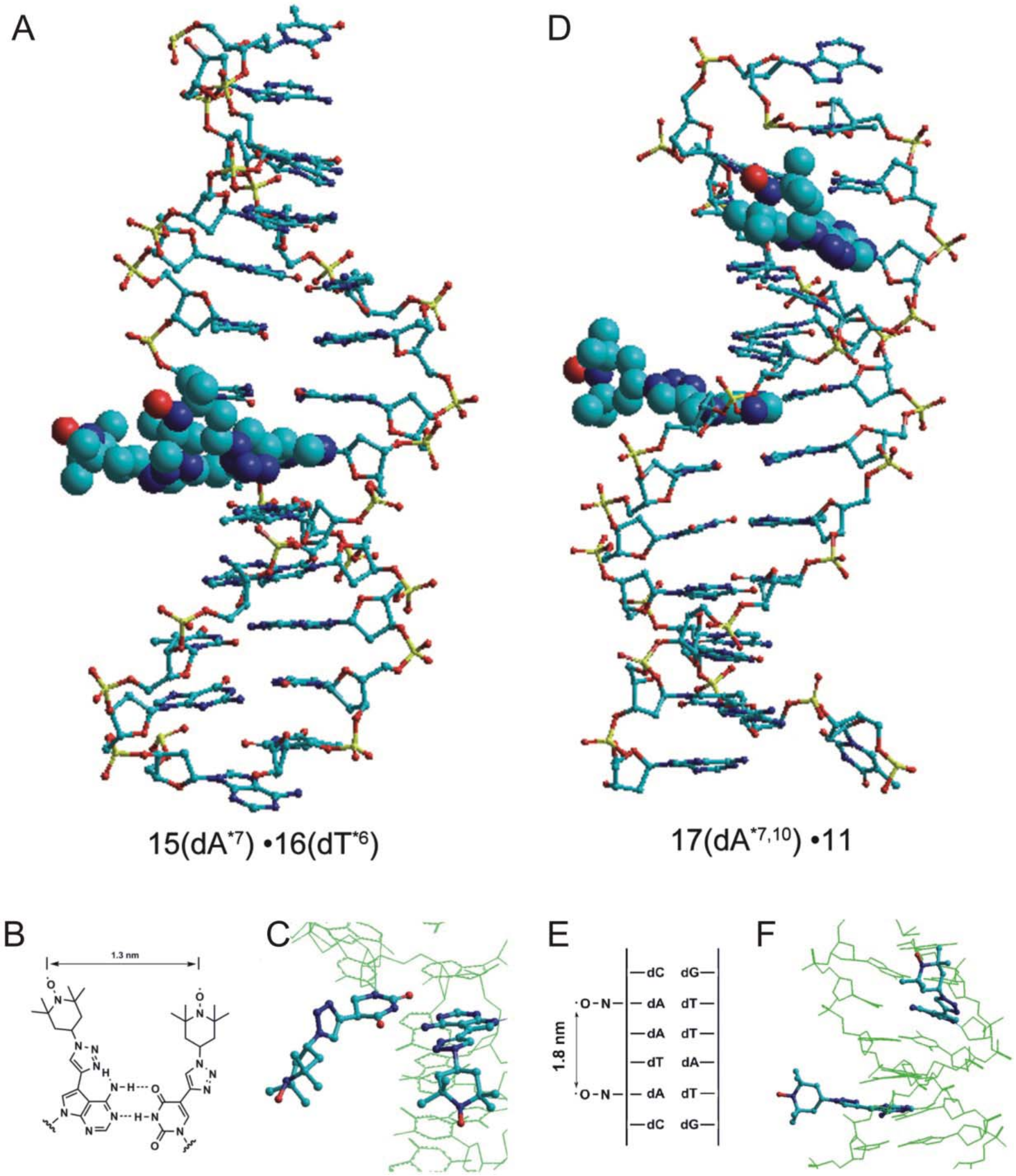

Figure 6.5 Molecular Dynamics (MD) simulation snapshots of the DNA duplexes **15(dA^{*7})•16(dT^{*6})** and **17(dA$^{*7,\ 10}$)•11**. The MD simulation were performed using AMBER99 force field implemented in YASARA Dynamics.[34] (A) MD simulation snapshot of DNA duplex **15(dA^{*7})•16(dT^{*6})**; (B) Modified base pair of **4** and **5** and the spin label distance, determined for the oxygen atoms of the nitroxides; (C) MD simulation snapshot of the spin labeled 'dA-dT' base pair, (D) MD simulation snapshot of DNA duplex **17(dA$^{*7,\ 10}$)•11**; (E) Spin spin distance for **17(dA$^{*7,\ 10}$)•11** containing two spin labels within one of the strands determined for the oxygen atoms of the nitroxides; (F) MD simulation snapshot of duplex **17(dA$^{*7,\ 10}$)•11**.

either a sterical interaction of the two spin labeled side chains or a disturbed 'dA-dT' base pair. Based on the MD simulation, we can exclude a disturbed base pair and conclude that sterical interaction leads to the anisotropic characteristic of the spectrum. For **15(dA^{*7})•16(dT^{*6})**, the simulated mean interspin distance is centered at 1.3 *nm* (± 0.2 *nm*) as shown in Fig. 6.4, B. Thus, there is reasonable agreement between experimental and simulated interspin distance distribution with a slight shift of the simulated interspin distance to shorter distances. Analysis of the data for duplex **17(dA^{*7,10})•11** exhibits an experimental determined interspin distance at 1.8 *nm* (± 0.2 *nm*) and a simulated mean interspin distance at 1.8 *nm* (± 0.2 *nm*) (Fig. 6.4, D). The agreement between the simulated and experimental interspin distance distributions is excellent, both for the interspin distances and the width of the distributions.

6.4 Conclusion

In this study, the TEMPO spin label was introduced in two DNA nucleobases (**1** and **2**) by the copper assisted azide-alkyne 'click' reaction. With this approach, a 'dA-dT' base pair was generated with one spin label linked to each nucleobase. Furthermore, one strand of a DNA duplex was modified with two spin labels in distant positions. Both post-modification reactions were performed with high efficiency. The spin labeling protocol performed on two ethynylated DNA constituents **1** (dA*) and **2** (dU*) can be extended to dG and dC derivatives, making all four DNA constituents – two pyrimidine bases and two purine bases in the form of 7-deazapurines – accessible. No interactions of two distant spin labels and a negligible perturbation of the DNA structure was observed [duplex **17(dA^{*7,10})•11**]. However, sterical interaction of spin labels and a small DNA structure perturbation was observed when two spin labels were linked to the 'dA-dT' base pair. By applying *cw* and pulse EPR spectroscopy, we were able to reveal interspin distances in the 1-2 *nm* range with high accuracy, namely a mean interspin distance of 1.4 *nm* (± 0.3 *nm*) for **15(dA^{*7}) 16(dT^{*6})** and 1.8 *nm* (± 0.2 *nm*) for **17(dA^{*7,10})•11**. For two spin labels in a more distant position, the determined distance distribution is exceptionally narrow and suitable for the identification of even small structural changes. Hence, the spin labeled DNA system obtained *via* 'click' reaction will allow us to provide detailed insights into structural changes caused by unusual DNA structures, by mispairing, DNA damages and/or lesions. Moreover, the target sites for spin labeling (ethynylated nucleosides **1** and **2**) within one particular oligonucleotide can also be utilized for the introduction of other reporter groups. Accumulated information can be collected regarding structural

DNA/RNA changes by direct comparison of data obtained from the various labels. Due to this, the click approach shows advantages over protocols described earlier.

6.5 Experimental Section

General

All chemicals were purchased from Acros, Aldrich, Sigma, or Fluka (Sigma-Aldrich Chemie GmbH, Deisenhofen, Germany). Solvents were of laboratory grade. Thin-layer chromatography (TLC) was performed on TLC aluminium sheets covered with silica gel 60 F254 (0.2 *mm*, VWR International, Germany). Flash column chromatography (FC): silica gel 60 (VWR International, Darmstadt, Germany) at 0.4 *bar*; UV-spectra were recorded on a U-3000 spectrophotometer (Hitachi, Japan); λ_{max} (ε) in *nm*, ε in $dm^3\ mol^{-1}\ cm^{-1}$. NMR spectra: DPX 300 spectrometer (Bruker, Germany) at 300 *MHz* for ^{1}H and 75 *MHz* for ^{13}C. The J values are given in Hz; δ values in *ppm* relative to Me_4Si as internal standard, or 85% H_3PO_4 for ^{31}P. For NMR spectra recorded in DMSO, the chemical shift of the solvent peak was set to 2.50 *ppm* for ^{1}H NMR and 39.50 *ppm* for ^{13}C NMR. Elemental analyses were performed by the Mikroanalytisches Laboratorium Beller, Göttingen, Germany. Reversed-phase HPLC was carried out on a 4 × 250 *mm* RP-18 (10 *mm*) LiChrospher 100 column (VWR International) with a Merck-Hitachi HPLC pump (Model L-6250) connected with a variable wavelength monitor (model 655-A), a controller (model L-500) and an integrator (model D-2500). Oligonucleotide synthesis, purification and characterization: The oligonucleotide syntheses were performed on a DNA synthesizer, model 392–08 (Applied Biosystems, Weiterstadt, Germany) at 1 *µmol* scale using the phosphoramidite 8 following the synthesis protocol for 3′-(2-cyanoethyl phosphoramidites) (user's manual for the 392 DNA synthesizer, Applied Biosystems, Weiterstadt, Germany). Oligonucleotides containing 5-ethynyl-2′-deoxyuridine (**2**) were prepared by using the corresponding phosphoramidite **9** and fast deprotection procedure.[16] For that, 4-tert-butylphenoxyacetyl-protected canonical phosphoramidites (Millipore) and the capping reagent 4-tert-butylphenoxyacetic anhydride instead of acetic anhydride were used. The coupling efficiency was always higher than 95 %. After cleavage from the support, the oligomers were incubated in a 25 % aq NH_3 solution. The following conditions were employed: (i) 60 °C, 14-16 *h* for oligonucleotides containing **1**; (ii) room temperature, 12 *h* for oligonucleotides containing **2**. The purification of 5′-*O*-dimethoxytrityl oligomers was carried out on reversed-phase HPLC (Merck-Hitachi-HPLC; RP-18 column; gradient system [A = 0.1 *M* (Et_3NH)OAc (pH 7.0)/MeCN 95:5, B = MeCN]: 3 *min* 20 % B in A, 12 *min* 20–50 % B in A, and 25 *min* 20 % B in A; flow rate 1.0 $ml\ min^{-1}$. The purified 'trityl-on'

	C2[c] C2[d]	C4[c] C6[d]	C4a[c] C5[d]	C5[c] C7[d]	C6[c] C8[d]	C7a[c] C4[d]	C≡C	triazole	C1′	C3′	C4′	C5′	C=O	$(MeO)_2$Tr
1[19]	152.7	157.5	102.3	93.9	127.0	149.1	82.9; 77.3	--	83.2	70.9	87.5	61.8	--	--
2[35]	149.5	144.5	97.5	--	--	161.6	83.6; 76.4	--	84.7	69.9	87.5	60.7	--	--
4	152.3	157.7	106.0	99.6	119.1	150.3	--	142.7; 118.4[e]	82.3	70.8	87.1	61.9	--	--
5	149.3	135.8	105.2	--	--	160.8	--	139.6; 119.8[e]	84.5	70.3	87.3	61.2	--	--
6	151.6	151.6	111.3	96.2	131.2	151.1	82.1; 77.3	--	83.1	70.9	87.6	61.7	175.8	--
7	151.6	151.6	111.3	96.2	131.1	151.0	82.1; 77.1	--	83.1	70.6	85.5	64.1	175.8	55.0

Table 6.2 ^{13}C-NMR chemical shifts (δ) of alkynylated nucleosides and spin labeled derivatives.[a], [b]

[a] Measured in DMSO-d_6 at 298 *K*.

[b] The signal of C2′ is superimposed by DMSO.

[c] Systematic numbering.

[d] Purine numbering.

[e] Decreased signal intensity by spin label.

oligonucleotides were treated with 2.5 % $CHCl_2COOH/CH_2Cl_2$ for 5 *min* at 0 °*C* to remove the 4,4′- dimethoxytrityl residues. The detritylated oligomers were purified again by reversed-phase HPLC (gradient: 0–20 min 0–20 % B in A; flow rate 1 *ml* min^{-1}). The oligomers were desalted on a short column (RP-18, silica gel) and lyophilized in a Speed-Vac evaporator to yield colorless solids which were frozen at -24 °C. The melting temperature curves were measured with a Cary-100 Bio UV-VIS spectrophotometer (Varian, Australia) equipped with a Cary thermoelectrical controller. The temperature was measured continuously in the reference cell with a Pt-100 resistor with a heating rate of 1 °*C* min^{-1}. The thermodynamic data of duplex formation were calculated by the Meltwin 3.0 program. The enzymatic hydrolysis of the oligonucleotides containing **1**, **2**, **4** and **5** were performed as described[17a] with snake venom phosphodiesterase (EC 3.1.15.1, *Crotallus adamanteus*) and alkaline phosphatase (EC 3.1.3.1, *Escherichia coli* from Roche Diagnostics GmbH, Germany) in 0.1 *M* Tris-HCl buffer (pH 8.3) at 37 °*C*. The hydrolysis product was analyzed by reversed-phase HPLC (RP-18). Quantification of the constituents was made on the basis of the peak areas, which were divided by the extinction coefficients ε_{260} of the nucleosides: dA 15 400, dC 7300, dG 11700, dT 8800, 1 11100 (MeOH), 2 10500 (MeOH), 4 10500 (MeOH), 5 7600 (MeOH). MALDI-TOF mass spectra were recorded in the linear negative mode with an Applied Biosystems Voyager DE PRO spectrometer with 3-hydropicolinic acid (3-HPA) as a matrix. The detected masses were identical with the calculated values (see Appendix A).

Preparation of oligonucleotides for EPR measurements

Lyophilized DNA samples were dissolved in 0.1 *M* NaCl, 10 *mM* $MgCl_2$ and 10 % glycerol (pH 7.0), yielding a concentration of 60 μM for the single-stranded oligonucleotides and 60 μM for the DNA duplexes, respectively. Glycerol was added as a cryoprotectant during all low temperature EPR experiments. For low temperature *cw* and pulse EPR experiments, 30-40 *µl* of the sample solution was filled into EPR quartz capillaries with 4 *mm* and 3 *mm* outer diameter, respectively, and frozen in liquid nitrogen before insertion into the resonator. Sample volumes of 10 *µl* were loaded into EPR quartz capillaries with a 0.9 *mm* inner diameter for *cw* EPR measurements at room temperature.

EPR measurements

Room temperature *cw* EPR spectra at X-band were recorded using a Magnettech Miniscope MS200 X-band spectrometer equipped with a rectangular TE102 resonator. To avoid saturation and to obtain high signal-to-noise ratio EPR spectra, the microwave power was set to 10 *mW* and the B-field modulation amplitude was adjusted to 0.15 *mT*. Low temperature *cw* EPR spectra for interspin distance determination in the range of 1-2 *nm* were recorded at 160 *K* using a homemade X-band EPR spectrometer equipped with a Super High Sensitivity Probehead (Bruker). Temperature stabilization was achieved by a continuous flow helium cryostat (ESR 900, Oxford Instruments) in combination with a temperature controller (ITC 503S, Oxford Instruments). The microwave power was set to 0.2 *mW* and the B-field modulation amplitude adjusted to 0.25 *mT*. A B-NM 12 B-field meter (Bruker) allowed measurement of the magnetic field. The DEER experiments were performed at 50 *K* and X-band frequencies (9.4 *GHz*) using a Bruker Elexsys 580 spectrometer equipped with a 3-mm split ring resonator (ER 4118X-MS3, Bruker). The resonator was overcoupled to Q ~ 100 as measured by the software Xepr (Bruker). A continuous flow cryostat (ESR900, Oxford Instruments) in combination with a temperature controller (ITC 503S, Oxford Instruments) were used for temperature stabilization. The following four-pulse DEER sequence was used:

$$\pi/2(\upsilon_{obs}) - \tau_1 - \pi\,(\upsilon_{obs}) - t' - \pi\,(\upsilon_{pump}) - (\tau_1 + \tau_2 - t') - \pi\,(\upsilon_{obs}) - \tau_2 - \mathit{echo}^{[36]} \tag{6.1}$$

A two-step phase cycling (+ ‹x›, - ‹x›) was realized on $\frac{\pi}{2}(\upsilon_{obs})$, while for all pulses at the observer frequency the ‹x› channels were applied. The pump pulse possessed a length of 12 *ns* and the pump frequency υ_{pump} was positioned at the center of the resonator dip. This frequency corresponds to the maximum of the echo-detected nitroxide EPR absorption spectrum. The observer frequency υ_{obs} was set to the low field local maximum of the absorption spectrum which resulted in a 65 *MHz* offset with an observer pulse lengths of 16 *ns* for $\frac{\pi}{2}$ and 32 *ns* for π pulses. Time t' was varied, whereas τ_1 and τ_2 were kept constant. Deuterium modulation was averaged by adding traces at eight different τ_1 start values, starting at $\tau_{1,0}$ = 200 *ns* and incrementing by $\Delta\,\tau_1 = 8$ *ns*. The dipolar evolution time was given by $t = t' - \tau_1$ and data with $t > 0$ were analyzed.

Fitting of experimental *cw* EPR spectra

Fitting of the simulated dipolar broadened *cw* EPR spectra to the experimental one recorded at low temperatures below 200 *K* reveal the average interspin distance in the range of 1-2 *nm* as described before using the programs DipFit[32] or ShortDistances.[31] Heisenberg exchange interaction does not lead to significant distance errors as long as the through space distances exceeds 1.0 *nm*[8, 32]. However, for distances below 1.0 *nm* or in case exchange is facilitated through bonds connecting the nitroxides influences of exchange interaction have to be considered. DipFit determines best-fit parameters for the interspin distance and distance distribution considering a Gaussian distribution of distances. During the fitting procedure, the g tensor values, the A_{xx} and A_{yy} values of the hyperfine tensor and the Lorentzian and Gaussian line width parameters are fixed to the values found for the reference spectra 16(dA^{*7}). In detail, A_{xx} and A_{yy} were fixed to 0.68 and 0.66 *mT*, respectively, whereas A_{zz} is variable. The g tensor values are set to $g_{xx} = 2.0082$, $g_{yy} = 2.0070$, $g_{zz} = 2.0022$. The EPR spectra are convoluted with a field-independent line shape function composed of a superposition of 28 % Lorentzian and 72 % Gaussian of 0.51 and 0.42 *mT* widths, respectively. The fraction of single spin labeled component is variable. Utilizing the program ShortDistances[31], the interspin distance distribution is calculated by Tikhonov regularization. The interspin distance as well as the width, and the fraction of single spin labeled component are adjustable during the fitting procedure.

Analysis of DEER data

Analysis of DEER experiments exhibits interspin distances in the range of 1.5-8 *nm* based on the dipolar coupling frequency of dipolar coupled spins. The lower limit of DEER experiments depends on the excitation bandwidth of the pump pulse which has to be larger than the dipolar coupling of the spins and is in our case 1.5 *nm*[30]. To elucidate only interspin distances within one nanoscopic object, the intermolecular background contribution has to be separated from the intramolecular contribution. Therefore the experimental echo decay is background-corrected using a homogeneous three-dimensional spin distribution followed by normalization of the function. Finally the interspin distance distributions are calculated by fitting the corrected dipolar evolution function using Tikhonov regularization as implemented in DEERAnalysis2006[33].

Molecular dynamics simulation

The molecular dynamics (MD) simulation was performed using the AMBER99 force field implemented in YASARA Dynamics[34] with periodic cell boundaries. A simulation cell was constructed with 12 *Å* real space around the DNA model and filled with water molecules and Na^+/Cl^- counter ions at locations of the lowest/highest electrostatic potential during a cell neutralization and pK_a prediction experiment (pH 7.0). After an energy minimization run, the final 10 *ns* MD simulation was done at 298 *K* with 1 *fs* time steps under constant pressure, while intermolecular forces were calculated every 2 *fs*. Periodic boundary crossing of solute atoms was prevented by means of the function solute drift. The interspin distances were extracted using the macro MD analyzes provided by YASARA Dynamics.

7-(2-Deoxy-ß-D-*erythro*-pentofuranosyl)-4-(isobutyrylamino)-5-ethynyl-7*H*-pyrrolo[2,3-*d*]pyrimidine (6)

To a stirred solution of compound 1[19] (274 *mg*, 1 *mmol*) in anhydrous pyridine (5 *ml*) was added Me_3SiCl (1.16 *ml*, 9.10 *mmol*) at room temperature. After 45 *min*, isobutyric anhydride (1.16 *ml*, 7.38 *mmol*) was introduced, and the solution was stirred for another 2 *h*. The mixture was cooled to 0 °*C*, diluted with H_2O (5 *ml*) and stirred for 10 *min*. After the addition of 12 % aq. NH_3 (5 *ml*), stirring was continued for 1 *h* at room temperature. The solvent was evaporated, and the residue was applied to flash chromatography (FC; silica gel, column 10 × 3 cm, CH_2Cl_2/CH_3OH 95:5). Compound 6 was isolated as a colorless solid (248 *mg*, 72 %). R_f=0.42 (CH_2Cl_2/CH_3OH 90:10); ^{1}H NMR (300 *MHz*, DMSO-d_6, 25 °C): δ=1.14 (s, 6H; $2CH_3$), 2.26 (m, 1H; H_α-2'), 2.58 (m, 1H; CH), 2.78 (m, 1H; H_β-2'), 3.43 (m, 2H; H-5'), 3.84 (m, 1H; H-4'), 4.08 (s, 1 H; C≡CH), 4.37 (m, 1H; H-3'), 5.04 (t, ^3J(H,H)=5.3 Hz, 1H; OH-5'), 5.35 (d, ^3J(H,H)=4.0 Hz, 1H; OH-3'), 6.62 (t, ^3J(H,H)=6.4 Hz, 1H; H-1'), 8.12 (s, 1H; H-6), 8.62 (s, 1H; H-2), 10.21 *ppm* (s, 1H; NH); UV/Vis (MeOH): λ_{max} (ε)=238 (53 000), 278 (26 000 *mol*$^{-1}$*dm*^{3}*cm*$^{-1}$); elemental analysis calcd (%) for $C_{17}H_{20}N_4O_4$: C 59.29, H 5.85, N 16.27; found: C 59.03, H 5.84, N 16.35.

7-[2-Deoxy-5-*O*-(4,4′-dimethoxytrityl)-*ß*-D-*erythro*-pentofuranosyl]-4-(isobutyrylamino)-5-ethynyl-7*H*-pyrrolo-[2,3-*d*]pyrimidine (7)

Compound 6 (241.1 *mg*, 0.7 *mmol*) was dried by repeated co-evaporation with anhydrous pyridine (3 × 5 *ml*) before dissolving in anhydrous pyridine (5 *ml*). To this solution, 4,4′-dimethoxytrityl chloride (DMT-Cl) (284.6 *mg*, 0.84 *mmol*) was added in three portions. The remaining solution was stirred for 3 *h* at room temperature. The reaction was quenched by the addition of MeOH (2 *ml*), and the mixture was stirred for another 30 *min*. The reaction mixture was diluted with CH_2Cl_2 (2 × 10 mL) and extracted with 5 % aqueous $NaHCO_3$ (30 *ml*) followed by H_2O (40 *ml*), dried over Na_2SO_4 and then evaporated to dryness. Purification by FC (silica gel, column 15 × 3 cm, CH_2Cl_2/acetone 95:5 → 90:10) gave a colorless foam of 7 (295 mg, 65 %). R_f=0.64 (CH_2Cl_2/CH_3OH 90:10); ^{1}H NMR (300 MHz, DMSO-d_6, 25 °C): δ=1.15 (s, 6H; $2CH_3$), 2.31 (m, 1H; H_α-2'), 2.67 (m, 1H; CH), 2.81 (m, 1H; H_β-2'), 3.16 (m, 2H; H-5'), 3.72 (s, 6H; OCH_3), 3.96 (m, 1H; H-4'), 4.07 (s, 1 H; C≡CH), 4.38 (m, 1H; H-3'), 5.40 (d, ^3J(H,H)=4.5 Hz, 1H; OH-3'), 6.62 (t, ^3J(H,H)=6.6 Hz, 1H; H-1'), 6.84 (m, 4H; Ar-H), 7.16–7.40 (m, 9H; Ar-H), 7.95 (s, 1H; H-6), 8.60 (s, 1H; H-2), 10.17 ppm (s, 1H; NH); UV/Vis (MeOH): λ_{max} (ε)=235 (56 000), 276 (18 000 *mol*$^-$

^{1}dm^{3}cm^{-1}); elemental analysis calcd (%) for $C_{38}H_{38}N_4O_6$: C 70.57, H 5.92, N 8.66; found: C 70.32, H 5.82, N 8.70.

7-[2-Deoxy-5-*O*-(4,4′-dimethoxytrityl)-*ß*-D-*erythro*-pentofuranosyl]-4-(isobutyrylamino)-5-ethynyl-7*H*-pyrrolo-[2,3-*d*]pyrimidin-3′-(2-cyanoethyl)-*N,N*-diisopropylphosphoramidite (8)

Compound 7 (259 *mg*, 0.4 *mmol*) was dissolved in anhydrous CH_2Cl_2 (3.0 *ml*) under Ar atmosphere and 2-cyanoethyl *N,N*-diisopropylchlorophosphoramidite (185 *µl*, 0.78 *mmol*) and *N,N*-diisopropylethylamine (150 *µl*, 0.87 *mmol*) were added at room temperature. After stirring 20 *min*, the reaction mixture was diluted with CH_2Cl_2 and washed with 5 % aqueous $NaHCO_3$, followed by brine. The organic layer was separated, dried over anhydrous Na_2SO_4, filtrated and evaporated to dryness. The residue was dissolved in 1 *ml* CH_2Cl_2 and submitted to FC (column 4 × 10 cm, CH_2Cl_2/acetone, 9:1) yielding a colorless foam of 8 (287.8 *mg*, 83%); R_f=0.44 (CH_2Cl_2/acetone, 70:10); ^{31}P NMR (121.5 MHz, $CDCl_3$, 25 °C): δ=148.87; 148.70 *ppm*.

4-Amino-7-(2-deoxy-b-d-erythro-pentofuranosyl)-5-[1-(2,2,6,6-tetramethyl-1-ylooxypiperidin-4-yl)-1,2,3-triazol-4-yl]-7H-pyrrolo[2,3-d]pyrimidine (4)

Compound 1 (137 *mg*, 0.5 *mmol*) and 4-azido-2,2,6,6-tetramethyl-1-piperidinyloxy radical (3) (118 *mg*, 0.6 *mmol*) were dissolved in THF/H_2O/*t*-BuOH (3:1:1, v/v, 5 *ml*), then *N,N*-diisopropylethylamine (80 *µl*, 0.46 *mmol*) was added, followed by the addition of copper(I) iodide (143 *mg*, 0.75 *mmol*). The reaction mixture was stirred for 4 *h* at room temperature. The solvent was evaporated, and the residue was purified by FC (silica gel, column 4 × 10 *cm*, CH_2Cl_2/MeOH 10:1) to give 4 as a pink solid, which was crystallized from H_2O, yielding pink crystals (151 *mg*, 64 %). R_f=0.53 (CH_2Cl_2/CH_3OH 90:10); ^{1}H NMR (300 MHz, DMSO-*d*$_6$, 25 °C): δ=1.16-1.23 (m, 17H; 4CH_3, 2CH_2, CH, low intensity), 2.41 (br, 2H; H_α-2′, H_β-2′), 3.48 (br, 2H; H-5′), 3.84 (br, 1H; H-4′), 4.38 (br, 1H; H-3′), 5.04 (s, 1H; OH-5′), 5.31 (s, 1H; OH-3′), 6.57 (s, 1H; H-1′), 7.39 (br, H; NH_2), 7.88 (s, 1H; H-6), 8.10 (s, 1H; H-2), 9.03 *ppm* (br, H; NH_2); UV/Vis (MeOH): λ_{max} (ε)=245 (14 400), 279 (10 800 *mol^{-1}dm^{3}cm^{-1}*); MS (ESI) m/z: calcd for $C_{22}H_{31}N_8O_4$: 472.25; found: 472.25 $[M+H]^+$.

1-(2-Deoxy-b-d-erythro-pentofuranosyl)-5-[1-(2,2,6,6-tetramethyl-1-ylooxypiperidin-4-yl)-1,2,3-triazol-4-yl]uracil (5)

As described for 4, compound 2 (126 *mg*, 0.5 *mmol*) in THF/H_2O/*t*-BuOH (3:1:1, v/v, 5 *ml*) was treated with 4-azido-2,2,6,6-tetramethyl-1-piperidinyloxy radical (3) (118 *mg*, 0.6 *mmol*), in the presence of *N,N*-diisopropylethylamine (80 µL, 0.46

mmol) and copper(I) iodide (143 *mg*, 0.75 *mmol*). Purification by FC (silica gel, column 4 × 10 *cm*, CH_2Cl_2/MeOH 10:1) gave 5 as pink solid, which was crystallized from H_2O, yielding light pink crystals (124 *mg*, 55 %). R_f=0.46 (CH_2Cl_2/CH_3OH 90:10); ^1H NMR (300 MHz, DMSO-d_6, 25 °C): δ=1.13-1.24 (m, 17H; $4CH_3$, $2CH_2$, CH, low intensity), 2.19 (br, 2H; H_α-2′, H_β-2′), 3.59 (m, 2H; H-5′), 3.85 (m, 1H; H-4′), 4.28 (br, 1H; H-3′), 5.03 (s, 1H; OH-5′), 5.30 (s, 1H; OH-3′), 6.24 (s, 1H; H-1′), 8.59 (br, H; H-6), 11.71 *ppm* (s, H; NH); UV/Vis (MeOH): λ_{max} (ε)=291 (14 200), 232 (18 400 $mol^{-1}dm^3cm^{-1}$); elemental analysis calcd (%) for $C_{20}H_{29}N_6O_6$ (449.49): C 53.44, H 6.50, N 18.70; MS (ESI) m/z: calcd for $C_{20}H_{29}N_6O_6$: 472.20; found: 472.20 $[M+Na]^+$.

General procedure for the cycloaddition of oligonucleotides with 4-azido-2,2,6,6-tetramethyl-piperidine-1-oxyl (3)

To a ss-oligonucleotide (5 A_{260} units) were added TBTA ligand (100 *µl* of a 20 *mM* stock solution in THF/H_2O/*t*-BuOH, 3:1:1), *N,N*-diisopropylethylamine (2 *µl* of a 1% stock solution in water), CuI (10 *µl*, 20 *mM* stock solution in THF/H_2O/*t*-BuOH, 3:1:1), 4-azido-2,2,6,6-tetramethyl-1-piperidinyloxy radical (3, 50 *µl* of a 20 *mM* stock solution in THF/H_2O/*t*-BuOH, 3:1:1), and the reaction mixture was stirred at room temperature for 4 *h*. The reaction mixture was concentrated in a Speed-Vac, dissolved in 500 *µl* bidistilled water and centrifuged for 30 *min* at 14 000 *rpm*. The supernatant solution was collected and further purified by reversed-phase HPLC with the gradient 0-30 *min* 0-60% B in A, 30-40 *min* 60% B in A, 40-50 *min* 60-0% B in A, flow rate 0.7 $cm^3\,min^{-1}$.

6.6 References

[1] a) W. Saenger, *Principles of Nucleic Acid Structure*, Springer-Verlag, New York, 1984; b) V. A. Bloomfield, D. M. Crothers, I. Tinoco, Jr. *Nucleic Acids: Structures, Properties and Functions*, University Science Books, Sausalito, CA, **1999**, pp. 79-108.

[2] G. M. Blackburn, M. J. Gait, D. Loakes, D. M. Williams, *Nucleic acids in chemistry and biology*, *Vol. 5*, The Royal Society of Chemistry, Cambridge, **2006**, pp 383-422.

[3] a) R. S. Keyes, A. M. Bobst in *Biological Magnetic Resonance: Spin labeling. The Next Millennium*, *Vol. 14* (Eds.: L. J. Berliner), Plenum Press, New York **1989**, pp. 283-334; b) O. Schiemann, T. F. Prisner, *Q Rev Biophys* **2007**, *40*, 1-53; c) A. Marko, D.Margraf, P. Cekan, S. T. Sigurdsson, O. Schiemann, T. F. Prisner, *Phys. Rev. E* **2010**, *81*, 021911.

[4] G. Sicoli, G. Mathis, O. Delalande, Y. Boulard, D. Gasparutto, S. Gambarelli, *Angew. Chem. Int. Ed.* **2008**, *47*, 735-737.

[5] G. Sicoli, G. Mathis, S. Aci-Sèche, C. Saint-Pierre, Y. Boulard, D. Gasparutto, S. Gambarelli, *Nucleic Acids Res.* **2009**, *37*, 3165-3176.

[6] a) O. Schiemann, N. Piton, Y. Mu, G. Stock, J. W. Engels, T. F. Prisner, *J. Am. Chem. Soc.* **2004**, *126*, 5722-5729; b) O. Schiemann, A. Weber, T. E. Edwards, T. F. Prisner, S. T. Sigurdsson, *J. Am. Chem. Soc.* **2003**, *125*, 3434-3435.

[7] H.-J. Steinhoff, A. Savitsky, C. Wegener, M. Pfeiffer, M. Plato, K. Möbius, *Biochim. Biophys. Acta, Bioenerg.* **2000**, *1457*, 253-262.

[8] H. J. Steinhoff, *Biol. Chem.* **2004**, *385*, 913-920.

[9] P. P. Borbat, J. H. Freed, *Chem. Phys. Lett.* **1999**, *313*, 145-154.

[10] J. P. Klare, H.-J. Steinhoff, *Photosynth. Res.* **2009**, *102*, 377-390.

[11] a) A. Spaltenstein, B. H. Robinson, P. B. Hopkins, *Biochemistry* **1989**, *28*, 9484-9495; b) C. Giordano, F. Fratini, D. Attanasio, L. Cellai, *Synthesis* **2001**, 565-572.

[12] S. Obeid, M. Yulikov, G. Jeschke, A. Marx, *Angew. Chem. Int. Ed.* **2008**, *47*, 6782-6785.

[13] a) F. Hansske, K. Watanabe, F. Cramer, F. Seela, *Hoppe Seyler's Z. Physiol. Chem.* **1978**, *359*, 1659-1665; b) P. Z. Qin, S. E. Butcher, J. Feigon, W. L. Hubbell, *Biochemistry* **2001**, *40*, 6929-6936; c) N.-K. Kim, A. Murali, V. J. DeRose, *Chem. Biol.* **2004**, *11*, 939-948; d) N. Piton, Y. Mu, G. Stock, T. F. Prisner, O. Schiemann, J. W. Engels, *Nucleic Acids Res.* **2007**, *35*, 3128-3143; e) Q. Cai, A. K. Kusnetzow, W. L. Hubbell, I. S. Haworth, G. P. Gacho, N. Van Eps, K. Hideg, E. J. Chambers, P. Z. Qin, *Nucleic Acids Res.* **2006**, *34*, 4722-4730.

[14] a) H. C. Kolb, M. G. Finn, K. B. Sharpless, *Angew. Chem. Int. Ed.* **2001**, *40*, 2004-2021; b) M. Meldal, C. W. Tornøe, *Chem. Rev.* **2008**, *108*, 2952-3015; c) F. Amblard, J. H. Cho, R. F. Schinazi, *Chem. Rev.* **2009**, *109*, 4207-4220; d) R. Huisgen, *Angew. Chem. Int. Ed.* **1963**, *2*, 565-598; e) R. Huisgen in *1,3-Dipolar Cycloaddition Chemistry*, *Vol. 2* (Eds: A. Padwa), Wiley, New York, **1984**; f) V. V. Rostovtsev, L. G. Green, V. V. Fokin, K. B. Sharpless, *Angew. Chem. Int. Ed.* **2002**, *41*, 2596-2599.

[15] P. M. E. Gramlich, C. T. Wirges, A. Manetto, T. Carell, *Angew. Chem. Int. Ed.* **2008**, *47*, 8350-8358.

[16] D. Graham, J. A. Parkinson, T. Brown, *J. Chem. Soc., Perkin Trans. 1* **1998**, 1131-1138.

[17] a) F. Seela, M. Zulauf, *Chem. Eur. J.* **1998**, *4*, 1781-1790; b) X. Peng, H. Li, F. Seela, *Nucleic Acids Res.* **2006**, *34*, 5987-6000; c) F. Seela, X. Peng, S. Budow, *Curr. Org. Chem.* **2007**, *11*, 427-462.

[18] F. Seela, V. R. Sirivolu, P. Chittepu, *Bioconjugate Chem.* **2008**, *19*, 211-224.

[19] F. Seela, M. Zulauf, *Synthesis* **1996**, 726-730.

[20] N. G. Bushmakina, A. Y. Misharin, *Synthesis* **1986**, 966-966.

[21] M. Kveder, G. Pifat, S. Pečar, M. Schara, P. Ramos, H. Esterbauer, *Chem. Phys. Lipids* **1997**, *85*, 1-12.

[22] a) P. Cekan, S. T. Sigurdsson, *J. Am. Chem. Soc.* **2009**, *131*, 18054-18056; b) M. Sajid, G. Jeschke, M. Wiebcke, A. Godt, *Chem. Eur. J.* **2009**, *15*, 12960-12962.

[23] N. D. Sinha, P. Davis, N. Usman, J. Pérez, R. Hodge, J. Kremsky, R. Casale, *Biochimie* **1993**, *75*, 13-23.

[24] M. Ahmadian, P. Zhang, D. Bergstrom, *Nucleic Acids Res.* **1998**, *26*, 3127-3135.

[25] D. Liang, L. Song, Z. Chen, B. Chu, *J. Chromatogr. A* **2001**, *931*, 163-173.

[26] S. Nagahara, A. Murakami, K. Makino, *Nucleosides and Nucleotides* **1992**, *11*, 889 - 901.

[27] P. Z. Qin, K. Hideg, J. Feigon, W. L. Hubbell, *Biochemistry* **2003**, *42*, 6772-6783.

[28] M. Flaender, G. Sicoli, T. Fontecave, G. Mathis, C. Saint-Pierre, Y. Boulard, S. Gambarelli, D. Gasparutto, *Nucleic Acids Symp. Ser.* **2008**, *52*, 147-148.

[29] O. Schiemann, P. Cekan, D. Margraf, T. F. Prisner, S. T. Sigurdsson, *Angew. Chem. Int. Ed.* **2009**, *48*, 3292-3295.

[30] a) G. Jeschke, Y. Polyhach, *Phys. Chem. Chem. Phys.* **2007**, *9*, 1895-1910; b) J. E. Banham, C. M. Baker, S. Ceola, I. J. Day, G. H. Grant, E. J. J. Groenen, C. T. Rodgers, G. Jeschke, C. R. Timmel, *J. Magn. Reson.* **2008**, *191*, 202-218.

[31] C. Altenbach, W. L. Hubbell, *Biophys. J.* **2008**, *94, Supplement 1*, 826-832.

[32] H.-J. Steinhoff, N. Radzwill, W. Thevis, V. Lenz, D. Brandenburg, A. Antson, G. Dodson, A. Wollmer, *Biophys. J.* **1997**, *73*, 3287-3298.

[33] G. Jeschke, V. Chechik, P. Ionita, A. Godt, H. Zimmermann, J. Banham, C. R. Timmel, D. Hilger, H. Jung, *Appl. Magn. Reson.* **2006**, *30*, 473-489.

[34] a) E. Krieger, T. Darden, S. B. Nabuurs, A. Finkelstein, G. Vriend, *Proteins: Struct., Funct., Bioinf.* **2004**, *57*, 678-683; b) E. Krieger, G. Koraimann, G. Vriend, *Proteins: Struct., Funct., Bioinf.* **2002**, *47*, 393-402.

[35] V. Borsenberger, M. Kukwikila, S. Howorka, *Org. Biomol. Chem.* **2009**, *7*, 3826-3835.

[36] M. Pannier, S. Veit, A. Godt, G. Jeschke, H. W. Spiess, *J. Magn. Reson.* **2000**, *142*, 331-340.

7

Site-directed spin labeling by ’click reaction’ reveals DNA conformational changes induced by mismatches

7.1 Abstract

Multiple forms of DNA damages such as base modifications, double-strand breaks and mispairings are related to inheritable diseases, cancer and aging. Here, the dynamics and structural changes of canonical DNA and DNA incorporating mismatched duplexes are examined by EPR spectroscopy. Two ethynyl-7-deaza-2′-deoxyadenosine residues were incorporated in DNA at distant positions and functionalized with 4-azido-2,2,6,6-tetramethyl-piperidine-1-oxyl (4-azido TEMPO) by the 'click' reaction. Mismatches such as dT·dT or dA·dA mispairs were positioned between these two spin labels in DNA duplexes. The overall mobility of the spin label side chains appears to be unaltered by this modification. Orientation selective pulse EPR experiments reveal changes in interspin distances which depend on the type and nearest neighbor environment of the mismatch.

7.2 Introduction

2′-Deoxyribonucleic acid (DNA) is the carrier of genetic information in living organisms. DNA mutations such as nucleobase changes, double-strand breaks and mispairings are associated with inheritable diseases, cancer and aging.[1-3] *In vivo*, DNA mismatches are usually caused by the misincorporation of nucleotides during replication[4], mutagenic compounds[5,6] or ionizing radiation[7]. This can lead to structural and conformational changes of DNA domains with biological impact in respect of mutagenicity. Consequently, such alterations, if not repaired, have severe effects on the cellular machinery. Conformational changes can be monitored by intramolecular distance measurements, which provide new insights into structure-function relationships[8-10]. Nanometer distance measurements related to mutagenic events involving DNA structural changes have been determined by high-resolution NMR spectroscopy[11], fluorescence resonance energy transfer (FRET)12 and X-ray crystallography[13,14]. Recently, the high sensitivity and accuracy of EPR spectroscopy on spin labeled oligonucleotides have been demonstrated under conditions close to the physiological state[15-18]. Several techniques have been developed for the spin labeling of nucleic acids. The highly exergonic character of the copper(I)-catalyzed Huisgen-Sharpless-Meldal alkyne-azide cycloaddition (CuAAC), the so called 'click' reaction, was used for spin labeling of DNA on solid-phase by Sigurdsson and co-workers[19] and in solution by the Seela and Steinhoff groups[20]. A 7-ethynyl derivative of 7-deaza-2′-deoxyadenosine (**1**) was incorporated in an oligonucleotide, followed by the click functionalization with 4-azido-2,2,6,6-tetramethyl-piperidine-1-oxyl (**2**; 4-azido TEMPO) leading to derivative **3** (Fig. 7.1)[20]. This reaction occurred with high efficiency without perturbing the DNA duplex structure. Pulse EPR experiments revealed an exceptional narrow distance distribution which enables identification of even small mismatch-induced structural changes of oligonucleotides. However, rigid spin labels may lead to a specific mutual orientation of both reporter groups[21-23]. Therefore, the determination of interspin distance distributions under the assumption of an isotropic distribution of spin label orientations, as applied in common data analysis programs, may be inaccurate. Consequently, the pulse EPR spectra and the derived distance distributions might be modulated by this effect. A pulse EPR study by Schiemann *et al.* using compound "Ç " as spin label, first introduced by Barhate *et al.*[24], revealed that an accurate determination of distances and relative orientations of spin centers in nucleic acids can be achieved by orientation selective pulse EPR experiments at X-band frequencies[21].

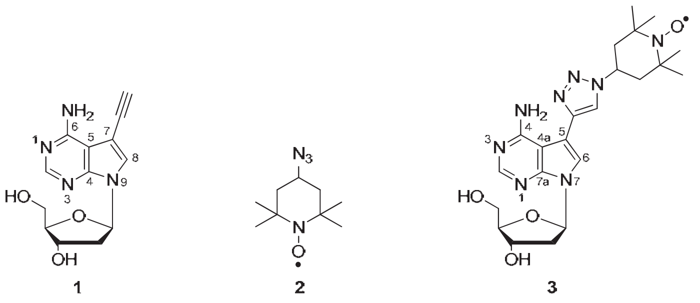

purine numbering

systematic numbering

Figure 7.1 Structures of 7-ethynyl-7-deaza-2′-deoxyadenosine and 4-azido TEMPO conjugates.

Here, we provide insight into structural changes of DNA caused by mismatch formation. To this end, continuous wave (*cw*) and orientation selective pulse EPR spectroscopy were used to examine the changes in the structure and dynamics of unmodified and modified spin labeled DNA duplexes. Mismatches were incorporated into oligonucleotides containing nucleoside derivative **1** as reactive group and the 4-azido TEMPO spin label **2** introduced by the 'click' reaction. Four mismatched constructs with dT·dT and dA·dA pairs located between two spin labeled positions (Table 7.1 and Scheme 7.1) were synthesized and analyzed. The results reveal that the spin label dynamics in all modified DNA duplexes are unaffected, independently of the position or the type of incorporated mismatches, whereas changes of the interspin distances appear due to the incorporation of mismatches.

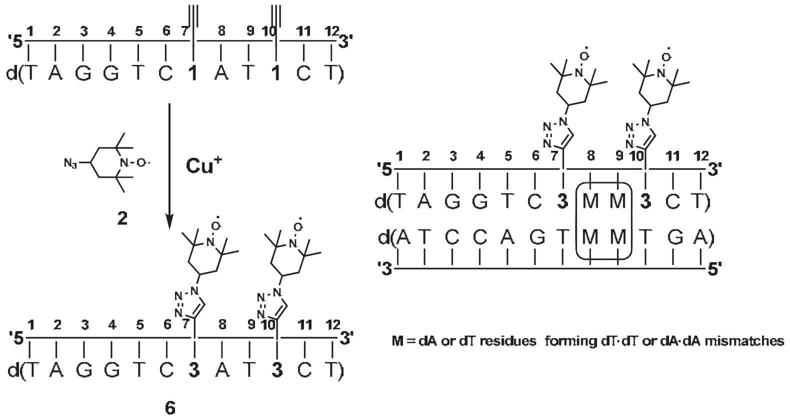

Scheme 7.1 Spin labeling of DNA by click reaction and formation of duplexes containing one dT·dT or dA·dA mismatch in position 8 or 9.

7.3 Materials and methods

Synthesis and characterization of oligonucleotides for spin labeling

The protocols of synthesis and characterization of oligonucleotides have been described[20,25]. The functionalization of oligonucleotides with 4-azido-2,2,6,6-tetramethyl-piperidine-1-oxyl (**2**) using *Huisgen-Sharpless-Meldal* alkyne-azide cycloaddition (CuAAC) was reported previously[20]. The oligonucleotides were purified by reversed-phase HPLC, and characterized by MALDI-TOF mass spectrometry and enzymatic hydrolysis. The melting curves were measured with a Cary-100 Bio UV-VIS spectrophotometer (Varian, Australia) equipped with a Cary thermoelectrical controller. The temperature was measured continuously in the reference cell with a Pt-100 resistor with a heating rate of 1 *°C* min^{-1}. The thermodynamic data of duplex formation were calculated by the Meltwin 3.0 program.

Continuous wave (*cw*) EPR experiments

Lyophilized DNA mutants were dissolved in 0.1 *M* NaCl, 10 *mM* $MgCl_2$ and 10 % glycerol (pH 7.0) yielding a concentration of 60 *μM* for single and double stranded variants. Sample volumes of 10 *μl* were filled into EPR quartz capillaries with 0.9 *mm* inner diameter for *cw* EPR measurements at room temperature. *Cw* EPR spectra at X-band were recorded using a homemade EPR spectrometer equipped with a Bruker dielectric resonator in combination with a liquid flow cryostat (liquid containing 30 % ethylene glycole, 70 % water) to adjust the sample temperature to 285 *K*. The microwave power was set to 1 *mW* and the B-field modulation amplitude adjusted to 0.15 *mT*. Fitting of simulated EPR spectra to the experimental was performed according to a Brownian model of isotropic reorientational diffusion of the nitroxide[26] with two distinct spectral components. Due to the fact that the experimental spectra reflect an almost isotropic reorientational motion of the nitroxide, the fraction of the component characterized by longer correlation times was in the range of 5-10 %. For the fitting procedure the g and A tensor values were fixed, whereas rotational diffusion constants and the ratio of the two spectral components were allowed to vary. The reorientational correlation time τ_c was calculated from the obtained rotational diffusion constant R according to $\tau_c = (6 \times R)^{-1}$.

Pulse EPR experiments

For all pulse EPR experiments 30-40 *µl* of the sample solution in 0.1 *M* NaCl, 10 *mM* $MgCl_2$ (pH 7.0) with a DNA concentration of 60 *µM* was loaded into EPR quartz capillaries with 3 *mm* outer diameter. 10 % Glycerol was added as cryoprotectant. The sample was frozen in liquid nitrogen before insertion into the resonator. Pulse EPR measurements were performed at 50 *K* and X-band frequencies (~ 9.4 *GHz*) using a Bruker Elexsys 580 spectrometer equipped with a 3-*mm* split ring resonator (ER 4118X-MS3, Bruker). A continuous flow cryostat (ESR900, Oxford Instruments) in combination with a temperature controller (ITC 503S, Oxford Instruments) was used for temperature stabilization. The four-pulse DEER sequence[27] was applied and the data analyzed as described recently[20]. For orientation selective experiments the observer frequency υ_{obs} was varied to achieve a 40, 65 and 80 *MHz* frequency offset between observer and pump pulses. All the other parameters were kept unmodified with respect to the previously specified values[20].

7.4 Results and Discussion

A series of oligonucleotides were synthesized by solid-phase phosphoramidite synthesis, deblocked under mild deprotection conditions and purified by reversed-phase HPLC. Ethynylated oligonucleotide strands **6** and **7** were functionalized with 4-azido-2,2,6,6-tetramethyl-piperidine-1-oxyl (**2**) as reported previously using copper(I) catalyzed *Huisgen-Sharpless-Meldal* alkyne-azide cycloaddition (CuAAC)[20]. The formation of click products was confirmed by MALDI-TOF mass spectrometry and enzymatic hydrolysis (see Appendix B, Table B.1 and Fig. B1). The selected spin labeled single strands were hybridized with unmodified second strand in low salt buffer (0.1 *M* NaCl, 10 *mM* $MgCl_2$ and 10% glycerol, pH 7.0) yielding a set of duplexes with canonical base pairs (**6·5**) or containing dT·dT or dA·dA mismatches (**7·5**, **6·8**, **6·9, 10·5**). So, two bidentate dA·dT base pairs are located in the center of the duplex between two spin labeled positions. Tridentate dC·dG base pairs surround the spin labels at both sites (positions 6 and 11), thereby stabilizing the local structure. These positions were chosen to separate the impact of changes of the micro-environment of the spin label from those introduced by mispairings. Effects induced by mispairing and hybridization are further distinguished by investigation of double labeled, unmodified single stranded (**6**) and double stranded DNA (**6·5**).

	Duplex	T_m [°C]	ΔT_m [°C]	r_{mean} [nm]	$\lvert\Delta r_{mean}\rvert$ [nm]	w_{mean} [nm]	$\lvert\Delta w_{mean}\rvert$ [nm]
6	5′-d(TAG GTC **3**AT **3**CT)	--	--	2.09	0.05	1.10	0.10
6·5	5′-d(TAG GTC **3**AT **3**CT) 3′-d(ATC CAG TTA TGA)	41	-2	1.80	0.02	0.56	0.02
7·5	5′-d(TAG GTC **3T**T **3**CT) 3′-d(ATC CAG T**T**A TGA)	29	-14	1.73	0.01	0.50	0.04
6·8	5′-d(TAG GTC **3**A**T** **3**CT) 3′-d(ATC CAG TT**T** TGA)	28	-15	1.86	0.04	0.55	0.07
6·9	5′-d(TAG GTC **3A**T **3**CT) 3′-d(ATC CAG T**A**A TGA)	22	-21	1.73	0.03	0.58	0.11
10·5	5′-d(TAG GTC **3**A**A** **3**CT) 3′-d(ATC CAG TT**A** TGA)	24	-19	2.08	0.03	0.63	0.02

Table 7.1 T_m values of oligonucleotide duplexes containing spin labeled conjugates[a] and parameters for the interspin distance distributions (r_{mean}, $\lvert\Delta r_{mean}\rvert$, w_{mean} and $\lvert\Delta w_{mean}\rvert$) determined by orientation selective EPR experiments and Tikhonov regularization (DEERAnalysis2006)[33].

[a] Measured at 260 nm in 0.1 *M* NaCl, 10 *mM* $MgCl_2$ and 10 % glycerol (pH 7.0) with 5 *μM* single-strand concentration.

The formation of mismatches does not only cause changes of the thermodynamics and kinetics of a particular canonical base pair but it also affects nearest neighbors. Consequently, the nearest neighbor model for Watson-Crick base pairs was extended to interactions between mismatches and neighboring base pairs[28,29]. It was shown that with the exception of terminal positions the thermodynamics of a mismatch is independent of its position within a particular duplex but depends on the local environment of the mismatch. For the duplexes containing one mismatched pair in between the spin labels, a thermodynamic analysis was performed (cf. Table 7.1). To be consistent with the conditions utilized in low temperature EPR experiments, 10 % glycerol was added to the buffer solution throughout all T_m measurements. The introduction of the two spin labels resulted in a decreased T_m value of 41 °*C* with ΔT_m = -2 °*C* compared to the T_m value of the unmodified DNA duplex indicating a nearly undisturbed helix structure due to the uncritical positions of the spin labels at C-7 of the 7-deazapurine moiety. It was reported that the presence of dA·dA or dT·dT mismatch in the center of a duplex reduces the T_m value significantly[30-32]. According to the experimental results (Table 7.1), substitution of a dA·dT base pair by a dT·dT mispair destabilized the duplex by 14 °*C* (T_m = 29 °*C* for **7·5**). A similar result was obtained for duplex **6·8** containing the dT·dT mismatch close to the second spin label towards the 5′- end of the duplex (ΔT_m = -15 °C). More pronounced destabilizations have been found in case of a dA·dA mismatch. The T_m values are decreased by 19-21 °*C* (T_m = 22 °*C* for **6·9**, T_m = 24 °*C* for **10·5**). In all cases, the significant decrease of T_m values caused by incorporation of mismatches reflects their destabilizing property.

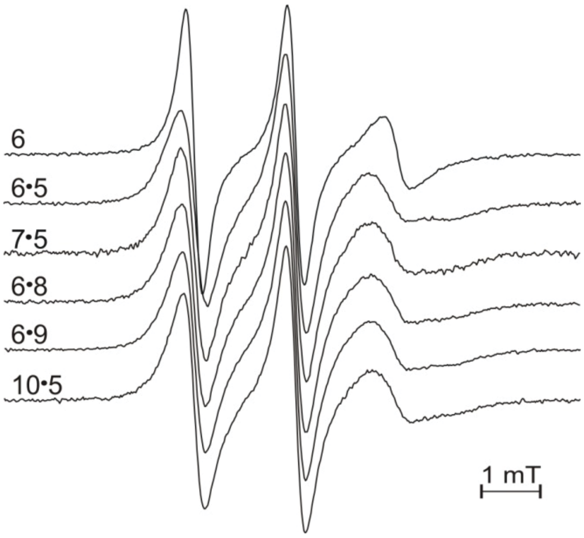

Figure 7.2 *Cw* EPR spectra (T = 285 *K*) at X-band (~ 9.4 *GHz*) measured in 0.1 *M* NaCl, 10 *mM* MgCl2 and 10 % glycerol (pH 7.0). All plots are normalized to constant amplitude.

EPR spectra recorded at 285 *K* (Fig. 7.2) reveals that the freedom for reorientational motion of both spin label side chains is only marginally restricted by sterical interaction with the DNA structure. For the single stranded, double labeled DNA **6** the peak amplitude ratios of the three hyperfine lines reveal the highest mobility of the spin label side chains compared to all other constructs with a reorientational correlation time of 1.3 *ns*. Hybridization with the complementary strand leads to less mobile spin label side chains. The reorientational correlation times for the

DNA duplexes are about 2.4 *ns*. This change may reflect changes in the rotational correlation time for the entire DNA molecule or for the residual motion of the spin label side chain. Based on the Stokes-Einstein relation and taking a spherical single stranded DNA molecule and a molecular weight of 1.8 *kDa* into account, the calculation of the reorientational correlation time τ yields a reorientational correlation time of 1.0 *ns*. This value is in the same order of magnitude like the simulated value of the experimental spectrum for the single stranded DNA. Thus, the change of the reorientational correlation time upon hybridization with the complementary strand is most likely due to the increased molecular weight by a factor of two and changes in the motion of the entire DNA molecule and not due to a change of the residual motion of the spin label side chain. Matched and mismatched DNA do not reveal any significant differences in the overall spin label mobility, neither the type of incorporated mismatches nor their locations affect the spin label side chain mobility.

Interspin distances were determined using pulse EPR spectroscopy (PELDOR). Since orientation correlation between the spin labels affects the PELDOR data, this has been considered by the application of three orientation selective pulse EPR experiments ($\Delta\nu$ = 40, 65, 80 *MHz*) for each of the samples as depicted in Fig. 7.3. Both, the mean interspin distances, r_{mean}, and the mean widths, w_{mean}, (full width at half maximum) were calculated from the distance distributions corresponding to the orientation selective pulse EPR experiments for the respective spin labeled oligonucleotides (see Table 7.1). The mean interspin distances and the distance distribution widths vary slightly with the frequency offset indicating the effect of orientation correlation between the spin labels. The maximal variances of the experimentally determined interspin distances and distribution widths are $|\Delta r_{mean}| \leq 0.05$ *nm* and $|\Delta w_{mean}| \leq 0.11$ *nm*, respectively. Remarkably, the asymmetric shape of the distance distribution for **10·5** is observed for all three orientation selective experiments. For the respective spin labeled oligonucleotides, the shapes of the Fourier transformations of the background corrected dipolar evolution function, the so called Pake pattern, resemble each other (cf. Fig. 7.4).

The variance in the mean interspin distances $|\Delta r_{mean}|$ induced by orientation selection is similar to the ones reported by Sicoli *et al.*[9], however, the variance in the present distribution widths is three times higher. Sicoli *et al.* incorporated spin labels using the 2-amino group of the guanine base as modification site, and a TEMPO label was introduced *via* nucleophilic displacement of a 2-fluoro substituent by an amino-TEMPO derivative. Due to their structure, these spin labels perform a cone-shaped motion. The cone angle in the present case of the 1,2,3-triazole linker is larger, which in turn leads to the observed enlarged distribution width.

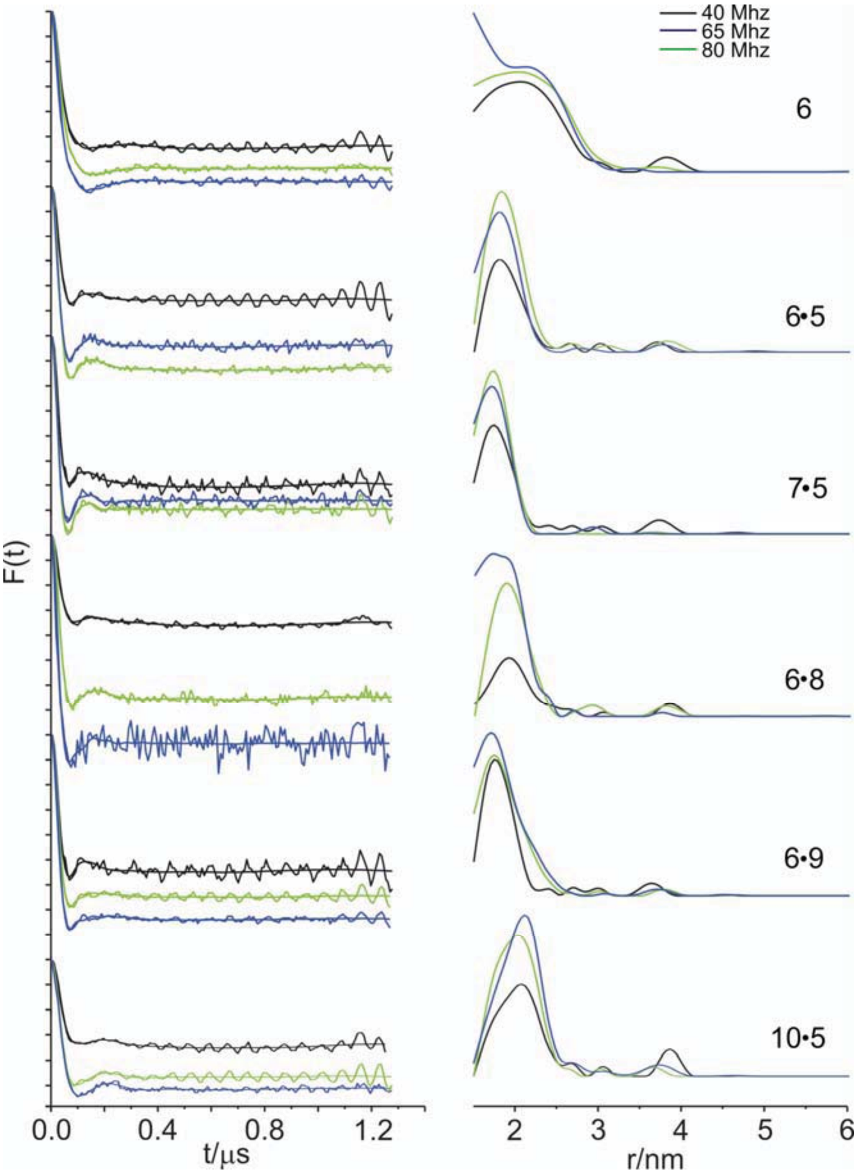

Figure 7.3 Low temperature (T = 50 *K*) orientation selective pulse EPR spectra at X-band (~ 9.4 GHz) measured in 0.1 *M* NaCl, 10 *mM* $MgCl_2$ and 10 % glycerol (pH 7.0) for the frequency offsets 40, 65 and 80 *MHz* (black, green and blue lines, respectively). Left: background corrected dipolar evolution data F(t). Tick marks are separated by 0.05. Right: distance distributions P(r) obtained by Tikhonov regularization (DeerAnalysis2006)[33]. Weak contributions from proton modulations are visible with a frequency of about 14.6 *MHz*. Data analysis and distance distribution determination are not significantly affected, as the proton modulation frequency would correspond to a distance of about 1.5 *nm*.

Changes of the mean interspin distances, r_{mean}, due to the incorporation of mismatches into the double stranded DNA were found to be in the range from 0.06

nm to 0.28 *nm* (cf. Table 7.1). These differences are significant, since they are up to five times larger than the distance variations due to orientation correlation. In contrast, changes of the distribution width as a result of the incorporation of mismatches are in the range of 0.01 *nm* to 0.07 *nm*, which is less than the variance of the distribution width of $|\Delta w_{mean}| \leq 0.11$ *nm* caused by orientation selection.

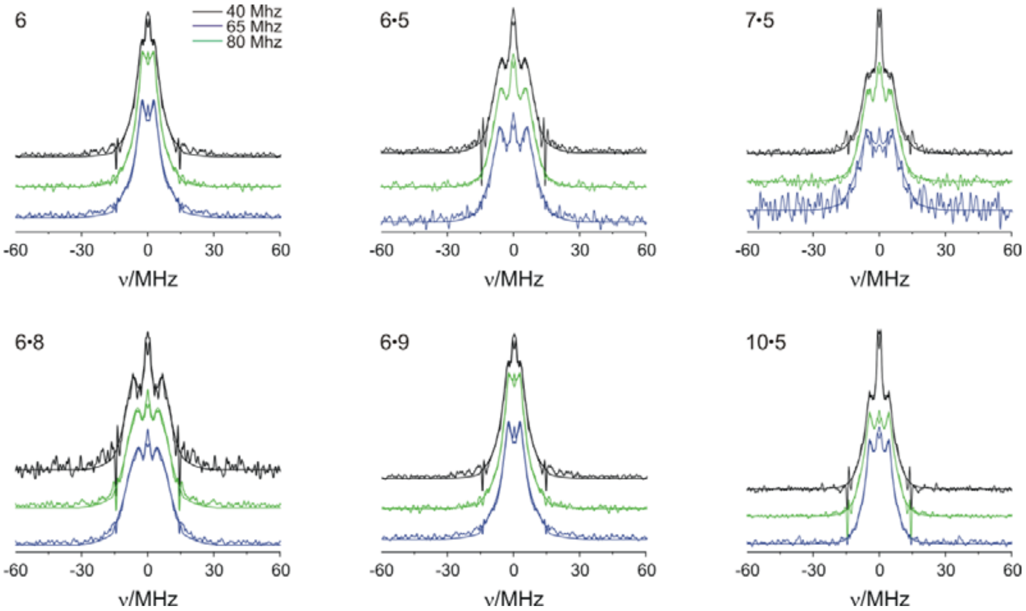

Figure 7.4 Fourier transformations of the background corrected dipolar evolution data of low temperature (T = 50 *K*) orientation selective pulse EPR spectra at X-band (~ 9.4 *GHz*) measured in 0.1 *M* NaCl, 10 *mM* $MgCl_2$ and 10 % glycerol (pH 7.0) for the frequency offsets 40, 65 and 80 *MHz* (black, green and blue lines, respectively).

Hybridization or introduction of mismatches significantly changes the interspin distance distributions (Fig. 7.3, Table 7.1). The double labeled, single stranded oligonucleotide **6** exhibits a distance distribution with a mean distance of 2.09 *nm* and a width of 1.1 *nm*, whereas the matched double stranded DNA duplex **6·5** reveals significantly smaller distance and distance distribution width values of 1.80 *nm* and 0.56 *nm*, respectively. Compared to the single stranded DNA, hybridization leads to a more structured conformation. Incorporation of the thymine mismatch in the complementary strand at position 8 decreases the interspin distance (**7·5,** 1.73 *nm*). An almost identical distance distribution is observed for DNA duplex **6·9** carrying a dA·dA mispair. For the DNA duplex **6·8** with the dT·dT mispair at position 9, the mean interspin distance is enlarged (1.86 nm). However, the largest interspin distance (2.08 *nm*) is found for DNA duplex

10·5 with the dA·dA mispair at position 9. This is in agreement with the thermodynamic analysis discussed before. A more pronounced decrease of the T_m values was found for both dA·dA mispairs reflecting the dependence of the effects on the type of mismatch. For all modified double labeled, double stranded DNA duplexes, the distribution widths of 0.5-0.6 *nm* resemble the results for the unmodified double labeled DNA duplex **6·5**. Sicoli *et al.*[9] performed similar pulse EPR experiments on duplex DNA with spin labels located in the minor groove and separated by six nucleotides. They detected lesion-induced global conformational changes. In the present study, the two spin labels of the 12-mer duplex are located in the major groove of the DNA duplex and separated by two nucleotides. Hence, the interspin distances were expected to react more sensitively to changes in the direct environment of the spin labels due to mismatch formation. Shortening as well as lengthening of the interspin distances, depending on the particular type of the mismatch and its nearest neighbors, as observed in the present study, may be evidence that the whole DNA shrinks or expands when a mismatch is incorporated. Another plausible explanation would be a local change of the base pair overlaps caused by mismatches. This can induce changes in the base pair twist perpendicular to the helix axis which ultimately leads to shortening or lengthening of the distance between the spin labels. Other local structural perturbations are possible such as more or less bending of the segments between the spin labels. Nevertheless, we anticipate that the overall shape is not significantly affected. A previous NMR study on DNA duplexes containing dA·dA or dT·dT mismatches revealed no significant global conformational changes upon introduction of the mismatches[34]. Both duplex structures with incorporated mispairs resembled the B-form of the fully matched DNA duplex structure.

7.5 Conclusion

This work reports on distance changes occurring in site-directed spin labeled duplex DNA when mismatches replace canonical base pairs. Based on ethynylated DNA, 4-azido TEMPO spin labels were introduced at the 7-position of the 7-deazadenine moiety by the copper assisted azide-alkyne ‘click’ reaction. *Cw* EPR experiments reveal that the overall mobility of the spin label side chains does not depend on the chain position of incorporation or the type of the mismatches incorporated. However, the distances between spin labels change when canonical dA·dT base pairs are replaced by dA·dA or dT·dT mispairs. The interspin distances do not only depend on the type of mismatch, but also on nearest neighbors located at the 3′- or 5′-site next to the spin label. The results disclose local changes induced by the mismatches under participation of nearest neighbors. These changes are finally transferred to the base pairs carrying the spin labels. This cross talk cannot be observed when the mismatches are far away from the bases bearing the spin label[9]. Thus, we have shown that the interspin distance is not only sensitive to a particular type of mismatch but also to the nearest neighbor environment. Implications of these distance changes are obvious for DNA repair, as repair enzymes do not simply recognize single mismatches but distinguish between mismatches in the context of a sequence motif[35,36].

7.6 References

[1] Kong, Q. M.; Lin, C. L. G. *Cell. Mol. Life Sci.* 2010, *67*, 1817-1829.

[2] Cederbaum, A. I.; Lu, Y. K.; Wu, D. F. *Arch. Toxicol.* 2009, *83*, 519-548.

[3] Cadet, J.; Douki, T.; Gasparutto, D.; Ravanat, J. L. *Mutat. Res.* 2003, *531*, 5-23.

[4] Friedberg, E. C. *Nature.* 2003, *421*, 436-440.

[5] Cadet, J.; Bellon, S.; Douki, T.; Frelon, S.; Gasparutto, D.; Muller, E.; Pouget, J. P.; Ravanat, J. L.; Romieu, A.; Sauvaigo, S. *J. Environ. Pathol. Toxicol.Oncol.* 2004, *23*, 33-43.

[6] Schärer, O. D. *Angew. Chem. Int. Ed.* 2003, *42*, 2946-2974.

[7] Bjelland, S.; Seeberg, E. *Mutat. Res.* 2003, *531*, 37-80.

[8] Cekan, P.; Sigurdsson, S. T. *J. Am. Chem. Soc.* 2009, *131*, 18054-18056.

[9] Sicoli, G.; Mathis, G.; Aci-Seche, S.; Saint-Pierre, C.; Boulard, Y.; Gasparutto, D.; Gambarelli, S. *Nucleic Acids Res.* 2009, *37*, 3165-3176.

[10] Schiemann, O.; Prisner, T. F. *Q. Rev. Biophys.* 2007, *40*, 1-53.

[11] Lukin, M.; de los Santos, C. *Chem. Rev.* 2006, *106*, 607-686.

[12] Wozniak, A. K.; Schröder, G. F.; Grubmüller, H.; Seidel, C. A. M.; Oesterhelt, F. *Proc. Natl. Acad. Sci.* 2008, *105*, 18337-18342.

[13] Lu, L.; Yi, C.; Jian, X.; Zheng, G.; He, C. *Nucleic Acids Res.* 2010, *38*, 4415-4425.

[14] Schneider, S.; Schorr, S.; Carell, T. *Curr. Opin. Struct. Biol.* 2009, *19*, 87-95.

[15] Sicoli, G.; Mathis, G.; Delalande, O.; Boulard, Y.; Gasparutto, D.; Gambarelli, S. *Angew. Chem. Int. Ed.* 2008, *47*, 735-737.

[16] Schiemann, O.; Piton, N.; Mu, Y.; Stock, G.; Engels, J. W.; Prisner, T. F. *J. Am. Chem. Soc.* 2004, *126*, 5722-5729.

[17] Qin, P. Z.; Dieckmann, T. *Curr. Opin. Struc. Biol.* 2004, *14*, 350-359.

[18] Wunnicke, D.; Strohbach, D.; Weigand, J. E.; Appel, B.; Feresin, E.; Suess, B.; Müller, S.; Steinhoff, H. J. *RNA*. 2011, *17*, 182-188.

[19] Jakobsen, U.; Shelke, S. A.; Vogel, S.; Sigurdsson, S. T. *J. Am. Chem. Soc.* 2010, *132*, 10424-10428.

[20] Ding, P.; Wunnicke, D.; Steinhoff, H. J.; Seela, F. *Chem. Eur. J.* 2010, *16*, 14385-14396.

[21] Schiemann, O.; Cekan, P.; Margraf, D.; Prisner, T. F.; Sigurdsson, S. T. *Angew. Chem. Int. Ed.* 2009, *48*, 3292-3295.

[22] Polyhach, Y.; Godt, A.; Bauer, C.; Jeschke, G. *J. Magn. Reson.* 2007, *185*, 118-129.

[23] Savitsky, A.; Dubinskii, A. A.; Flores, M.; Lubitz, W.; Möbius, K. *J. Phys. Chem. B.* 2007, *111*, 6245-6262.

[24] Barhate, N.; Cekan, P.; Massey, A. P.; Sigurdsson, S. T. *Angew. Chem. Int. Ed.* 2007, *46*, 2655-2658.

[25] Seela, F.; Zulauf, M. *Chem. Eur. J.* 1998, *4*, 1781-1790.

[26] Freed,J.H. Theory of Slow Tumbling ESR Spectra for Nitroxides. In *Spin Labeling: Theory and Applications.* , Berliner,L.J. (ed.) Academic Press: New York, 1976, pp. 53-132.

[27] Pannier, M.; Veit, S.; Godt, A.; Jeschke, G.; Spiess, H. W. *J. Magn. Res.* 2000, *142*, 331-340.

[28] SantaLucia, J. Jr.; Hicks, D. *Annu. Rev. Biophys. Biomol. Struct.* 2004, *33*, 415-440.

[29] Peyret, N.; Seneviratne, P. A.; Allawi, H. T.; SantaLucia, J., Jr. *Biochemistry* 1999, *38*, 3468-3477.

[30] Seela, F.; Debelak, H. *Nucleic Acids Res*. 2000, *28*, 3224-3232.

[31] Aboulela, F.; Koh, D.; Tinoco, I.; Martin, F. H. *Nucleic Acids Res.* 1985, *13*, 4811-4824.

[32] Werntges, H.; Steger, G.; Riesner, D.; Fritz, H. J. *Nucleic Acids Res*. 1986, *14*, 3773-3790.

[33] Jeschke, G.; Chechik, V.; Ionita, P.; Godt, A.; Zimmermann, H.; Banham, J. E.; Timmel, C. R.; Hilger, D.; Jung, H. *Appl. Magn. Reson.* 2006, *30*, 473-498.

[34] Gervais, V.; Cognet, J. A.; Le, B. M.; Sowers, L. C.; Fazakerley, G. V. *Eur. J. Biochem.* 1995, *228*, 279-290.

[35] Mazurek, A.; Johnson, C. N.; Germann, M. W.; Fishel, R. *Proc. Natl. Acad. Sci.* 2009, *106*, 4177-4182.

[36] Iyer, R. R.; Pluciennik, A.; Burdett, V.; Modrich, P. L. *Chem. Rev.* 2006, 106, 302-323.

8

Summary and Outlook

Nucleic acids like deoxyribonucleic acids (DNA) and ribonucleic acids (RNA) are essential constituents of all living organisms. The fundamental functions of DNA and RNA are the long-term storage of genetic instructions and the implementation of the genetic information into amino acid sequences of proteins, respectively. Furthermore, RNA accomplishes different functions such as transfer RNA (tRNA), ribosomal RNA (rRNA) or gene regulator (riboswitches). For functional RNA and DNA not only the primary sequences of the nucleotides but also the three dimensional conformations are important. For a deeper understanding of the role of structural rearrangements conformational changes induced by ligand binding to the aptamer (first section) and by DNA mismatches (second section) were studied in this thesis.

Natural occurring riboswitches, a class of RNA molecules, are able to control the implementation of genetic information through the regulation of gene expression, either through premature termination of transcription or inhibition of translation initiation. Both, natural and synthetic riboswitches, so-called aptamers, are complex folded three dimensional structures, which bind specific ligands such as cofactors, amino acids or nucleobases in preformed binding pockets. They are mainly located in the 5' untranslated region (UTR) of prokaryotic mRNAs. Ligand binding often induces structural rearrangements of the RNA structures, which in turn regulate gene expression and therefore the implementation of genetic instructions. The functional mechanism of these regulatory elements in detail is unknown. Further information about the dynamics and the structure of the riboswitches are necessary for a detailed understanding of the functional mechanism.

In the first section of this work *cw* and pulse EPR spectroscopy in combination with site-directed spin labeling was performed to investigate the dynamics and conformational alterations of the synthetic Tc riboswitch. The Tc aptamer functions as a molecular switch for conditional gene expression in yeast. It binds its ligand with a dissociation constant of ~0.8 *nM* in a 1:1 stoichiometry. The ligand Tc is able to inhibit prokaryotic translation and is often utilized as a therapeutic agent of low toxicity. In first instance the methanethiosulfonate spin labels were post-synthetically introduced by reaction with 4-thiouridine-modified RNA. The results of the *cw* EPR study on single and double labeled RNA mutants revealed ion-induced changes of the overall spin label mobility and the polarity of the micro-environment due to conformational changes. The data provided first evidence that the conformation of the aptamer in a Mg^{2+}-containing buffer in the presence of Tc resembles the one in the absence of the ligand. However, small, local structural changes upon Tc-binding could not be excluded. For further studies a TEMPO spin label was attached by reaction with 2'-aminouridine-modified RNA. Pulse EPR experiments were performed on double labeled RNA mutants to distinguish between ion and ligand induced effects and to determine interspin distances within a 2-6 *nm* range. The results obtained herein indicate a thermodynamic equilibrium of two aptamer conformations in the absence of Tc, where one of these conformations is captured upon ligand binding.

In addition, three aptamer structures have been modeled based on the published crystal structure of a circularly permuted Tc riboswitch and on interspin distances measured by *cw* and pulse EPR spectroscopy in this study. Two models correspond to the two equilibrium conformations in the absence of the ligand, the third model to the captured aptamer conformation in the presence of Tc. MD simulations for all RNA models were carried out in order to verify the models and to compare experimentally obtained interspin distances with simulated ones. The results show a good agreement between both. In conclusion, these studies have uncovered the existence of such a conformational equilibrium in the free state. The shift to one of these conformations upon ligand binding seems to be an appropriate functional mechanism for a riboswitch to manipulate gene expression.

In the future the binding and folding kinetics of the Tc aptamer could be followed by stopped flow or freeze quench approaches in combination with EPR spectroscopy to provide an in-depth knowledge about the functional mechanism for riboswitches. The use of Tc derivatives and the investigation of the ligand binding and its consequences for the conformational equilibrium may rate the importance of conformational alterations for the specificity of the riboswitches towards its ligand.

The incorporation of DNA mutations such as nucleobase changes, double-strand breaks and mispairings can lead to structural and conformational changes of DNA domains which in turn are related to inheritable diseases, cancer and aging. For a more comprehensive understanding of the structure-function relationship a detailed background about mismatch-induced conformational changes is required.

In the second section of this work, spin labeled DNA systems were investigated by *cw* and pulse EPR spectroscopy. Within this project, the copper(I)-catalyzed Huisgen-Sharpless-Meldal alkyne-azide cycloaddition (CuAAC) ‘click reaction’ was introduced as a powerful modification of existing strategies for further DNA and RNA studies. Therefore, two TEMPO spin labels were incorporated with high efficiency in a DNA duplex at spatially separated positions within one strand or in a dA·dT base pair. Interspin distances within the 1-2 *nm* range and exceptionally narrow distribution widths were determined by *cw* and pulse EPR experiments. MD simulations were performed for both spin labeled DNA duplexes with the spin labels adjusted to their experimental determined interspin distance. The results exhibit a very good agreement between simulated and experimentally obtained distances. Furthermore, no perturbation of the DNA structure were observed when the two spin labels were incorporated at separated positions and only minor perturbation due to the incorporation of the two spin labels into the dA·dT base pair.

Besides spin labeling of dA·dT base pairs, the new spin labeling technique has the potential to be extended to dG and dC derivatives and therefore allows spin labeling of all four DNA as wells as RNA constituents for further EPR studies. In summary this spin labeling method is demonstrated to be a powerful tool to spin label unknown DNA structures as well as synthetic parallel and anti-parallel DNA in future experiments. In the present study the new spin labeling protocol was used to identify mismatch-induced conformational changes of spin labeled DNA. For this purpose a DNA system was chosen with two spin labels separated by two nucleotides. The application of *cw* and orientation selective pulse EPR measurements provided insights into the dynamics and structural alterations caused by mismatched base pairs. Mismatches such as dA·dA or dT·dT mispairs left the overall mobility of the spin label side chains unaltered, independent of the chain position or the type of the incorporated mismatches. In contrast, interspin distances have been found to depend on the type and nearest neighbor environment of the mismatch. The changes are transferred to the base pairs carrying the spin labels. Consequently, these findings may enhance the comprehension for DNA repair, as repair enzymes may not only specifically recognize single mismatches but also distinguish between mismatches in the context of a sequence motif and/or folding properties.

Future investigations can be extended not only to e.g. dG·dG, dC·dC, dA·dC or dA·dG mispairs but also to a systematic study of different nearest neighbors of the spin label. Furthermore, the effects on interspin distance distributions and conformational alterations can be traced in dependence of the position of the spin label, including positions close the 3′- or 5′-end or in the center of the DNA duplex. This may additionally deepen the knowledge about the mechanisms of DNA repair enzymes and their structure-function relationship.

9

Appendix

Oligonucleotide	$[M\text{-}1]^-$ (Da)	
	Calc.	Found
5′-d(TAG GTC **1**AT ACT) (**12**)	3667	3666
5′-d(AGT AT**2** GAC CTA) (**13**)	3653	3653
5′-d(TAG GTC **1**AT **1**CT) (**14**)	3690	3690
5′-d(TAG GTC **4**AT ACT) (**15**)	3863	3863
5′-d(AGT AT**5** GAC CTA) (**16**)	3851	3850
5′-d(TAG GTC **4**AT **4**CT) (**17**)	4084	4084

[a] Determined as $[M\text{-}1]^-$ in the linear negative mode.

Table A1. Molecular masses $[M\text{-}1]^-$ of oligonucleotides measured by MALDI-TOF mass spectrometry.[a]

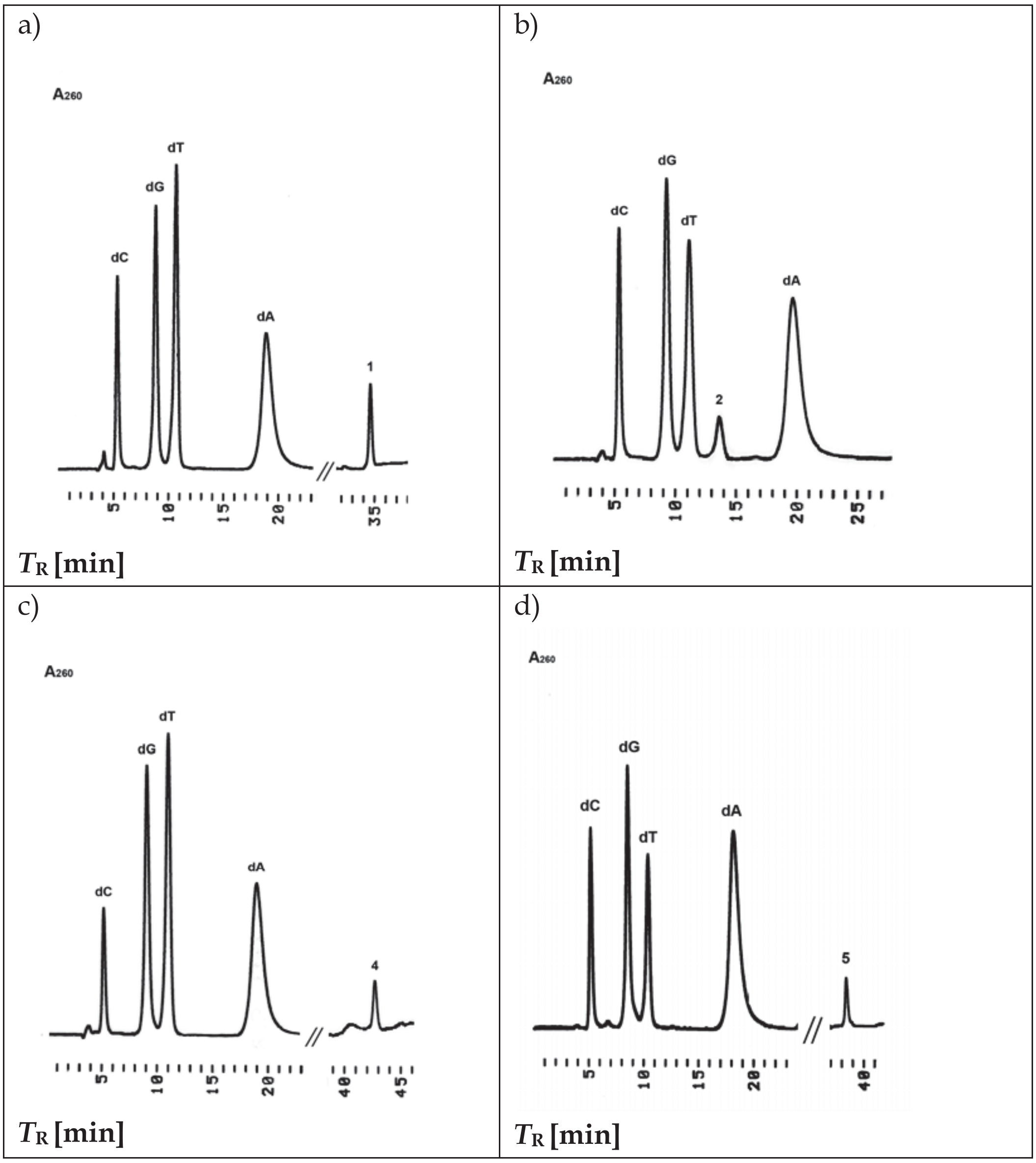

Figure A1. HPLC profiles of the enzymatic hydrolysis products a) of the oligonucleotide 5′-d(TAG GTC **1**AT ACT) (**12**); b) of oligonucleotide 5′-d(AGT AT**2** GAC CTA) (**13**); c) of the oligonucleotide 5′-d(TAG GTC **4**AT ACT) (**15**); d) of the oligonucleotide 5′-d(AGT AT**5** GAC CTA) (**16**) obtained after digestion with snake venom phosphodiesterase and alkaline phosphatase in 0.1 M Tris-HCl buffer (pH 8.3) at 37 °C. Gradient: 0-20 min 100% A, 20–40 min 0–30% B in A, 40-50 min 30% B in A, 50-60 min 30-0% B in A, flow rate 0.7 mL min^{-1} (A = 0.1 M (Et_3NH)OAc (pH 7.0)/MeCN 95:5, B = MeCN).

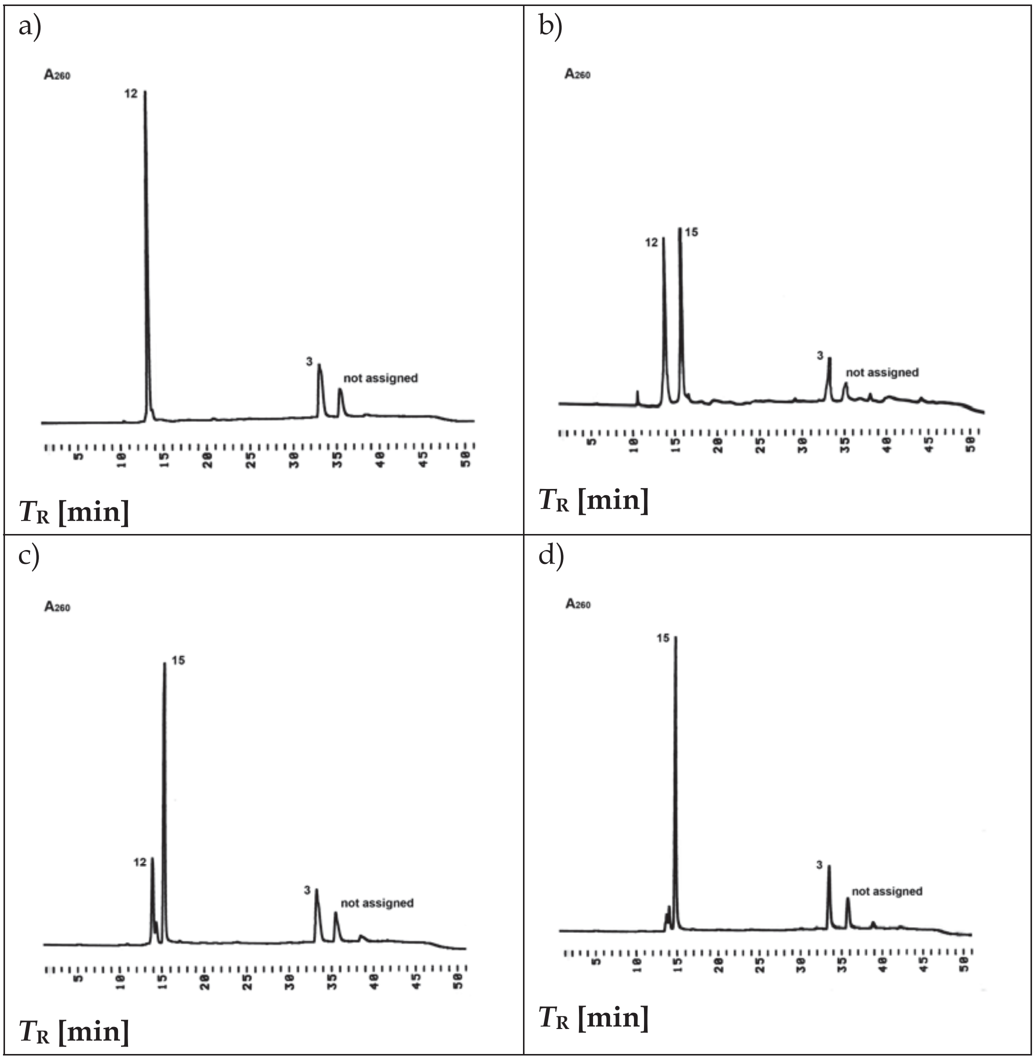

Figure A2. HPLC profiles of the Cu (I) catalyzed 'click' reaction of the oligonucleotide 5′-d(TAG GTC **1**AT ACT) (**12**) with 4-azido TEMPO **3**, monitored in intervals by HPLC, 20 µL reaction mixture per injection a) at 0 min; b) at 60 min; c) at 120 min; d) at 240 min. Gradient: 0-30 min 0–60% B in A, 30-40 min 60% B in A, 60-0 %B in A, flow rate 0.7 mL min^{-1} (A = 0.1 M (Et_3NH)OAc (pH 7.0)/MeCN 95:5, B = MeCN).

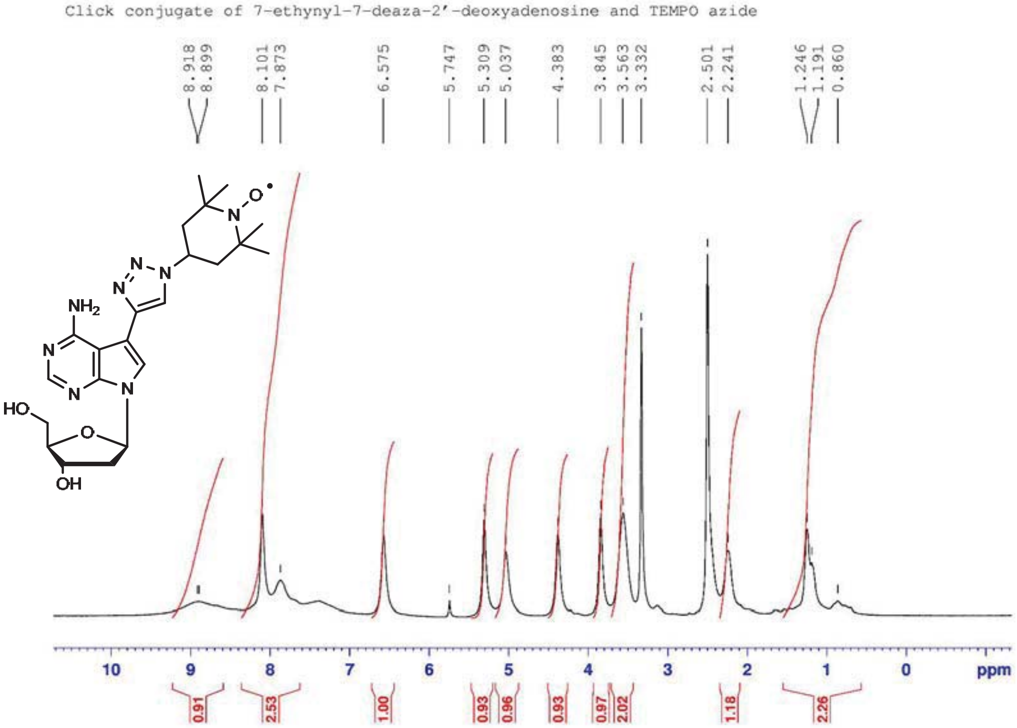

Figure A3. ¹H-NMR spectrum of compound **4.**

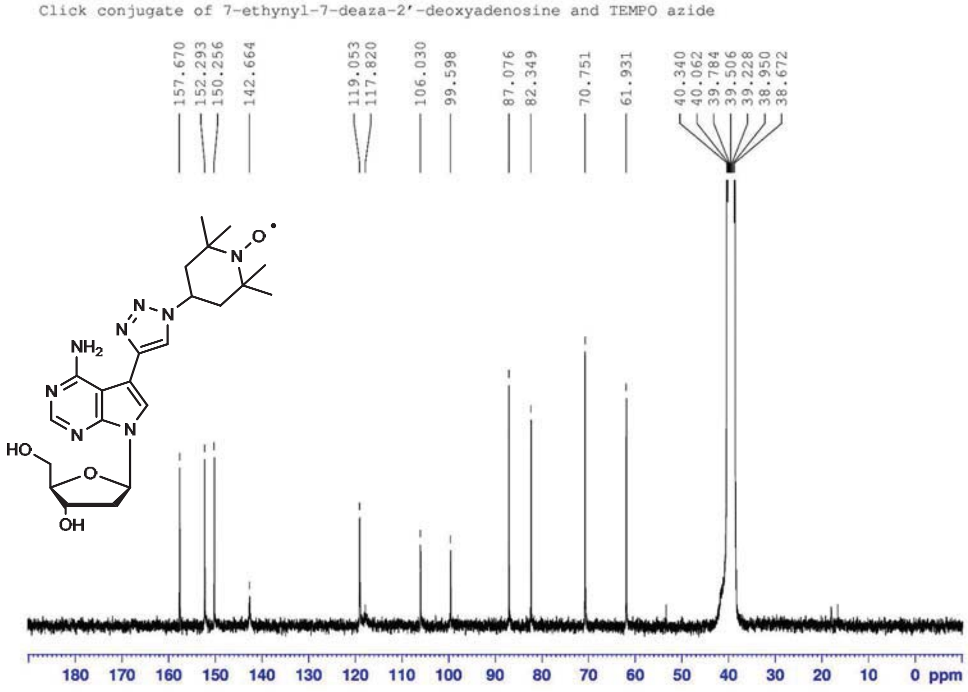

Figure A4. ¹³C-NMR spectrum of compound **4.**

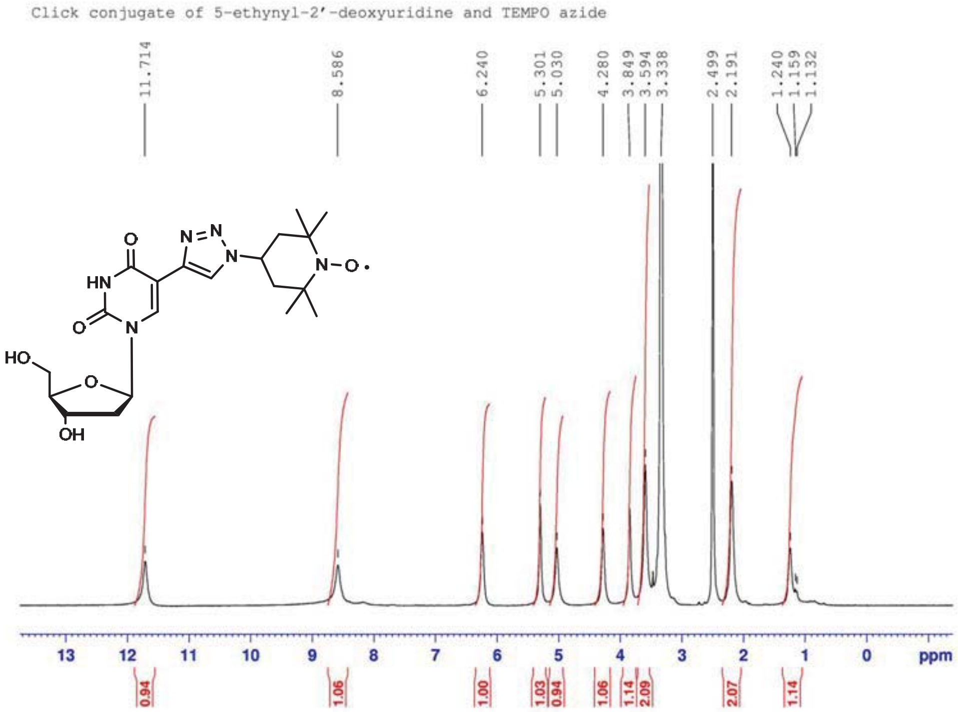

Figure A5. ^{1}H-NMR spectrum of compound **5.**

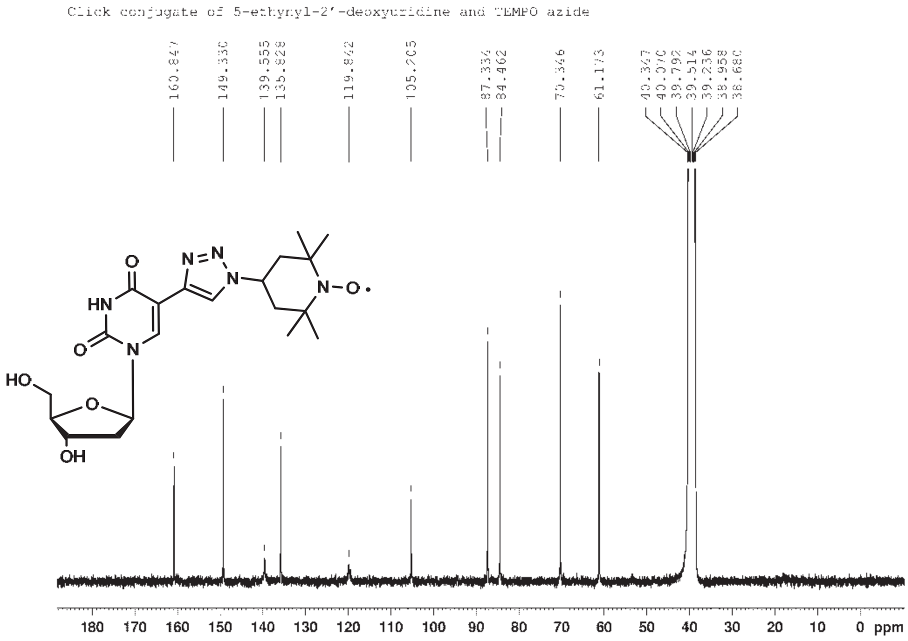

Figure A6. ^{13}C-NMR spectrum of compound **5.**

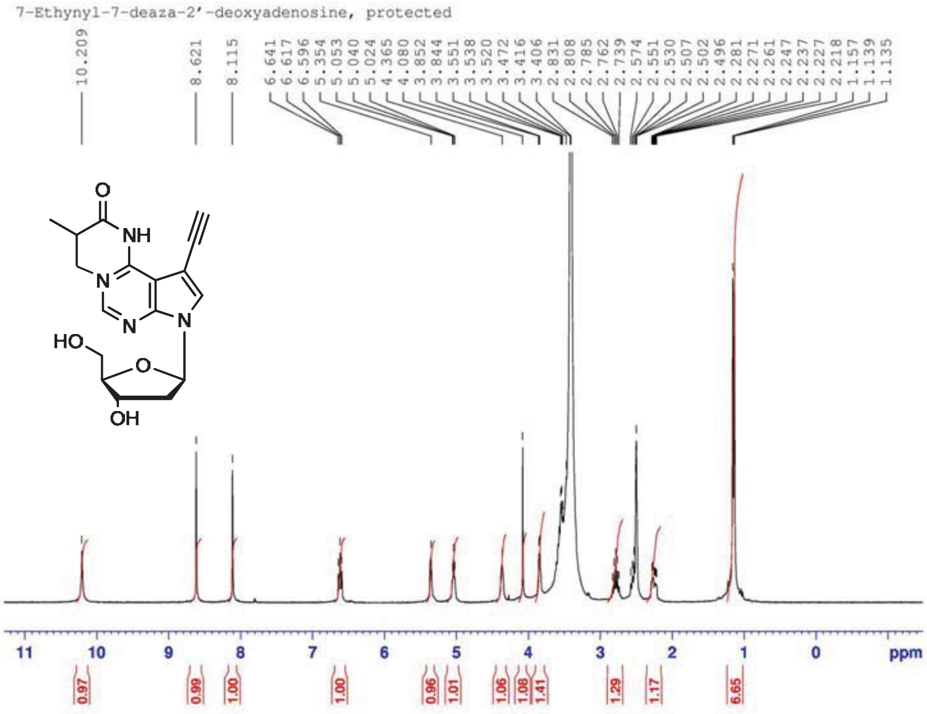

Figure A7. ^{1}H-NMR spectrum of compound **6.**

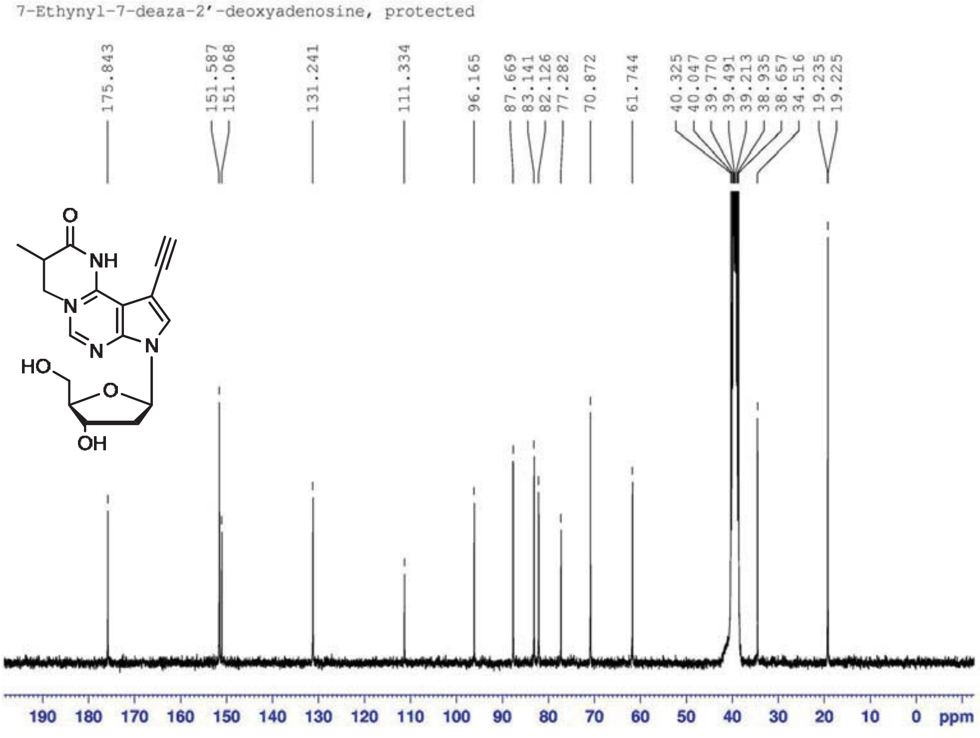

Figure A8. ^{13}C-NMR spectrum of compound **6.**

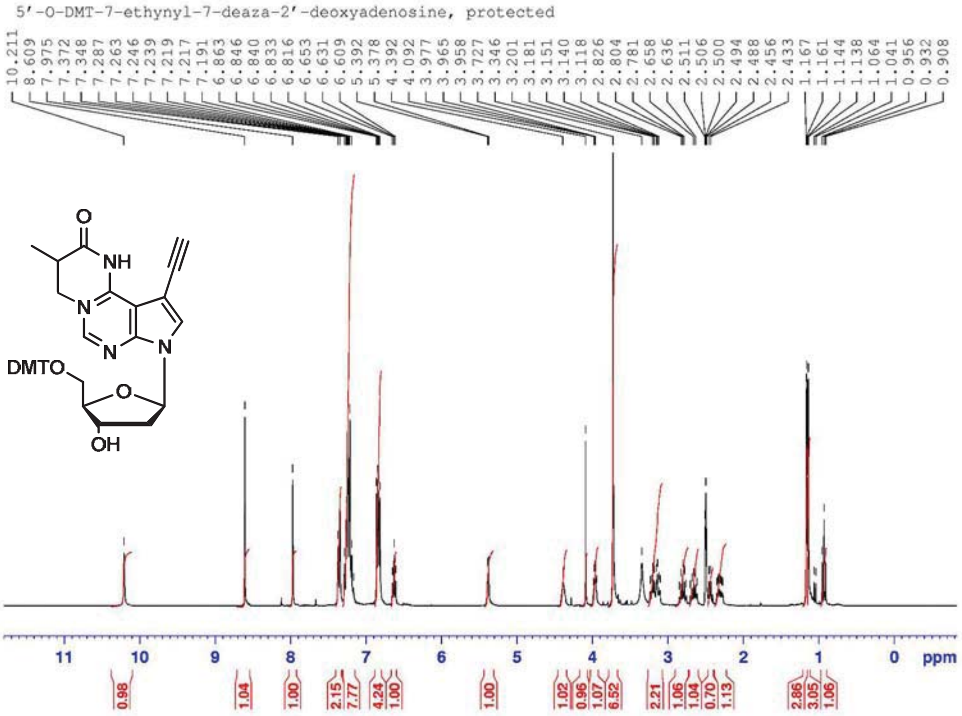

Figure A9. ^{1}H-NMR spectrum of compound **7.**

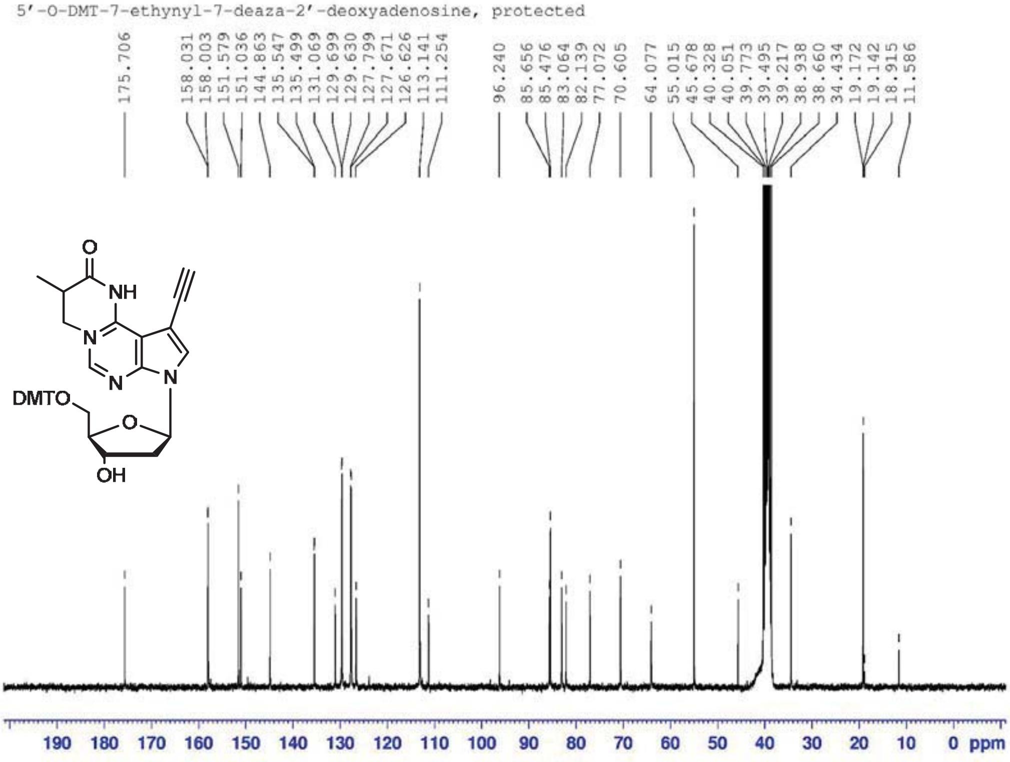

Figure A10. ^{13}C-NMR spectrum of compound **7.**

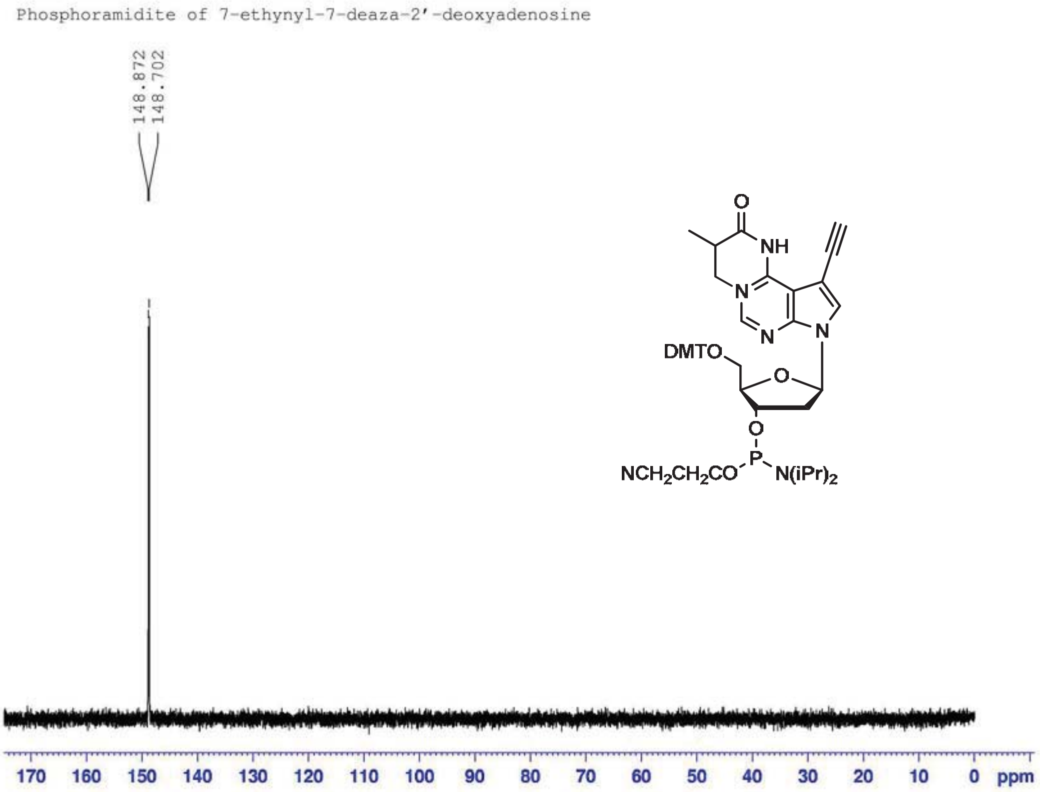

Figure A11. ^{31}P-NMR spectrum of compound **8.**

Oligonucleotide	[M-1]$^-$ (Da)	
	Calc.	Found
5′-d(TAG GTC **1**AT **1**CT)	3690	3690
5′-d(TAG GTC **3**AT **3**CT) (**6**)	4084	4084
5′-d(TAG GTC **1**TT **1**CT)	3681	3681
5′-d(TAG GTC **3**TT **3**CT) (**7**)	4075	4075

[a] Determined as [M-1]$^-$ in the linear negative mode.

Table B1. Molecular masses [M-1]$^-$ of oligonucleotides measured by MALDI-TOF mass spectrometry.[a]

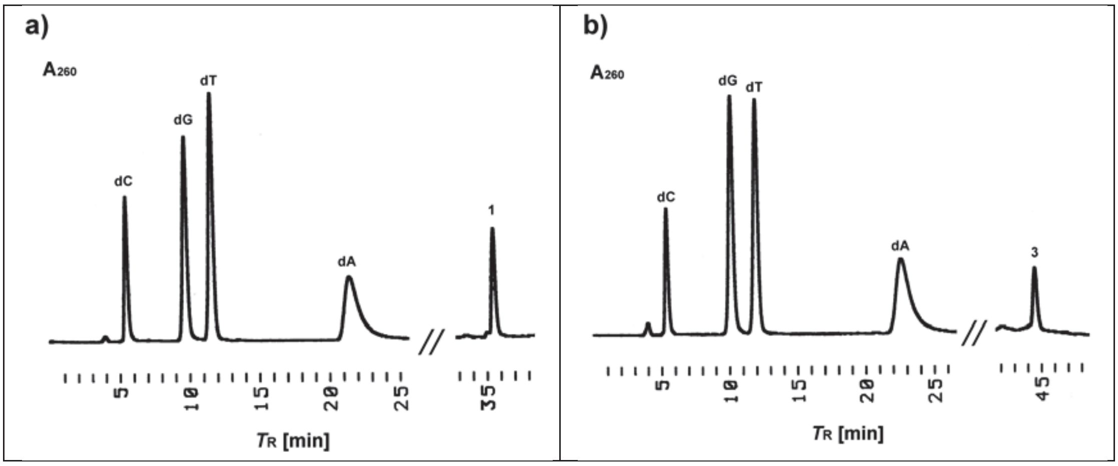

Figure B1. HPLC profiles of the enzymatic hydrolysis products a) of the oligonucleotide 5′-d(TAG GTC **1**AT **1**CT) and b) of oligonucleotide 5′-d(TAG GTC **3**AT **3**CT) (**6**) obtained after digestion with snake venom phosphodiesterase and alkaline phosphatase in 0.1 M Tris-HCl buffer (pH 8.3) at 37 °C. Gradient: 0-20 min 100% A, 20–40 min 0–30% B in A, 40-50 min 30% B in A, 50-60 min 30-0% B in A, flow rate 0.7 mL min^{-1} (A = 0.1 M (Et_3NH)OAc (pH 7.0)/MeCN 95:5, B = MeCN).

Eidesstattliche Erklärung

Ich erkläre hiermit, dass ich die vorliegende Arbeit ohne unzulässige Hilfe Dritter und ohne Benutzung anderer als der angegebenen Hilfsmittel angefertigt habe. Die aus anderen Quellen direkt oder indirekt übernommenen Daten und Konzepte sind unter Angabe der Quelle gekennzeichnet.

Bei der Auswahl und Auswertung folgenden Materials haben mir die nachstehend aufgeführten Personen in der jeweils beschriebenen Weise unentgeltlich geholfen.

1. Die Synthese der RNA Proben erfolgte zunächst von Denise Strohbach (Universität Bochum) und anschließend durch Bettina Appel (Universität Greifswald) aus der Arbeitsgruppe von Frau Prof. S. Müller.

2. Die in dieser Arbeit gezeigten Bindungskonstanten der RNA Proben wurden durch Julia Weigand (Universität Frankfurt) aus der Arbeitsgruppe von Frau Prof. B. Suess bestimmt.

3. Die Synthese der DNA Proben, die Bestimmung der T_m Werte und der gezeigten NMR und Massenspektren erfolgten durch Ping Ding (Universität Münster) aus der Arbeitsgruppe von Herrn Prof. F. Seela.

Weitere Personen waren an der inhaltlichen materiellen Erstellung der vorliegenden Arbeit nicht beteiligt. Insbesondere habe ich hierfür nicht die entgeltliche Hilfe von Vermittlungs- bzw. Beratungsdiensten (Promotionsberater oder andere Personen) in Anspruch genommen. Niemand hat von mir unmittelbar geldwerte Leistungen für Arbeiten erhalten, die im Zusammenhang mit dem Inhalt der vorgelegten Dissertation stehen.

Die Arbeit wurde bisher weder im In- noch im Ausland in gleicher oder ähnlicher Form einer anderen Prüfungsbehörde vorgelegt.

Osnabrück, der 21.07.2011

Danksagung

An erster Stelle möchte ich mich sehr herzlich bei Herrn Prof. H.-J. STEINHOFF bedanken für die faszinierende Aufgabenstellung und die großartige Betreuung während meiner gesamten Doktorandenzeit, insbesondere für seine stets „offene Tür".

Mein besonderer Dank gilt zudem Frau Prof. B. SÜSS für die Bereitschaft das Zweitgutachten über diese Arbeit zu erstellen. Zudem wäre diese Arbeit ohne das RNA Projekt nicht möglich gewesen.

Ohne Proben hätte diese Arbeit ebenfalls gar nicht erst entstehen können, daher möchte ich mich hiermit bei allen bedanken, die an den RNA und DNA Projekten beteiligt waren: JULIA WEIGAND unter Leitung von Frau Prof. B. SÜSS, DENISE STROHBACH und BETTINA APPEL aus der Arbeitsgruppe von Frau Prof. S. MÜLLER und PING DING unter Leitung von Herrn Prof. F. SEELA. BETTINA möchte ich besonders für die herzliche Aufnahme und die Betreuung während meines Aufenthaltes in Greifswald danken.

Bedanken möchte ich mich auch bei meinen Kollegen: ALEXEY LOKHMATIKOV, ARMEN MULKIDJIANIAN, CHRISTIAN BEIER, CHRISTIAN RICKERT, CONSTANZE SCHWAN, DANIEL KLOSE, DARIA DIBROVA, ENRICA BORDIGNON, HENRIK BRUTLACH, IOAN ORBAN, JULIA HOLTERHUES (für die herzliche Aufnahme in die Arbeitsgruppe und unsere gemeinsamen Mädels-Kochabende), KATRIN JAHNS, LAKSHMI PULAGAM, LESZEK URBAN, MARCO CICHON, MARION VON LANDSBERG (ohne die unsere AG nicht mehr dieselbe sein wird), MEIKE MÜLLER-TRIMBUSCH, MICHAEL SIPPACH, NATASCHA VOSKOBOYNIKOVA, PHILIPP GRÖNE, PRASAD GAJULA, SABRINA DUNKEL, VITALI ZIELKE, WERNER GEISLER, WAGEIHA MOSSLEHY für eine vielleicht nicht immer einfache, aber auch nie langweilige Zeit in unserer Arbeitsgruppe. Dabei werden mir besonders unsere „Doktorandenabende" im Gedächtnis bleiben.

Darüberhinaus möchte ich mich bei JOHANN P. KLARE und INGA HAENELT für das Korrekturlesen dieser Arbeit bedanken. Ebenfalls danken möchte ich INGA für die hilfreichen und immer wieder interessanten Diskussionen rund um meine Arbeit und vieles mehr. Meinen Bürokollegen möchte ich nicht nur für unsere Diskussionen danken, sondern auch für „faszinierende" Einblicke in die männliche Denkweise - meistens. Ganz besonderen Dank möchte ich an dieser Stelle SABINE BÖHME und CHRISTOPH ABÉ sagen für die vielen kleinen und großen lustigen

Momente (von denen es reichlich gab) und die Gespräche auch in den nicht so guten Zeiten. Das Nachhausegehen ist langweilig geworden …

Bei meinen Freunden, Brüdern und meinen Eltern möchte ich mich besonders herzlich Bedanken für Ihre ununterbrochene Hilfe und Unterstützung auch und insbesondere außerhalb der Universität in all den Jahren.

Danke!